ON HOMOGENIZATION AND DE-HOMOGENIZATION OF COMPOSITE MATERIALS

A Thesis

Submitted to the Faculty

of

Drexel University

by

Chang (Karen) Yan

in partial fulfillment of the

requirements for the degree

of

Doctor of Philosophy

November 2003

To my family

ACKNOWLEDGEMENTS

I would like to express my sincere and deep gratitude to my advisor Dr. Albert S.D. Wang, for his help, guidance and encouragement throughout my graduate studies. I would also like to express my thanks to the members of my thesis committee: Dr. Alan Lau, Dr. Horacio Sosa, Dr. David Wotton, and Dr. Aspasia Zerva for their help and valuable comments.

I would like to thank Dr. Wei Sun for his help and support since the first day I came to Drexel.

I would also like to thank the faculty and staff of the MEM Department, for keeping things moving smoothly.

Special thanks to Dr. Simon Chung, my lab partner, for many discussions on the composite research, and helps during my stay at Drexel.

Thanks to my friends at Drexel and elsewhere, you know who you are, for making my life more enjoyable.

Finally, special thanks to my husband, Dr. Peng Song, and our families half a world away. Without their unwavering support, love, and understanding, I would have never been able to complete this journey.

Table of Contents

List of Tables

List of Figures

Abstract

On Homogenization and De-homogenization of Composite Materials

Chang (Karen) Yan

Albert S.D. Wang, Ph.D.

Composite homogenization is a modelling concept that allows the description of heterogeneous materials by constitutively equivalent, homogeneous ones. The concept is universally applied to fibrous composites, resulting in many modelling approaches. But, by homogenization, the composite is voided of its physical microstructure; elements that may affect failure mechanisms physically are also voided. This fact often leads to difficulties in failure theories formulated at the homogenized material scale.

De-homogenization is a reverse scheme in that the microstructure is restored, albeit locally, back in the homogenized composite. Clearly, this is done after composite homogenization and field analysis of composite structures under global loading; so the micro fields in the desired locations with restored microstructure can be recovered. The recovered micro fields may then provide the needed information for some failure theories to be formulated at the composite micro scale instead.

This thesis presents a unified modelling approach for homogenization (forward) and de-homogenization (backward), applicable to unidirectional composite systems. Emphasis is placed on the uniqueness between the forward and the backward modelling processes; so the desired micro fields are truly recovered within the confines of mechanics.

Micro fields in several laminates made of the UD systems are recovered; key effects that influence failure mechanisms therein are studied. An inter-scale failure theory that describes matrix cracking in laminates is then formulated, being based on the recovered

micro-fields.

Laminate matrix cracking in several well-documented experimental studies are simulated using the inter-scale theory. The simulation captures the major cracking characteristics that are otherwise excluded in failure theories derived at the homogenized composite scale.

The general concept of homogenization/de-homogenization is applicable to all composite systems, where responses from micro-macro-global interactions are to be physically described. The approach taken in the formulation of the inter-scale theory serves as an example of both conceptual and practical importance.

Chapter 1: Introduction

1.1 Background

Advanced fiber-reinforced composite materials have been widely used in various load-bearing structures, from sporting goods to aerospace vehicles. The ever-increasing popularity of fiber-reinforced composites is due largely to their lightweight, high strength, and superior structural durability. Besides, these and many other functional properties can be tailored through a proper composition of two essential constituents: the fiber and the matrix. However, the spatial layout of the fibers in matrix-consolidated composites often forms a complex fibrous network, an integral part of the composite microstructure at the fiber-matrix scale. Of course, this microstructure plays a dominant role in forming all the composite properties, including failure mechanisms.

In principle, property characterization of fibrous composites should be based on their precise microstructures. In practice, however, the true microstructures of the composites are often simplified in the characterization models, both geometrically and materially. The degree of simplification depends on the desired engineering accuracy. In this connection, the theory of homogenization [13, 14, 21, 42] is almost universally applied to characterizing fibrous composite properties.

Composite homogenization is a mechanics based modelling scheme that transforms a body of a heterogeneous material into a constitutively equivalent body of a homogeneous continuum. In principle, the transformation model should be built on the basis of

the composite microstructure, along with the relevant physical laws. A set of effective properties is obtained for the equivalent homogeneous continuum.

To fibrous composites, homogenization is an essential first step towards the design and analysis of larger scale and load-bearing structures. The analysis of a class of multi-directional laminates made of unidirectional fiber-reinforced laminas is a classical example. In this case, the unidirectional laminas are first homogenized, each with a set of effective properties. The laminate is then treated as a layered plate structure, capable of carrying globally applied thermo-mechanical loads. In this regard, several composite lamination theories [2, 46] and the ply-elasticity theories [39, 49] have been used to obtain the stress/strain fields in the homogenized laminas. Since the laminates are homogenized without micro structures, these stress/strain fields are termed as the macro stress/strain fields.

When a certain laminate is loaded, failures often occur inside one or more laminas and/or in the interface between two adjacent laminas. Traditionally, the computed macro stress/strain fields in the laminas are used in forming failure theories for the observed failures. Among the well known theories, the maximum stress [27], maximum strain [27], and stress-polynomial criteria [24, 47] are widely applied. These failure theories are based on the point stress state in the homogenized laminas, along with the assumptions that a point strength limit(s) exists in the same laminas; i.e. failure occurs when the lamina point stress state exceeds the strength limit(s) at that point.

Other failure criteria have been based on the concept of crack propagation [29, 33, 48]. In this case, finite crack-like flaws are artificially introduced to the homogenized lamina, which can propagate when the stress state near the flaw is critical. Here, the introduced

flaws are considered an effective property of the homogenized lamina.

Experimental correlations, however, could not validate the unique existence of either the strength limit(s) or the finite flaw(s) as effective lamina properties. In fact, documented experiments [28, 45] revealed that the strength limit(s) of the homogenized lamina can vary with a number of extrinsic factors, such as the geometry of the tested specimen and the test methods. Similarly, experimentally correlated effective flaw(s) in the homogenized lamina can also vary with the same extrinsic factors [6].

The general view has been that material failures in laminates actually initiate at the fiber-matrix (micro) scale, though the phenomenon is observed at the lamina (macro) scale. The transition from the micro scale failure to the macro scale failure can be either insidious or sudden depending on the material conditions existing in the microstructure. In short, both the material and geometrical effects at the micro scale play a role in this transition. Yet, many micro scale effects are self-equilibrating; and homogenization involves volume averaging which eliminates all self-equilibrating effects. This is perhaps the fundamental reason why the macro field based failure theories are unable to model sublaminate failures consistently.

In recent years, there have been concerted efforts in developing a viable technique to recover the micro fields in laminas of loaded laminates [26, 40, 53]. It is believed that the micro fields may provide the needed information as to how a certain failure occurs and to what extent the microstructure influences these events. A physical failure theory could then be developed, based on the micro fields in the loaded laminates.

Though the actual micro fields in a certain loaded laminate can be obtained by a

brute-force micromechanics analysis of the entire laminate, it is impractical if not impossible to do so in general practice. The only alternative is to follow the traditional approach to homogenize the laminas first and compute the macro fields of the homogenized laminas in laminates under global loads. Then, the actual micro fields in the laminas where failure(s) is the suspect are recovered through a reversed process termed as "de-homogenization". This process refers to the restoration of the composite microstructure back in the lamina where failure is suspected; the micro fields are recovered through a rigorous micromechanics analysis. In this regard, it is important to ensure the uniqueness and precision between the homogenization and de-homogenization processes. Only then, a physical theory could be developed for a certain failure that occurs in laminates.

1.2 Objectives and Scope

The objective of this thesis is two-fold:

(1) To develop a mechanics modelling methodology that can be applied to (a) homogenization of unidirectional lamina, with fewer simplifications and with precise mechanical analysis, and (b) de-homogenization of the homogenized lamina in laminates that are under external loads. Emphasis is placed on the uniqueness between the forward and the reversed processes, so the recovered micro fields are true, or at least nearly true.

(2) To develop a failure theory for sub-laminate matrix cracking. The theory is based on the lamina micro fields, which is recovered from the lamina macro field through the de-homogenization process. The new theory, termed inter-scale failure model, is applied to a number of known matrix cracking problems for which the macro field based failure theories have not been general and/or adequate enough.

In order to be problem-specific and give numerical results, the scope of the thesis is limited to

(1) Unidirectional fiber-reinforced systems and their laminates.

(2) The interested failures are in a class of matrix dominated tensile cracking in laminates under certain loading.

(3) Both the fibers and the matrix are assumed to be homogeneous and linearly elastic.

(4) The composite microstructure contains no defects and/or flaws, though matrix cracking is governed by a random material strength defined at the micro scale.

Numerical results in all illustrative examples are based on a E-glass/epoxy unidirectional system.

1.3 Organization of the Thesis

The remainder of the thesis is organized as follows.

In Chapter 2, a critical review of the currently available composite homogenization models for unidirectional fiber-reinforced systems is presented. In this regard, it should be noted that all prior homogenization models are formulated with the purpose of obtaining the effective properties of the composite; recovery of the composite micro fields is not intended. Consequently, most of the current models are constructed based on a single-fiber RVE(represented volume element), a modified single-fiber RVE, or an equivalent single-fiber RVE.

The review focuses on the implications of the concept of statistical homogeneity, the assumption of material symmetry, and the requirements imposed on the model construction. An in-depth analysis of each model is then conducted, as to the sources of

inconsistency, and hence the limit in application. In particular, the mechanics aspects in the model formulation and execution are examined within the confines of solid mechanics. Sources of inaccuracy in the computed results are identified.

The review and the in-depth model analysis provide the necessary guidelines for the formulation of a new model that should be devoid of most of the difficulties inherent in the current models. The new model should be capable of obtaining accurate effective composite properties in the homogenization process as well as recovering the micro fields in loaded laminates through the process of de-homogenization.

This new modelling approach is outlined in Chapter 3. Here, the model is based on a multi-fiber RVE whose selection is in accord with the actual fiber packing in the composite. In this way, the RVE truly reflects the microstructure of the composite at the fiber-matrix scale, and satisfies the requirements of the underlying statistical homogeneity and material symmetry assumptions. In addition, a center element containing one or more fibers is identified inside the RVE. It is then demonstrated that the micro field in the center element is insensitive to the details of the boundary conditions on the RVE, as long as they are statically equivalent; exact or nearly exact micro fields can be obtained inside the center element, provided the RVE is treated rigorously via a micromechanics analysis.

The effective properties of the composites are obtained through the usual boundary-value solution methods applied to homogenization. Numerical examples are presented to demonstrate the utility of this modelling technique, along with contrasting results rendered from other prevailing models.

Chapter 4 is devoted to the recovery of the micro fields in loaded laminates, using the

same multi-fiber RVE model. Here, it is first demonstrated that exact or nearly exact micro fields in loaded laminates can be recovered uniquely through a de-homogenization process. The latter involves a combination of rigorous laminate analysis and micromechanics solutions to the selected RVE.

Micro fields in several laminates are recovered. Some important material and geometric factors at the micro scale are studied, including the effects of local fiber-to-fiber interaction, the thermal residual stresses, the presence of micro defects, interaction with ply level constrains, and the response to global loading. The main emphasis is placed on the micro effects that influence the formation and propagation of matrix cracking in laminates under load.

An inter-scale failure theory is formulated in Chapter 5. The theory is based on the recovered laminate micro fields that contain the aforementioned micro effects. Material condition governing the onset of matrix cracking is based on the assumption that a tensile strength of random magnitude is present between two adjacent fibers, and matrix tensile cracking at the macro scale is a probabilistic event involving separation of collimated fibers in a finite volume, e.g. the size of the selected RVE, where the micro field is recovered and possible matrix cracking may occur.

The formulated inter-scale theory is applied to explain the observed matrix cracking events in several past experiments that are not explained consistently by any failure theory based on the laminate macro fields. The inter-scale theory consistently explains these events with predictive capability; it requires only a single material condition to be characterized at the fiber-matrix scale. A Weibull statistics based experiment for the characterization of this material condition is suggested.

The inter-scale theory serves as a connection between the micro scale material elements and the macro scale elements. This is clearly seen in the events of matrix dominated failures in laminates.

Conclusions from this study and recommendations for future research are discussed in Chapter 6.

Chapter 2: The Homogenization Theory: A Brief Review

The homogenization theory is the foundation of the mechanics of composite materials. This chapter presents a brief review of the theory, focusing on the basic assumptions and the prevailing models that have been developed for advanced fiber-reinforced composite systems.

Although the homogenization theory has also been applied to systems having time-dependent and/or non-linear characteristics, the present review is confined to linearly elastic systems.

2.1 Fundamental Elements in Homogenization

Consider the elemental unidirectionally fiber-reinforced (UD) composites. It consists of a matrix material in which continuous and aligned fibers are embedded. Thus, at the fiber-matrix scale, a distinct geometrical and material structure can be described. But in most engineering applications, the composite is assumed to be one statistically homogeneous material with a certain material symmetry. These are the fundamental assumptions in the theory of composite homogenization.

2.1.1 Statistical Homogeneity

For heterogeneous media, such as composites, the physical properties vary from point to point. In general, such media possess randomly distributed properties. For a complete

description of the physical properties, each is a random spatial function, and all of their joint probability distributions must be known. An "average" is defined in the ensemble sense over a selected sample volume of the medium. A statistically homogeneous medium is one whose property "averages" are independent of location of the sample volume. Thus, the sample volume is necessarily representative of such medium in a statistically sense. In composite literature, such a sample volume is known as **representative volume element** (RVE) [14, 21].

The statistical homogeneity assumption transforms heterogeneous composites to homogeneous ones; the average properties are termed as "effective properties". Henceforth, the conventional theories for continua can be used in the analyses of composites.

2.1.2 Material Symmetry

Material symmetry is another assumption to be made in conjunction with the statistical homogeneity assumption. For fibrous composites, symmetry is often inferred from the material and geometrical features at the fiber-matrix scale. For the UD system, three types of symmetry are usually considered depending on the fiber packing patterns or fiber arrays. Namely, orthotropy is assumed for a rectangular fiber array. Square symmetry is assumed for a square array. Transverse isotropy is assumed for a hexagonal array, or for a completely random array. [14, 21, 55]

The symmetry assumption, in effect, minimizes the number of directionally dependent properties for the homogenized composites. For linear elastic solids, complete anisotropy

requires 21 independent constants; orthotropic symmetry requires 9 independent constants; square symmetry requires 6 independent constants; and transverse isotropic symmetry requires 5 independent constants.

2.1.3 The Representative Volume Element (RVE)

The validity of the homogeneity and symmetry assumptions depends on the detailed microstructure at the fiber-matrix scale and thus the selection of the RVE [52].

Figure 2.1(a) shows a magnified cross-section of a UD graphite-epoxy composite. Over this cross-section, the average fiber volume content V_f is 0.71. At this scale, the fibers are not uniformly distributed. The local value of V_f can vary with the size and location of the sample volume over which V_f is computed. Figure 2.1(b) shows the dependence of V_f on the sample volume size. The values of V_f scatter greatly when the volume-element is small; the scatter decreases as the sample volume increases. In this case, V_f converges to 0.71 when the sample volume approaches the size containing 25 or more fibers. In the theory of homogenization, V_f is the key parameter on which other properties are based. Thus, in principle, the minimum sample volume over which V_f is independent of the sample location should be considered as the RVE.

The existence of material symmetry in the selected RVE depends on the fiber packing details as well as the sample size. For the composite shown in Figure 2.1 (a), fiber packing is random; here, a transverse isotropy may be assumed; i.e. a material isotropy in the composite cross-section may exist, statistically speaking. To verify this assumption, let a circular sample of radius of $3d_f$ (d_f being the fiber-diameter) be randomly taken from the composite cross-section. This sample would then contain about 20 fibers. A local x-y

coordinate is fixed at the center of the circle; the first and second area moments produced by the fiber cross-sections are computed. For isotropic symmetry, all first moments must vanish and the second moments (moments of inertia) $I_{xx} = I_{yy}$ and $I_{xy} = 0$. Moreover, these conditions must be met for any arbitrary rotation of the $x - y$ frame in the cross-sectional plane. Figure 2.1(c) shows the computed second moments I_{xx}, I_{yy} and I_{xy} versus the x-y rotation angle from 0 to 2π. In this case, conditions for plane isotropy are met for a sample containing 20 or more fibers.

Based on the above, a "proper" RVE containing 25 fibers or more meets the statistical homogeneity and transverse isotropy requirements. Any RVE with a size smaller than this would not meet the requirements.

2.1.4 Effective Elastic Moduli

When a composite specimen is under external load, micro stresses and strains are induced throughout the specimen. Ideally, the micro fields should be computed exactly, given the specimen and its fiber/matrix microstructure. According to the statistical homogeneity assumption, an appropriate RVE can be defined and isolated. On the RVE boundary, there exist definitive surface displacements and surface tractions. Within the RVE, there exist definitive stress field σ_{ij} and strain field ϵ_{ij}.

Through homogenization, the composite specimen is regarded as a body of an effective homogeneous material, whose mechanical behavior is described by a definitive constitutive law. This constitutive law can be determined based on the detailed fields in the selected RVE through an "averaging" procedure:

Specifically, if the exact micro fields σ_{ij} and ϵ_{ij} in the RVE are known under the

applied load, the averaged stresses and strains over the RVE are given by:

$$\bar{\sigma}_{ij} = \frac{1}{V}\int_V \sigma_{ij} dV \tag{2.1}$$

$$\bar{\epsilon}_{ij} = \frac{1}{V}\int_V \epsilon_{ij} dV, \tag{2.2}$$

where V is the volume of the RVE [1]. The averages are then treated as the effective stress and strain fields in the homogenized RVE. The relations between $\bar{\sigma}_{ij}$ and $\bar{\epsilon}_{ij}$ determine the "effective" constitutive law. When linear elasticity is assumed, the generalized Hook's law applies:

$$\bar{\sigma}_{ij} = C_{ijkl}\bar{\epsilon}_{kl}, \tag{2.3}$$

or

$$\bar{\epsilon}_{ij} = S_{ijkl}\bar{\sigma}_{kl}, \tag{2.4}$$

In the above, C_{ijkl} and S_{ijkl} are the effective stiffness and the effective compliance for the homogenized composite respectively.

The number of independent constants in C_{ijkl} is determined by the assumed symmetry. For UD composites, orthotropic, square, and transversely isotropic symmetries may be assumed. Figure 2.2 shows the principal material coordinate axes for a typical UD composite, where x_1 is in the fiber direction, and x_2, x_3 are in the transverse plane. The generalized Hook's law for orthotropy in the (x_1, x_2, x_3) frame can be expressed in the

contracted notation, involving 9 independent constants:

$$\begin{pmatrix} \sigma_1 \\ \sigma_2 \\ \sigma_3 \\ \sigma_4 \\ \sigma_5 \\ \sigma_6 \end{pmatrix} = \begin{pmatrix} C_{11} & C_{12} & C_{13} & 0 & 0 & 0 \\ & C_{22} & C_{23} & 0 & 0 & 0 \\ & & C_{33} & 0 & 0 & 0 \\ & & & C_{44} & 0 & 0 \\ & & & & C_{55} & 0 \\ & & & & & C_{66} \end{pmatrix} \begin{pmatrix} \epsilon_1 \\ \epsilon_2 \\ \epsilon_3 \\ \epsilon_4 \\ \epsilon_5 \\ \epsilon_6 \end{pmatrix}, \tag{2.5}$$

where $\epsilon_1 = \epsilon_{11}$, $\epsilon_2 = \epsilon_{22}$, $\epsilon_3 = \epsilon_{33}$, $\epsilon_4 = 2\epsilon_{23}$, $\epsilon_5 = 2\epsilon_{31}$, and $\epsilon_6 = 2\epsilon_{12}$.

In the special cases where the fibers are packed in a square array, a square symmetry can be assumed. This results in $C_{22} = C_{33}$, $C_{12} = C_{13}$, $C_{55} = C_{66}$. The number of independent constants reduces to six.

In the case of transverse isotropy, $C_{44} = \dfrac{C_{22} - C_{23}}{2}$, reducing the number of independent constants to five.

In practice, the so-called engineering constants are used, which can be expressed in terms of C_{ij}:

$$\begin{aligned} E_{11} &= \frac{C}{C_{22}C_{33} - C_{23}^2} \\ E_{22} &= \frac{C}{C_{33}C_{11} - C_{13}^2} \\ E_{33} &= \frac{C}{C_{11}C_{22} - C_{12}^2} \\ \nu_{12} &= \frac{C_{13}C_{23} - C_{12}C_{33}}{C_{23}^2 - C_{22}C_{33}} \\ \nu_{13} &= \frac{C_{12}C_{23} - C_{13}C_{22}}{C_{23}^2 - C_{22}C_{33}} \\ \nu_{23} &= \frac{C_{12}C_{13} - C_{23}C_{11}}{C_{13}^2 - C_{33}C_{11}} \end{aligned} \tag{2.6}$$

$$
\begin{aligned}
G_{23} &= C_{44} \\
G_{31} &= C_{55} \\
G_{12} &= C_{66},
\end{aligned}
$$

where

$$C = C_{11}C_{22}C_{33} - C_{11}C_{23}^2 - C_{22}C_{13}^2 - C_{33}C_{12}^2 + 2C_{12}C_{23}C_{13}. \tag{2.7}$$

Alternatively, the generalized Hook's law can be expressed in terms of the effective compliances. For the orthotropic case,

$$\begin{pmatrix} \epsilon_1 \\ \epsilon_2 \\ \epsilon_3 \\ \epsilon_4 \\ \epsilon_5 \\ \epsilon_6 \end{pmatrix} = \begin{pmatrix} S_{11} & S_{12} & S_{13} & 0 & 0 & 0 \\ & S_{22} & S_{23} & 0 & 0 & 0 \\ & & S_{33} & 0 & 0 & 0 \\ & & & S_{44} & 0 & 0 \\ & & & & S_{55} & 0 \\ & & & & & S_{66} \end{pmatrix} \begin{pmatrix} \sigma_1 \\ \sigma_2 \\ \sigma_3 \\ \sigma_4 \\ \sigma_5 \\ \sigma_6 \end{pmatrix}. \tag{2.8}$$

The engineering constants can also be given in terms of S_{ij}:

$$
\begin{aligned}
E_{11} &= \frac{1}{S_{11}} \\
E_{22} &= \frac{1}{S_{22}} \\
E_{33} &= \frac{1}{S_{33}} \\
\nu_{12} &= -\frac{S_{12}}{S_{11}} \\
\nu_{13} &= -\frac{S_{13}}{S_{11}}
\end{aligned} \tag{2.9}
$$

$$\begin{aligned} \nu_{23} &= -\frac{S_{23}}{S_{22}} \\ G_{23} &= \frac{1}{S_{44}} \\ G_{31} &= \frac{1}{S_{55}} \\ G_{12} &= \frac{1}{S_{66}}. \end{aligned}$$

2.1.5 Mechanics Procedures in Homogenization

Determination of the elastic constants C_{ij} in (2.5), or the engineering constants in (2.6), depends on the description of the selected RVE, the manner in which the boundary conditions are imposed, and the rigor in solving the boundary value (B-V) problems for the micro fields. This brings out two major difficulties in obtaining accurate C_{ij}.

First of all, the microstructure of the UD composites at the fiber-matrix level may contain random elements other than the matrix and fibers, e.g. coating, fiber-matrix interface disbonds, matrix micro-voids, etc.. It is difficult to describe the geometry and the material in such a microstructure in precision; in addition, microstructures are often simplified in order to make the associated B-V problems mathematically tractable. For instance, fibers are assumed to be perfectly round; have the same diameters; each fiber is bonded perfectly to the matrix , etc.

Another difficulty is that, when the RVE is isolated from the composite, mixed stresses and strains (or displacement) are distributed on its boundary. The exact distribution of these boundary agencies are unknown until the exact micro fields are computed. Thus, it is almost always necessary to impose statically equivalent boundary conditions on the RVE.

Figure 2.3 illustrates the commonly followed procedure for determining the effective moduli for the UD composites. First, the UD composite cross-section is examined at the fiber-matrix scale, so as to guide the selection of the RVE with a proper size and with a relevantly assumed material symmetry. A set of independent boundary conditions sufficient to determine the required number of constants in C_{ij} are then imposed on the RVE. The associated boundary-value problems are solved for the micro fields. The averaging procedure is performed over the RVE to obtain $\bar{\sigma}_{ij}$ and $\bar{\epsilon}_{ij}$, as in Equations (2.1) and (2.2). Finally, the effective constants in C_{ijkl} or S_{ijkl} are determined within the premise of Equation (2.3) or (2.4).

In the literature, many models have been advanced for the evaluation of the effective moduli for UD composites. Depending on the details of the selected RVE and the rigorousness in the B-V solution schemes, these models can be grouped in four different. These will be discussed in the following section.

2.2 Review on Existing Homogenization Models

In this section, the chronological development on the selection of RVE for UD composites and the analysis methods for the resulting B-V problems are briefly reviewed and discussed.

2.2.1 Rule-of-Mixture

The rule-of-mixture models are derived from the mechanics of material approach [27, 46]. Rule-of-mixture embodies several simplifying assumptions regarding the mechanical behaviors of the composites. A typical RVE is shown in Figure 2.4. It consists only of

the fiber and matrix. This representation is applicable to both the $x_1 - x_2$ and $x_1 - x_3$ planes, and it is valid for a transversely isotropic symmetry. The only geometric parameter defining the microstrucutre in the RVE is the fiber volume fraction V_f. The details of the fiber packing in the transverse $x_2 - x_3$ plane are irrelevant.

On the basis of this RVE, one can predict four elastic constants: E_{11}, E_{22}, ν_{12}, and G_{12}. The associated boundary conditions on the RVE are: (a) an axial strain ϵ_1 in the fiber direction; (b) a transverse stress σ_2 normal to the fiber direction; and (c) a pure shear stress τ_{12}. Condition (a) yields the longitudinal Young's modulus E_{11} and the axial Poisson's ratio ν_{12}:

$$E_{11} = E_f V_f + E_m V_m = E_f V_f + E_m(1 - V_f)\,, \tag{2.10}$$

$$\nu_{12} = \nu_f V_f + \nu_m V_m = \nu_f V_f + \nu_m(1 - V_f)\,. \tag{2.11}$$

where V_f and V_m are the volume fractions of the fiber and matrix, respectively. E_f and E_m are the Young's modulus for the fiber and matrix; and ν_f and ν_f are the Poisson's ratio of the fiber and matrix, respectively.

Condition (b) and (c) yield respectively the transverse Young's modulus E_{22} and the axial shear modulus G_{12}:

$$\frac{1}{E_{22}} = \frac{V_f}{E_f} + \frac{V_m}{E_m}\,, \tag{2.12}$$

$$\frac{1}{G_{12}} = \frac{V_f}{G_f} + \frac{V_m}{G_m}\,, \tag{2.13}$$

where G_f and G_m are the shear modulus of the fiber and matrix, respectively.

The Rule-of-mixture provides a quick estimation of the effective moduli in a simple

way. The four constants can describe the composites under plane-stress conditions. Since the fiber packing in the $x_2 - x_3$ plane is omitted in the RVE description, the effective moduli in the $x_2 - x_3$ plane cannot be determined. Moreover, in solving the B-V problems, one-dimensional stress state is assumed. These simplifications lead to inaccurate micro stress and strain fields in the RVE.

2.2.2 Variational Bounding Models

The variational approach is an attempt to determine the effective moduli for the composite as a three dimensional (3-D) continuum. It involves the application of the minimum energy principles to set the bounds for the effective moduli. Development of this approach is as follows:

Suppose the exact boundary conditions on the selected RVE could be specified; the induced micro fields can be computed exactly. The averaged stresses $\bar{\sigma}_{ij}$ and strains $\bar{\epsilon}_{ij}$ are expressed through (2.1) and (2.2); and the strain energy stored in the RVE is given by

$$U = \int_V \frac{1}{2}\sigma_{ij}\epsilon_{ij}dV\,, \tag{2.14}$$

where V is the volume of the RVE.

Now, for the composite (i.e. the RVE) as a continuum, the stresses and strains in the RVE under the same boundary conditions are given by (2.1) and (2.2); the associated strain energy stored therein is given by

$$\bar{U} = \int_V \frac{1}{2}\bar{\sigma}_{ij}\bar{\epsilon}_{ij}dV\,. \tag{2.15}$$

Now, if the energies in (2.14) and (2.15) are equal, the effective constants in the homogenized RVE are uniquely determined.

Since the exact boundary conditions on the RVE are unknown before the true micro fields are obtained, a linear displacement condition may be prescribed on the RVE boundary

$$u_i^0 = \epsilon_{ij}^0 x_j \,, \tag{2.16}$$

where ϵ_{ij}^0 are the boundary strains. This results in a uniform strain field ϵ_{ij}^0 in the homogenized RVE. Moreover, the associated stress field is computed through the generalized Hook's law: $\bar{\sigma}_{ij} = C_{ijkl}\,\epsilon_{kl}^0$. The field is also uniform throughout the RVE. The strain energy stored therein is given by

$$\bar{U}^{\epsilon^0} = \int_V \frac{1}{2} C_{ijkl} \epsilon_{kl}^0 \epsilon_{ij}^0 dV \,. \tag{2.17}$$

Now, if the micro fields in the RVE under the same boundary condition in (2.16) is solved, the stored energy U^{ϵ^0} is computed using (2.14).

It follows from the principle of minimum potential energy that

$$\bar{U}^{\epsilon^0} \leq U^{\epsilon^0} \,. \tag{2.18}$$

By the equality in (2.18), the upper bounds for the effective stiffness in C_{ijkl} are determined.

Alternatively, a uniform surface traction may be prescribed on the RVE:

$$T_i^0 = \sigma_{ij}^0 n_j \,. \tag{2.19}$$

This produces a uniform stress field σ_{ij}^0 in the RVE as a continuum. The corresponding strain field is computed via (2.8): $\bar{\epsilon}_{ij} = S_{ijkl}\,\sigma_{kl}^0$. The latter is also uniform throughout the RVE. The stored strain energy is given by

$$\bar{U}^{\sigma^0} = \int_V \frac{1}{2} S_{ijkl} \sigma_{kl}^0 \sigma_{ij}^0 dV \,. \tag{2.20}$$

The micro fields in the RVE under the same boundary condition of (2.19) can be solved rigorously; the stored strain energy U^{σ^0} is computed again via (2.14).

It follows from the principle of minimum complementary energy that

$$\bar{U}^{\sigma^0} \leq U^{\sigma^0} \,. \tag{2.21}$$

The upper bounds for the effective compliance in S_{ijkl} are determined by the equality of (2.21). The inverse of $\mathbf{S}$ yields $\mathbf{C}$; the upper bounds for S_{ijkl} correspond to the lower bounds for C_{ijkl}.

Paul [37] was apparently the first to use the bounding procedure to determine the moduli of alloyed metals. Hashin [13], and Hashin and Shtrikman [17] derived bounds for a matrix material containing spherical inclusions. Hill [22] treated the UD composites characterized only by V_f; the bounds for E_{11}, ν_{12}, and K_{23} were obtained. Hashin and Rosen [16] considered the UD composites as a composite cylinder assembly(CCA), and

derived bounds for all 5 effective moduli under the assumption of transversely isotropic symmetry.

In the CCA model, each fiber of radius r_f is surrounded by a concentric matrix shell of the outer radius r_m, where r_f and r_m are connected through $V_f = \frac{r_f^2}{r_m^2}$. The RVE contains a single fiber with a concentric matrix shell, as depicted in Figure 2.5. Two types of fiber packing can be represented by the CCA model: the hexagonal array with identical fibers and the random array with fibers of arbitrary diameters. Figure 2.6(a) shows the hexagonal array, where V_1 denotes the volume of the composite cylinder and V_2 denotes the remaining volume. Figure 2.6 (b) shows the random array, where the composite cylinders have irregular shapes. The length of the cylinders are large compared to fiber diameter; fiber end effects are ignored in the Saint-Venant sense. The resulting B-V problems are reduced to the plane strain or the generalized plane strain types.

For transverse isotropy, five unique sets of B.C.s (either stress or displacement) are specified in order to determine the five independent constants. The constants selected by Hashin and Rosen [16] are K_{23}, G_{23}, G_{12}, E_{11}, and C_{11}. K_{23} is the plane strain bulk modulus of the composite. The corresponding boundary conditions for determining each of the five constants are listed in Table (2.2.2).

Under each B.C., the micro stress and strain fields in the RVE can be obtained analytically owing to axial symmetry of the RVE. Furthermore, elastic constants are decoupled in the strain energy expression.

In the case of the hexagonal array, the upper and lower bounds for the aforementioned five moduli are obtained. The detail expressions are found in [16].

In the case of random array, the composite is represented by an assembly of composite

Table 2.1: Five effective elastic moduli with corresponding B.C.s in the CCA model, after [16].

	Strain B.C.	Displacement B.C.	Stress B.C.	Traction B.C.
Plain-strain bulk modulus K_{23}	$\epsilon^0_{11} = 0$ $\epsilon^0_{22} = \epsilon^0$ $\epsilon^0_{33} = \epsilon^0$ $\epsilon^0_{ij} = 0,$ $i \neq j$	$u^0_1 = 0$ $u^0_2 = \epsilon^0\, x_2$ $u^0_3 = \epsilon^0\, x_3$	$\sigma^0_{11} \neq 0$ $\sigma^0_{22} = \sigma^0$ $\sigma^0_{33} = \sigma^0$ $\sigma^0_{ij} = 0,$ $i \neq j$	$T^0_1 \neq 0$ $T^0_2 = \sigma^0\, x_2$ $T^0_3 = \sigma^0\, x_3$
Transverse shear modulus G_{23}	$\epsilon^0_{ii} = 0,$ $i = 1, 2, 3$ $\epsilon^0_{12} = 0$ $\epsilon^0_{31} = 0$ $\epsilon^0_{23} = \gamma^0/2$ $\epsilon^0_{32} = \gamma^0/2$	$u^0_1 = 0$ $u^0_2 = \gamma^0\, x_3/2$ $u^0_3 = \gamma^0\, x_2/2$	$\sigma^0_{ii} = 0,$ $i = 1, 2, 3$ $\sigma^0_{12} = 0$ $\sigma^0_{31} = 0$ $\sigma^0_{23} = \tau^0$	$T^0_1 = 0$ $T^0_2 = \tau^0\, x_3$ $T^0_3 = \tau^0\, x_2$
Longitudinal shear modulus G_{12}	$\epsilon^0_{ii} = 0,$ $i = 1, 2, 3$ $\epsilon^0_{12} = \gamma^0/2$ $\epsilon^0_{31} = \gamma^0/2$ $\epsilon^0_{23} = 0$	$u^0_1 = \gamma^0\, x_2/2$ $u^0_2 = \gamma^0\, x_1/2$ $u^0_3 = 0$	$\sigma^0_{ii} = 0,$ $i = 1, 2, 3$ $\sigma^0_{12} = \tau^0$ $\sigma^0_{31} = \tau^0$ $\sigma^0_{23} = 0$	$T^0_1 = \tau^0\, x_2$ $T^0_2 = \tau^0\, x1$ $T^0_3 = 0$
Longitudinal Young's modulus E_{11}	$\epsilon^0_{11} = \epsilon^0$ $\epsilon^0_{22} = -\mu\, \epsilon^0$ $\epsilon^0_{33} = -\mu\, \epsilon^0$ $\epsilon^0_{ij} = 0,$ $i \neq j$	$u^0_1 = \epsilon^0\, x_1$ $u^0_2 = -\mu\, \epsilon^0\, x_2$ $u^0_3 = -\mu\, \epsilon^0\, x_3$	$\sigma^0_{11} = \sigma^0$ $\sigma^0_{22} = 0$ $\sigma^0_{33} = 0$ $\sigma^0_{ij} = 0,$ $i \neq j$	$T^0_1 = \sigma^0\, x_1$
	$T^0_2 = 0$, $T^0_3 = 0$, for both displacement and traction B.C.			
Modulus C_{11}	$\epsilon^0_{11} = \epsilon^0$ $\epsilon^0_{22} = 0$ $\epsilon^0_{33} = 0$ $\epsilon^0_{ij} = 0,$ $i \neq j$	$u^0_1 = \epsilon^0\, x_1$	$\sigma^0_{11} = \sigma^0$	$T^0_1 = \sigma^0\, x_1$
	$u^0_2 = 0, u^0_3 = 0$, for both displacement and traction B.C.			

cylinders, having varying fiber diameters but the same V_f. The outer irregular surfaces of composite cylinders are approximated by circular cylinders. The remaining volume is filled out progressively by composite cylinders of smaller and smaller cross sections. Again, the RVE contains a single fiber with a concentric matrix shell, although the diameter of the fiber is arbitrarily small or large. The same set of boundary conditions are applied; the micro fields in each B-V problems are solved exactly. In this case, except for G_{23}, the bounds for K_{23}, G_{12}, E_{11}, and C_{11} coincide. They are given in [15], as

$$K_{23} = K_m + \frac{V_f}{\dfrac{1}{K_f - K_m} + \dfrac{V_m}{K_m + G_m}} \tag{2.22}$$

$$E_{11} = E_m V_m + E_f V_f + \frac{4\,(\nu_f - \nu_m)^2 V_m V_f}{\dfrac{V_m}{K_f} + \dfrac{V_f}{K_m} + \dfrac{1}{G_m}} \tag{2.23}$$

$$G_{12} = G_m + \frac{V_f}{\dfrac{1}{G_f - G_m} + \dfrac{V_m}{2G_m}} \tag{2.24}$$

$$C_{11} = E_{11} + 4\,\mu^2\,K_{23}\,. \tag{2.25}$$

In Equation (2.25), μ is a part of the boundary condition. Physically, μ is the axial Poisson's ratio ν_{12}, see Table 2.2.2. It is evaluated along with E_{11} under the conditions $T_2^0 = 0$ and $T_3^0 = 0$. Its expression is

$$\mu = \nu_{12} = \nu_m V_m + \nu_f V_f + \frac{(\nu_f - \nu_m)(1/K_m - 1/K_f)V_m V_f}{\dfrac{V_m}{K_f} + \dfrac{V_f}{K_m} + \dfrac{1}{G_m}}\,. \tag{2.26}$$

The bounds for G_{23} are

$$G_{23}^{up} = G_m \frac{\left(1+\alpha V_f^3\right)(\rho+\beta_1 V_f) - 3V_f V_m^2 \beta_1^2}{\left(1+\alpha V_f^3\right)(\rho - V_f) - 3V_f V_m^2 \beta_1^2} \tag{2.27}$$

$$G_{23}^{low} = G_m \left[1 + \frac{V_f}{\frac{1}{\gamma-1} + \frac{V_m}{1+\beta_1}}\right], \tag{2.28}$$

where

$$\begin{aligned} \alpha &= \frac{\beta_1 - \gamma\beta_2}{1+\gamma\beta_2} \\ \rho &= \frac{\gamma+\beta_1}{\gamma-1} \\ \gamma &= \frac{G_f}{G_m} \\ \beta_1 &= \frac{1}{3-4\nu_m} \\ \beta_2 &= \frac{1}{3-4\nu_f}. \end{aligned} \tag{2.29}$$

The related transverse moduli E_{22} and ν_{23} also have bounds as they are related to G_{23} [16]. In Equations (2.22-2.29), V_f and V_m are the volume fraction of fiber and matrix respectively; E_f and E_m, the Young's moduli; ν_f and ν_m, the Poisson's ratios; G_f and G_m, the shear moduli; K_f and K_m, the bulk moduli.

Hashin and Rosen's CCA model gives the upper and lower bounds for the five moduli in the case of the hexagonal array. In the case of the random array, approximated by CCAs with arbitrary small diameters to fill the voids, it leads to coincided bounds for 4 moduli and a set of bounds for G_{23}. It should be noted that, when the bounds coincide, it implies that the uniform displacement and traction boundary conditions prescribed on

the RVE are equivalent, or, they mutually produce each other. Moreover, the respective micro fields obtained are the same. However, because the RVE contains only a single fiber, interactions with neighboring fibers are omitted. Hence, the computed micro fields are not the true micro fields in the composite. Consequently, the effective moduli computed are not accurate in the logical sense, even if the bounds coincide.

2.2.3 Self-Consistent Model

The "self consistent model" is aimed to determine unique solutions for the effective moduli in a heterogeneous medium. Here, the selected RVE is embedded in the homogenized medium whose properties are to be determined. The calculation procedures are similar to that described previously. The only difference is that the applied load is now prescribed in the far field of the homogenized medium.

The model was first applied to model polycrystals by Hershey [20], and Budiansky and Wu [3]. For UD fiber-reinforced composites, Hill [23] used a single fiber embedded in an unbounded effective medium; the effective moduli were computed by assuming transverse isotropy. Hermans [19] considered a fiber surrounded by a matrix shell as the basic RVE, which is in turn embedded in the effective composite, see Figure 2.7. Hermans was able to obtain an approximate solution for G_{23}, due to inaccuracy in the micro field solution. Christensen and Lo [4] used the same model and solved the stresses and strains in the RVE exactly; so a unique solution for G_{23} was obtained.

The 3-phase self-consistent model provides unique solutions for all of the five effective elastic moduli. In addition, the fiber-to-fiber interactions are included in the average sense by surrounding infinite homogenized medium. Still, the representation of the RVE

is inexact; the computed effective moduli are somewhat approximate.

2.2.4 Periodic Model

The periodic model is developed for the so-called "model" composites, whose fiber packing exhibits a certain periodicity in the $x_2 - x_3$ plane. Examples includes rectangular, square, and hexagonal arrays. For these arrays, the smallest repeating element is taken as the RVE, which in most cases contains a single fiber. When the composite specimen is subjected to a uniform far field loading, each and every RVE will undergo identical deformation; a certain periodicity then exists in the displacement, stress and strain fields. When the RVE is isolated from the specimen, periodic boundary conditions are prescribed in terms of both displacements and tractions. Clearly, the description of, and the solution to the B-V problem must be exact; the compatibility and continuity between the isolated RVE and its neighboring ones are preserved.

Heaton [18] described the compatible displacements and traction boundary conditions on the RVE for a square array. Aboudi [1] analyzed a similar RVE containing a fiber of square cross-section. Sun and Vaidya [42] detailed the periodic displacement boundary conditions for composites of square and hexagonal arrays under various far field loading conditions. In most cases, the micro fields need to be solved numerically by either the 3-D finite element method [42] or the asymptotic solution method [25, 44]. However, the effective constants are multiply coupled in each of the applied far-field loading conditions.

Yuan, et al. [55] treated the UD composite with a rectangular array where orthotropic symmetry is assumed. Six sets of far-field loading conditions are prescribed and the corresponding boundary conditions on the isolated RVE described accordingly. In each

case, the resulting B-V problem could be formulated in the generalized plane strain field (in the $x_2 - x_3$ plane).

Figure 2.8 shows the RVE cross-section in the $x_2 - x_3$ plane for the rectangular array. The size of the RVE is $2a \times 2b$. The following periodic boundary conditions are specified:

$$u_i = \epsilon^0_{ij}\, x_j + u^*_i, \quad u^*_i \text{ is periodic on } \partial V,\ i,j = 1,2,3 \tag{2.30}$$

$$t_i = \sigma^0_{ij}\, n_j \text{ is anti} - \text{periodic on } \partial V,\ i,j = 1,2,3\,. \tag{2.31}$$

In the above, u_i is the displacement vector expressed in terms of the far-field uniform strain ϵ^0_{ij}; u^*_i is the periodic part of u_i. The latter is a self-equilibrated part of the micro field solution; it does not contribute to the homogenized macro fields [38].

When the above B-V problem is solved by a numerical method, e.g. via a finite element method, the conditions in (2.30) and (2.31) can be represented by

$$u_i(P_2) - u_i(P_1) = \epsilon^0_{ij}\ [x_j(P_2) - x_j(P_1)]\ , \tag{2.32}$$

and

$$(t_i)_{P_2} = -(t_i)_{P_1}\,. \tag{2.33}$$

P_1 and P_2 are a pair of corresponding points on the RVE bounding surface, as shown in Figure 2.8.

Table 2.2 lists the detailed far-field uniform strain, the corresponding displacement and traction boundary conditions on the RVE for each of the six sets of loading. Note

that the first set determines the constants C_{11}, C_{12}, and C_{13}; the second set determines C_{22} and C_{23}; the third to sixth sets determine C_{33}, C_{44}, C_{55}, and C_{66}, respectively.

A simple reduction can readily be made for composites of a square array, since the size of the RVE is then $2a \times 2a$. Thus, Table2.2 can be used for the square array by setting $a = b$. The third and fifth sets of loadings are redundant; so the effective constants $C_{33} = C_{22}$ and $C_{55} = C_{66}$. The first set yields $C_{13} = C_{12}$.

Recently, Li [32] applied the concept of translational symmetry to describe the periodic boundary conditions for UD composites having a square or a hexagonal array. Figure 2.9 displays the RVE for the square array and the mutually orthogonal translational symmetry axes in the $x_2 - x_3$ plane. The RVE for the hexagonal array is shown in Figure 2.10, along with the three axes of translational symmetry. As mentioned before, square symmetry is assumed for the square array; transverse isotropy is assumed for the hexagonal array. Details in the required sets of far-field loading, the corresponding periodic boundary conditions on the RVE, and the effective constants to be determined in each loading set are presented in Appendix A.1. It should be noted that the resulting B-V problems are three dimensional in nature. A 3-D numerical computational routines is needed to solve the micro fields.

For"model" composites with periodic fiber packings, it is possible to describe compatible displacement and traction boundary conditions on the isolated RVE, for each set of admissible far-field loading condition. If the resulting B-V problem is solved exactly, the computed micro fields in the RVE are the same as the true micro fields that actually exist in the composite. Consequently, the computed effective constants for the homogenized composite are exact. The only limitation is that the assumed periodicity in the fiber

Table 2.2: Periodic boundary conditions and corresponding effective constants, after [55]

Elastic and mathematic constants	Far-field uniform strains	Displacement conditions on RVE	Traction conditions on RVE
C_{11} C_{12} C_{13} (E_{11}) (ν_{12}) (ν_{13})	$\epsilon_{11} = \epsilon^0_{11}$ $\epsilon_{22} = 0$ $\epsilon_{33} = 0$ $\epsilon^0_{ij} = 0$ $i \neq j$ $i, j = 1, 2, 3$	$u_2(a, x_3) = u_2(-a, x_3)$ $u_3(a, x_3) = u_3(-a, x_3)$ $u_2(x_2, b) = u_2(x_2, -b)$ $u_3(x_2, b) = u_3(x_2, -b)$ $u_1(x_1, x_2, x_3) = \epsilon^0_{11} x_1$	$\sigma_{22}(a, x_3) = \sigma_{22}(-a, x_3)$ $\sigma_{23}(a, x_3) = \sigma_{23}(-a, x_3)$ $\sigma_{33}(x_2, b) = \sigma_{33}(x_2, -b)$ $\sigma_{23}(x_2, b) = \sigma_{23}(x_2, -b)$
C_{22} C_{23} (E_{22}) (ν_{23})	$\epsilon_{11} = 0$ $\epsilon_{22} = \epsilon^0_{22}$ $\epsilon_{33} = 0$ $\epsilon^0_{ij} = 0,$ $i \neq j,$ $i, j = 1, 2, 3$	$u_2(a, x_3) = u_2(-a, x_3) + 2a\epsilon^0_{22}$ $u_3(a, x_3) = u_3(-a, x_3)$ $u_2(x_2, b) = u_2(x_2, -b)$ $u_3(x_2, b) = u_3(x_2, -b)$ $u_1(x_1, x_2, x_3) = 0$	$\sigma_{22}(a, x_3) = \sigma_{22}(-a, x_3)$ $\sigma_{23}(a, x_3) = \sigma_{23}(-a, x_3)$ $\sigma_{33}(x_2, b) = \sigma_{33}(x_2, -b)$ $\sigma_{23}(x_2, b) = \sigma_{23}(x_2, -b)$
C_{33} (E_{33})	$\epsilon_{11} = 0$ $\epsilon_{22} = 0$ $\epsilon_{33} = \epsilon^0_{33}$ $\epsilon^0_{ij} = 0$ $i \neq j,$ $i, j = 1, 2, 3$	$u_2(a, x_3) = u_2(-a, x_3)$ $u_3(a, x_3) = u_3(-a, x_3)$ $u_2(x_2, b) = u_2(x_2, -b)$ $u_3(x_2, b) = u_3(x_2, -b) + 2b\epsilon^0_{33}$	$\sigma_{22}(a, x_3) = \sigma_{22}(-a, x_3)$ $\sigma_{23}(a, x_3) = \sigma_{23}(-a, x_3)$ $\sigma_{33}(x_2, b) = \sigma_{33}(x_2, -b)$ $\sigma_{23}(x_2, b) = \sigma_{23}(x_2, -b)$
C_{44} (G_{23})	$\gamma_{23} = \gamma^0_{23}$ other $\epsilon_{ij} = 0$	$u_2(a, x_3) = u_2(-a, x_3)$ $u_3(a, x_3) = u_3(-a, x_3) + a\gamma^0_{23}$ $u_2(x_2, b) = u_2(x_2, -b) + b\gamma^0_{23}$ $u_3(x_2, b) = u_3(x_2, -b)$ $u_1 = 0$	$\sigma_{22}(a, x_3) = \sigma_{22}(-a, x_3)$ $\sigma_{23}(a, x_3) = \sigma_{23}(-a, x_3)$ $\sigma_{33}(x_2, b) = \sigma_{33}(x_2, -b)$ $\sigma_{23}(x_2, b) = \sigma_{23}(x_2, -b)$
C_{55} (G_{13})	$\gamma_{13} = \gamma^0_{13}$ other $\epsilon_{ij} = 0$	$u_1(a, x_3) = u_1(-a, x_3)$ $u_1(x_2, b) = u_1(x_2, -b) + 2b\gamma^0_{13}$ $u_2 = u_3 = 0$	$\sigma_{23}(a, x_3) = \sigma_{23}(-a, x_3)$ $\sigma_{23}(x_2, b) = \sigma_{23}(x_2, -b)$
C_{66} (G_{12})	$\gamma_{12} = \gamma^0_{12}$ other $\epsilon_{ij} = 0$	$u_1(a, x_3) = u_1(-a, x_3) + 2a\gamma^0_{12}$ $u_1(x_2, b) = u_1(x_2, -b)$ $u_2 = u_3 = 0$	$\sigma_{23}(a, x_3) = \sigma_{23}(-a, x_3)$ $\sigma_{23}(x_2, b) = \sigma_{23}(x_2, -b)$

packing must exist.

2.2.5 Summary and Discussion

In this chapter, a review of the theory of composite homogenization, the basic assumptions and limitations, the chronological development of homogenization models and computational methods has been presented. The theory of composite homogenization has progressed from a rudimentary approximation to a more rigorous and scientific quest over a period of 40 years.

For the most part, the homogenization models have employed an RVE that contains only a single fiber, such as the CCA model and the 3-phase self-consistent model. The single fiber varieties do not always meet the requirement of the underlying assumptions of statistical homogeneity and material symmetry. Moreover, fiber-to-fiber interaction effects are often omitted e.g. in the CCA model, or approximated e.g. in the 3-phase self-consistent model. In these cases, the computed micro fields as well as effective moduli are inexact. The periodic models enable exact descriptions of the boundary conditions on the RVE and the fiber-to-fiber interactions. Though the micro fields and the effective moduli can be determined exactly, the periodic models are limited to the so-called "model" composites with periodic fiber arrays. In real composites, the fiber distribution almost always exhibits a certain degree of randomness; periodicity in fiber packing does not exist.

Micro fields in loaded composite structures are increasingly desired because it is believed that failures in composites originate in the microstructure; hence, a detailed micro field may provide the needed information for explaining composite failure. A rigorous

composite homogenization model is essential for obtaining the exact micro fields in composites.

In order to accomplish this objective, the homogenization model must be based on an RVE that is truly representative of the actual composite, and consistent boundary conditions must be prescribed when the RVE is isolated. Only then, exact micro field solutions in the RVE can be obtained along with accurate effective moduli for the homogenized composite.

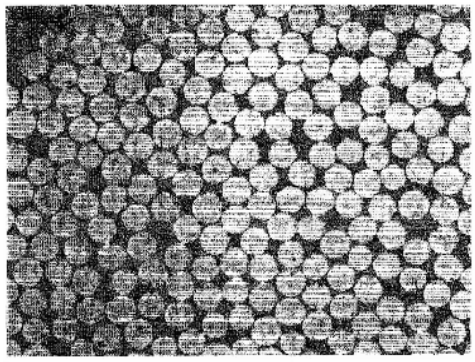

(a)

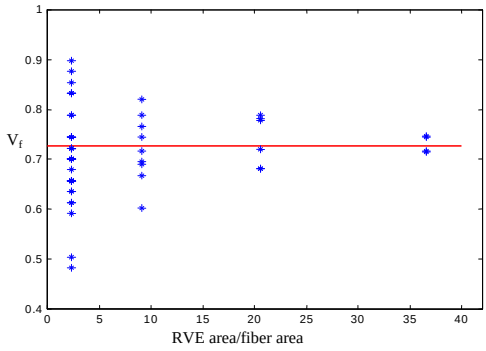

(b)

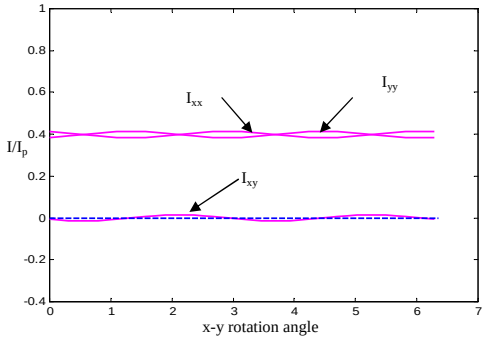

(c)

Figure 2.1: A graphite/epoxy UD composite (a) cross section; (b) dependence of V_f on area-element over which V_f is computed;(c) I_{xx}, I_{yy} and I_{xy} versus the x-y rotation angle from 0 to 2π, where I_{xx}, I_{yy} and I_{xy} are normalized by the polar moments of inertia of the circular area, $I_p = (\pi/2)(3d_f)^4$.

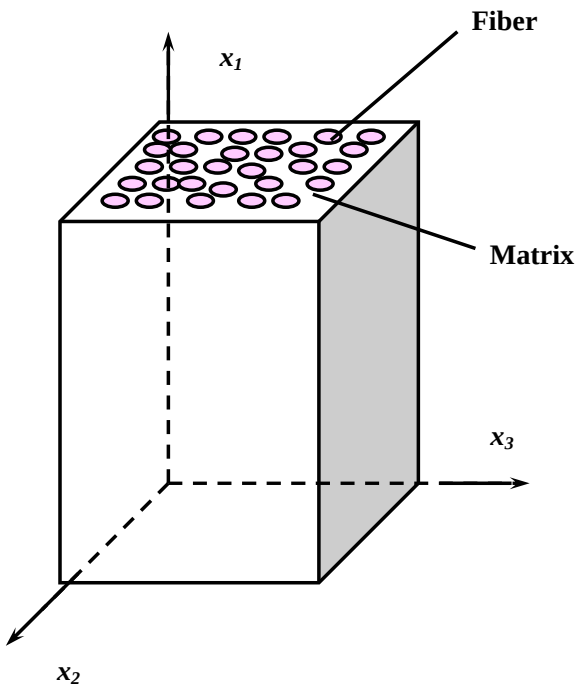

Figure 2.2: A typical unidirectional composite referred to Cartesian coordinate system.

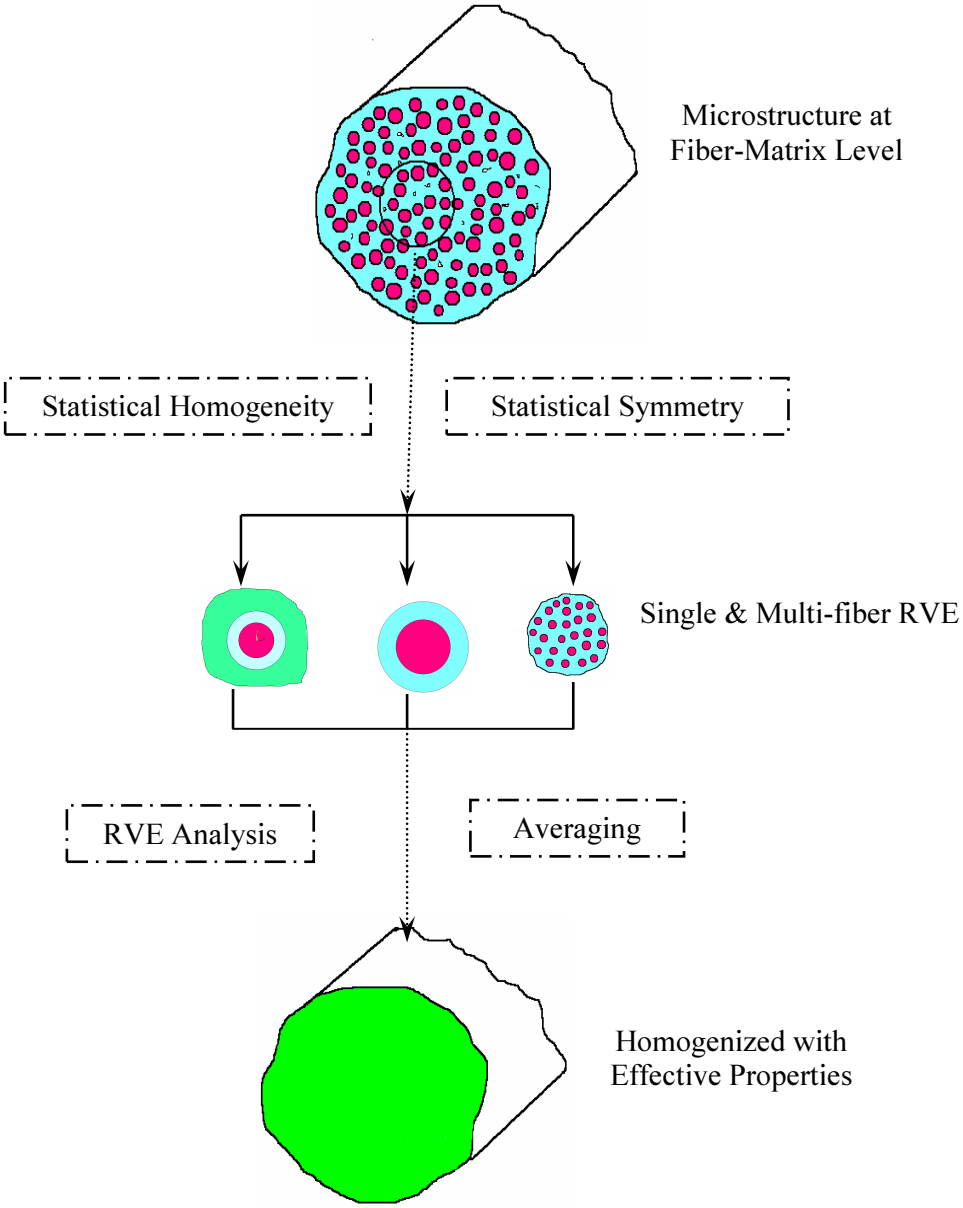

Figure 2.3: Common procedure in composite homogenization process.

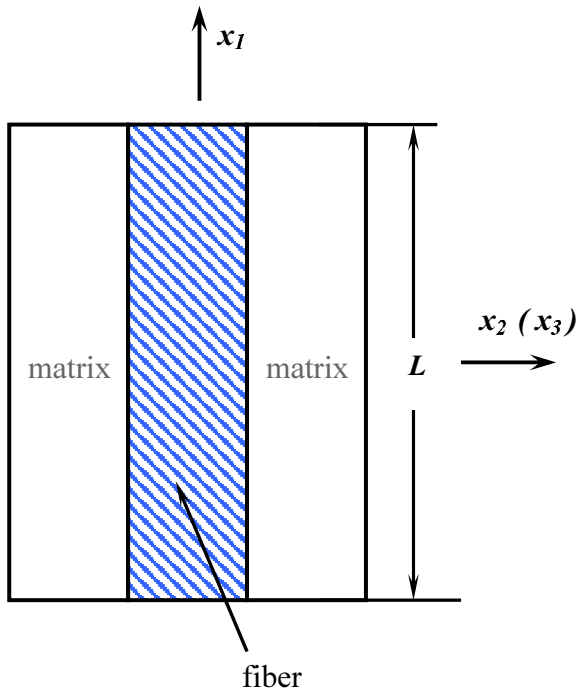

Figure 2.4: A RVE in the rule-of-mixture model.

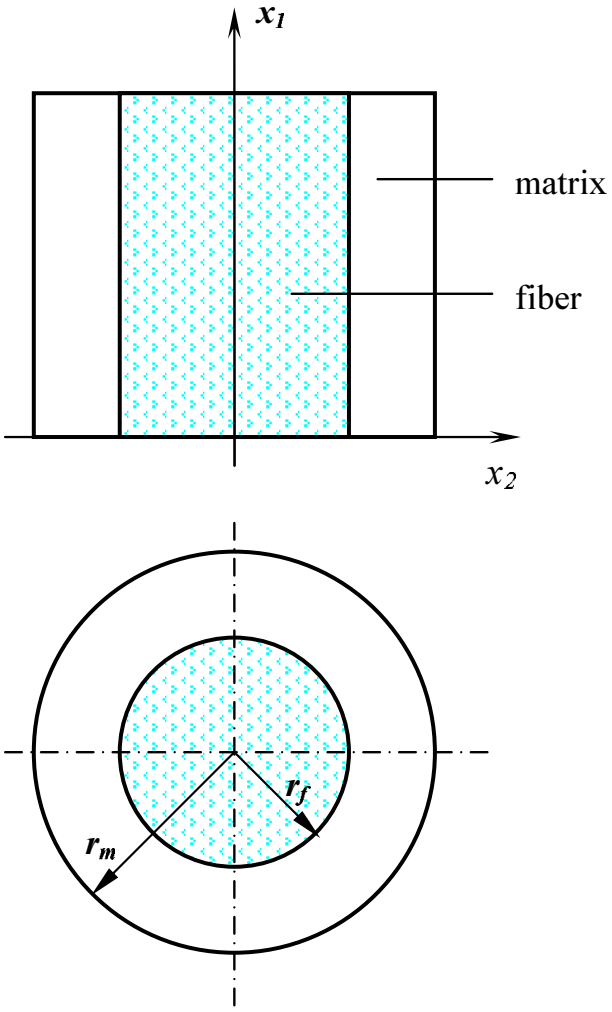

Figure 2.5: Geometry of a composite cylinder in Hashin and Rosen's model [16].

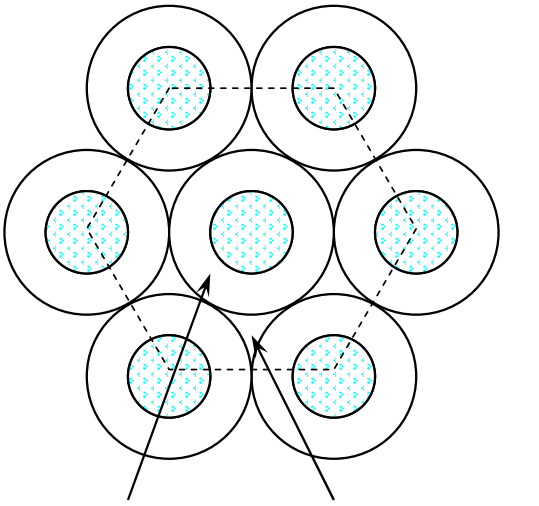

(a)

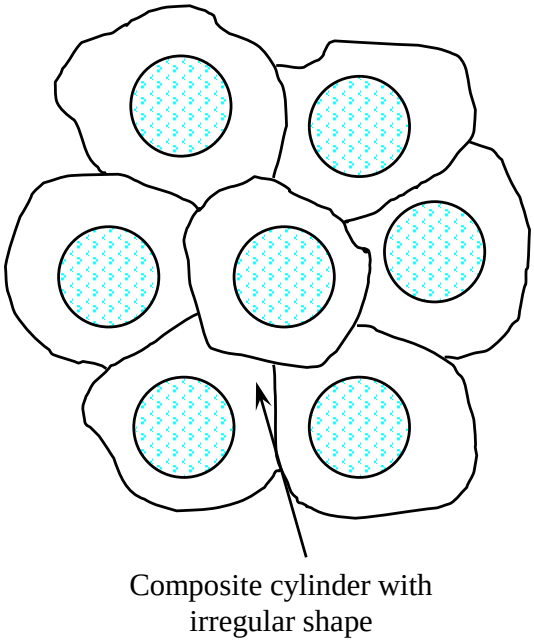

(b)

Figure 2.6: Fiber packing: (a) hexagonal array of composite cylinders, (b) random array of composite cylinders, after Hashin and Rosen [16].

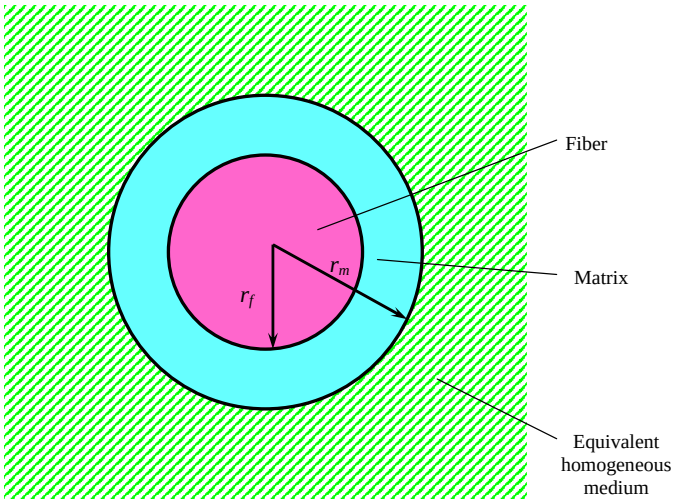

Figure 2.7: A 3-phase RVE model in Generalized Self Consistent Model(GSCM), after Christen and Lo [4].

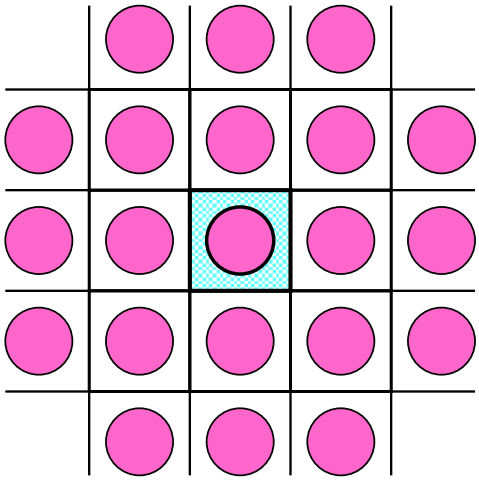

(a) Composite with periodic array.

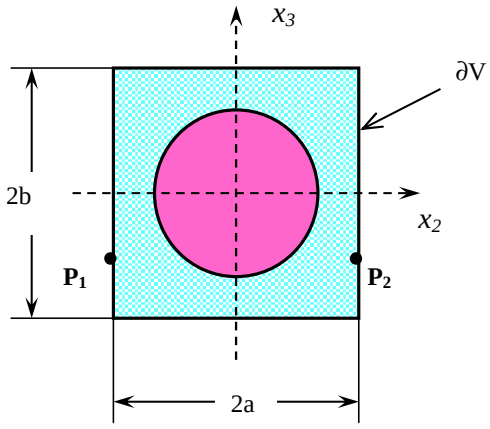

(b) A unit cell.

Figure 2.8: UD composite with regular fiber packing: (a) periodic array (b) unit cell [55].

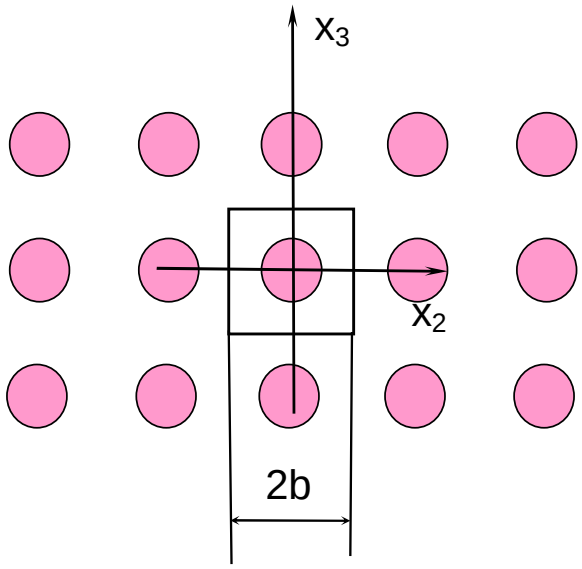

Figure 2.9: A square packing and the square unit cell -after [32].

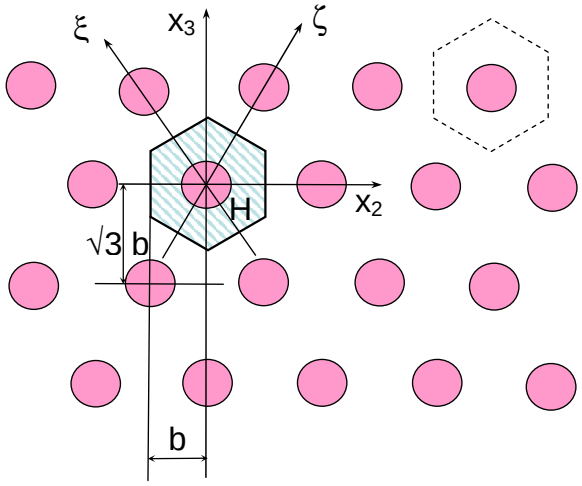

Figure 2.10: A hexagonal packing and the hexagonal unit cell -after [32].

Chapter 3: A Multi-Fiber RVE Model For Homogenization

A multi-fiber RVE model is described in this chapter. The model is developed to obtain the exact micro fields in the RVE, and hence the exact effective moduli for the homogenized composites. Numerical examples are presented to illustrate the details in this modelling approach.

3.1 The Multi-fiber RVE Model

For UD composites having random fiber packing, the RVE must contain sufficient number of fibers in order to be consistent with the statistical homogeneity and material symmetry assumptions. Furthermore, only a multi-fiber RVE can retain the exact effects of fiber-to-fiber interaction. These points are discussed in Chapter 2 (see Section 2.1.1-2.1.3).

Once a proper RVE is selected, exact boundary conditions must be prescribed; so the resulting B-V problems can be solved. However, this is not possible because the exact boundary stresses and displacements are integral parts of the B-V problem solutions in the first place. With the multi-fiber RVE, the bounding method of Hashin and Rosen [16] can still be applied by specifying statically equivalent uniform boundary conditions; approximate RVE micro fields are obtained. Owing to the Saint Venant's principle, the interior of the RVE is insensitive to the details of the boundary conditions, as long as they are statically equivalent. Hence, the micro fields in the interior are exact, or nearly exact.

The details in the model development are given in the following:

According to mechanics principles, uniformly applied far field load would induce the uniform stress and strain in the homogenized composite. In truth, the exact micro stresses and strains on the RVE boundary are not uniform; let them be expressed in the form:

$$\epsilon_{ij} = \epsilon^0_{ij} + \delta\epsilon_{ij} \quad \text{on } \partial V, \tag{3.1}$$

$$\sigma_{ij} = \sigma^0_{ij} + \delta\sigma_{ij} \quad \text{on } \partial V, , \tag{3.2}$$

where V is the volume of the RVE; ∂V is the boundary of the RVE; ϵ^0_{ij} and σ^0_{ij} are the averaged strains and stresses, respectively; $\delta\epsilon_{ij}$ and $\delta\sigma_{ij}$ are perturbations from composite microstructure, including the effect of fiber-to-fiber interactions.

These perturbations are self-equilibrated and don't contribute to the averaged stresses and strains. Specifically,

$$\int_{\partial V} \delta\epsilon_{ij} ds = 0 \tag{3.3}$$

$$\int_{\partial V} \delta\sigma_{ij} ds = 0\,. \tag{3.4}$$

In general, $\delta\epsilon_{ij}$ and $\delta\sigma_{ij}$ are oscillatory on the RVE boundary; the characteristic length of the oscillation is on the order of the fiber diameter d_f.

Owing to the Saint Venant's principle, the effect of $\delta\epsilon_{ij}$ and $\delta\sigma_{ij}$ on the micro fields diminishes beyond a distance larger than the fiber diameter. This fact will be demonstrated numerically in several examples later in this chapter.

Based on the above mentioned Saint Venant's effect, a *center element* inside the RVE

is identified. The boundary of the center element is at least one fiber diameter from the RVE boundary. The stresses and strains on the boundary of the center element are then exact or nearly exact. The micro fields inside the center element are even more so. Figure 3.1 shows a multi-fiber RVE with a center element for a UD system with a random fiber packing.

By applying the averaging procedure over the center element, the computed effective moduli will be unique and exact, regardless whether a set of statically equivalent uniform displacement or traction condition is imposed on the RVE boundary. In fact, the computed upper and lower bounds over the center element simply collapse into one.

In a recent article, Wang and Sun [43] examined the decaying effect of oscillatory boundary conditions (i.e. the Saint Venant's effect) in UD composites with a square array. Oscillating boundary stresses of varying frequencies were prescribed on an RVE containing 25 fibers, as shown in Figure 3.2. The decay rate of the boundary effect was examined as a function of the oscillation wavelength. It is found that, at a distance of one wavelength inside the RVE boundary, the amplitudes of the oscillating stresses reduce to less than 5% of that on the boundary. In UD composites, the oscillatory stresses due to fiber-to-fiber interaction have a wavelength of one fiber diameter or so. Thus, the center element may be selected according to the following guidelines:

1. For composites of a random fiber array, the RVE should be selected in accord with the statistical homogeneity and material symmetry. The center element should be at least one fiber diameter inside the RVE. Generally, the center element may contain one or more than one fiber; the number of fibers depends on the actual fiber packing. See Figure 3.1.

Table 3.1: Constituent thermo-elastic properties of the E-glass/epoxy UD system.

	Young's modulus $E(msi)$	Poison's ratio ν	Thermal Expansion coefficient $\alpha(\times 10^{-6} in/in -^o F)$
E-glass	10.6	0.22	2.8
Epoxy	0.5	0.35	32

2. For "model" composites having a square or rectangular array, a 9-fiber RVE may suffice. In that case, the center element will contain only a single fiber. See Figure 3.3(a).

3. For hexagonal fiber array, an RVE involving 13 or more fibers is needed; the center element contains one fiber or more. See Figure 3.9(a).

3.2 Numerical Examples

The use of the multi-fiber RVE model for homogenization can best be illustrated by specific examples. The composite considered in the examples is a glass/epoxy UD system. The fiber and matrix are assumed linearly elastic; and the fiber/matrix interface are perfectly bonded. Table 3.1 lists the thermo-elastic constants of the E-glass fiber and the epoxy matrix.

Three types of fiber packing are considered, namely: (a) square array, (b) hexagonal array, and (c) random array. However, results for the square array are presented in more details in order to facilitate a comparison with that obtained by the periodic model. Among the effective moduli, the transverse shear modulus G_{23} is singled out for comparison; the reason is that G_{23} is most sensitive to the assumed fiber packing.

3.2.1 Square Array

For composites of a square array, a 9-fiber RVE is selected, see Figure 3.3 (a). In this case, square symmetry is appropriate and 6 independent constants need to be determined. 4 sets of independent boundary conditions need to be applied on the RVE. The corresponding linear displacement and uniform traction boundary conditions, and the effective constants to be computed from each case are listed in Table 3.2. For composites having a rectangular array, 6 sets of independent boundary conditions are specified in order to compute the 9 independent moduli; the corresponding list is found in Appendix A.2.

Numerical computations are carried out by the commercial FEA software ANSYS; quadratic triangular plane strain elements are used; the number of elements within a single fiber element is about $6,000$. Several MATLAB programs are written for processing the stress, strain, and displacement data from the FEA solutions.

For the square array, the periodic model of Yuan, et.al [55] applies; and it provides unique and exact solutions. thus, a concurrent analysis of the examples is also conducted to obtain comparable results. Figure 3.3 (b) shows the single-fiber periodic element in relation to the 9-fiber RVE. The periodic boundary conditions are listed in Table 2.2, by setting $a = b$.

Under the pure shear loading in the $x_2 - x_3$ plane, either in term of uniform traction, or linear displacement, (case #3 in Table 3.2), the micro fields in the 9-fiber RVE are computed for a UD composite with $V_f = 36\%$. The deformed configuration of the center element is shown in Figure 3.4(a). The deformed configuration of the periodic element is shown in Figure 3.4(b). The periodic component of the deformed configuration in

Table 3.2: Uniform boundary conditions and corresponding effective elastic and mathematic constants for a UD composite with a square array.

Elastic and Mathematic constants	Strain B.C.	Displacement B.C.	Stress B.C.	Traction B.C.	FE models
C_{11} C_{12} C_{13} (E_{11}) (ν_{12}) (ν_{13})	$\epsilon_{11} = \epsilon^0_{11}$ $\epsilon_{22} = 0$ $\epsilon_{33} = 0$ $\epsilon_{ij} = 0$ $i \neq j$ $i, j = 1, 2, 3$	$u_1 = \epsilon^0_{11} x_1$ $u_2 = 0$ $u_3 = 0$	$\sigma_{11} = \sigma^0_{11}$ $\sigma_{22} = 0$ $\sigma_{33} = 0$ $\sigma_{ij} = 0$ $i \neq j$ $i, j = 1, 2, 3$	$T_1(x_2, x_3) = \sigma^0_{11}$ $T_2 = 0$ $T_3 = 0$	generalized plain strain
C_{22} C_{23} (E_{22}) (ν_{23})	$\epsilon_{11} = 0$ $\epsilon_{22} = \epsilon^0_{22}$ $\epsilon_{33} = 0$ $\epsilon_{ij} = 0$ $i \neq j,$ $i, j = 1, 2, 3$	$u_1 = 0$ $u_2 = \epsilon^0_{22} x_2$ $u_3 = 0$	$\sigma_{11} = 0$ $\sigma_{22} = \sigma^0_{22}$ $\sigma_{33} = 0$ $\sigma_{ij} = 0$ $i \neq j,$ $i, j = 1, 2, 3$	$T_1 = 0$ $T_2(x^0_2, x_3) = \sigma^0_{22}$ $T_2(-x^0_2, x_3) = -\sigma^0_{22}$ $T_2(x_2, x^0_3) = 0$ $T_2(x_2, -x^0_3) = 0$ $T_3 = 0$	plain strain
C_{44} (G_{23})	$\gamma_{23} = \gamma^0_{23}$ other $\epsilon_{ij} = 0$	$u_2 = \frac{\gamma^0_{23} x_3}{2}$ $u_3 = \frac{\gamma^0_{23} x_2}{2}$ $u_1 = 0$	$\sigma_{23} = \sigma^0_{23}$ other $\sigma_{ij} = 0$	$T_1 = 0$ $T_2(x^0_2, x_3) = 0$ $T_2(-x^0_2, x_3) = 0$ $T_2(x_2, x^0_3) = \sigma^0_{23}$ $T_2(x_2, -x^0_3) = -\sigma^0_{23}$ $T_3(x^0_2, x_3) = \sigma^0_{23}$ $T_3(-x^0_2, x_3) = -\sigma^0_{23}$ $T_3(x_2, x^0_3) = 0$ $T_3(x_2, -x^0_3) = 0$	plain strain
C_{66} (G_{12})	$\gamma_{12} = \gamma^0_{12}$ other $\gamma_{ij} = 0$	$u_1 = \gamma^0_{12} x_1$ $u_2 = 0$ $u_3 = 0$	$\sigma_{12} = \sigma^0_{12}$ other $\sigma_{ij} = 0$	$T_1(x^0_2, x_3) = \sigma^0_{12}$ $T_1(-x^0_2, x_3) = -\sigma^0_{12}$ $T_1(x_2, x^0_3) = 0$ $T_1(x_2, -x^0_3) = 0$ $T_2 = 0$ $T_3 = 0$	generalized plain strain

each case is shown in Figure 3.5 (a) and (b) respectively. No difference can be discerned between the two sets of results.

The micro stress fields in the center element and in the periodic element are also compared. Figure 3.6 shows the radial normal stress distribution along the fiber/matrix interface as a function of θ, $0^o \leq \theta \leq 360^o$. Here again, the results from the 9-fiber RVE model and the periodic model agree well. The large oscillation in the radial stress distribution reflects the fiber-to-fiber interaction.

From the above, it is seen that the micro fields in the center element of the 9-fiber RVE are exact, or nearly exact, compared to the periodic model solution. Consequently, upon averaging, the effective transverse shear modulus G_{23} should be exact as well. Figure 3.7 displays the results of G_{23} as a function of V_f. Here, if G_{23} is computed by averaging over the entire 9-fiber RVE, a pair of bounds is obtained; when the average is taken over the center-element only, the bounds collapse into one. Exact G_{23} solutions for $V_f = 49\%$ and 64% are also obtained using the periodic model; both fall on the curve of the collapsed bounds. Table 3.3 lists the numerical values of G_{23} computed from the various models.

It should be pointed out that more than one type of periodic element can be defined for the square array. A different periodic element is labelled #2 in Figure 3.8. It is oriented 45^o from the one used before (labelled #1) and it contains a whole fiber in the center and 1/4 fiber at each of the 4 corners. The effective moduli in the $x_2 - x_3$ plane computed from this periodic element are different from the element #1 used before; the relations between the effective moduli in the #1 and #2 elements are readily found by a

Table 3.3: Numerical results of G_{23} for Glass/Epoxy composite with a square array

Volume Fraction (%)	G_{23}^{strain} (msi) 9-fiber RVE	G_{23}^{stress} (msi) 9-fiber RVE	G_{23}^{strain} (msi) center element in 9-fiber RVE	G_{23}^{stress} (msi) center element in 9-fiber RVE	G_{23} (msi) Periodic element model
25	0.2699	0.2584	0.261	0.261	
36	0.3132	0.3013	0.3049	0.3041	
42.25	0.3619	0.3326	0.3365	0.3351	
49	0.4145	0.3756	0.3797	0.3773	0.378
56.25	0.4908	0.4389	0.4433	0.4396	
64	0.6148	0.5411	0.5515	0.5455	0.548
72.25	0.87889	0.7494	0.7928	0.7857	

coordinate transformation:

$$E_{22}^{'} = \frac{4E_{22}G_{23}}{E_{22} + 2G_{23}(1-\nu_{23})} \tag{3.5}$$

$$G_{23}^{'} = \frac{E_{22}}{2(1+\nu_{23})} \tag{3.6}$$

$$\nu_{23}^{'} = \frac{E_{22} - 2G_{23}(1-\nu_{23})}{E_{22} + 2G_{23}(1-\nu_{23})}, \tag{3.7}$$

where E_{22}, G_{23}, and ν_{23} are the transverse Young's modulus, in-plane shear modulus, and Poison's ratio obtained from the periodic element #1; $E_{22}^{'}$, $G_{23}^{'}$, and $\nu_{23}^{'}$ are the ones from the periodic element #2.

3.2.2 Hexagonal Array

In the case of the hexagonal array, the selected RVE involves 13 fibers: 5 whole fibers, 4 half fibers, and 4 quarter fibers; the center element contains only a single fiber, see Figure

3.9(a). Here, transverse isotropy is assumed; 5 independent constants are computed from 5 independent sets of boundary conditions. These are listed previously in Table 2.2.2.

For purpose of comparison, the 2-phase single fiber RVE of Hashin and Rosen [16] and the 3-phase self-consistent RVE of Christensen and Lo [4] are also analyzed, see Figure 3.9 (b) and (c), respectively. The periodic model of Li [32] is not used, due to excessive computation time required in the execution.

The 3-phase self-consistent method is executed, using an iterative procedure: namely, the moduli of the equivalent composite are first assumed; the micro field in the RVE is then computed; the effective moduli in the RVE are obtained by an averaging procedure. If the computed RVE moduli and the assumed composite moduli are not the same, the process is then repeated by replacing the assumed composite moduli with the computed RVE moduli. Unique solutions for the composite moduli are obtained when the two sets of moduli agree.

Figure 3.10 depicts 3 sets of G_{23} as a function of V_f. One set is the bounds from the 2-phase single fiber RVE model; another set is computed from the 3-phase self-consistent model; and the 3rd set is the bounds computed from the center-element in the selected RVE. It is seen that the 2-phase single fiber RVE model yields a pair of rather wide bounds; the multi-fiber RVE model yields a pair of rather narrow bounds to the point of collapsing into one. The 3-phase self-consistent model yields a curve slight higher than the pair of narrow bounds. The difference shows the approximate nature of the 3-phase self-consistent RVE representation and the nearly exact nature of the multi-fiber RVE model. Detailed numerical results are listed in Table 3.4.

Table 3.4: Numerical results of G_{23} for Glass/Epoxy composite with a hexagonal array

Volume Fraction (%)	G_{23}^{strain} (msi) Hashin and Rosen model	G_{23}^{stress} (msi) Hashin and Rosen model	$G_{23}^{self-consistent}$ (msi) Self-consistent model	G_{23}^{strain} (msi) center element in 8-fiber RVE	G_{23}^{stress} (msi) center element in 8-fiber RVE
25	0.299	0.256	0.282	0.276	0.279
36	0.388	0.297	0.352	0.338	0.343
42.25	0.454	0.329	0.405	0.3857	0.392
49	0.54	0.374	0.477	0.451	0.459
56.25	0.654	0.44	0.577	0.543	0.5527
64	0.812	0.539	0.7208	0.6799	0.695
72.25	1.043	0.713	0.937	0.896	0.915

Figure 3.11 shows the radial normal stresses σ_{rr} along the fiber and matrix interface, computed from the 3-phase self-consistent model and the multi-fiber RVE model, respectively. Both models retain the oscillatory characteristics in σ_{rr}, reflecting the fiber-to-fiber interaction. But, differences between the two still exist. The multi-fiber RVE model exhibits more micro details than the 3-phase self-consistent model.

3.2.3 Random Array

For composites with random fiber array, such as displayed in Figure 2.1 (a), a 25-fiber RVE is chosen, which conforms to the statistical homogeneity and transverse isotropy assumptions. The center element in the RVE is identified to be one fiber diameter from the RVE boundary. In this case, it contains 9 fibers, as shown in Figure 3.13. For the 5 independent effective moduli, the required RVE boundary loadings are given in Table 2.2.2.

Table 3.5: Numerical results of G_{23} for Glass/Epoxy composite with a random array

Volume Fraction (%)	G_{23}^{strain} (msi) Hashin and Rosen model	G_{23}^{stress} (msi) Hashin and Rosen model	G_{23}^{strain} (msi) 25-fiber RVE	G_{23}^{stress} (msi) 25-fiber RVE	G_{23}^{strain} (msi) center element in 25-fiber RVE	G_{23}^{stress} (msi) center element in 25-fiber RVE
25	0.299	0.256	0.269	0.262	0.263	0.263
36	0.388	0.297	0.321	0.306	0.310	0.309
42.25	0.454	0.329	0.361	0.343	0.348	0.347
49	0.54	0.374	0.411	0.385	0.390	0.389
56.25	0.654	0.44	0.491	0.453	0.455	0.454
64	0.812	0.539	0.599	0.548	0.556	0.554
72.25	1.043	0.713	0.860	0.770	0.801	0.791

Figure 3.14 provides 2 sets of solutions for the transverse shear modulus G_{23}, plotted as a function of V_f. One set is the bounds obtained from the 2-phase single fiber RVE model of Hashin and Rosen; the other is the bounds computed from averaging over the 9-fiber center element in the 25-fiber RVE. It is seen that the bounds from the multi-fiber RVE model are so narrow as to be uniquely valued; the bounds from the 2-phase single fiber RVE are rather wide. Table 3.5 gives detailed numerical results.

Figure 3.15 shows the radial normal stresses σ_{rr} along the fiber and matrix interface for two fibers, arbitrarily chosen inside the center element, see Figure 3.13; fiber 1 is close to its neighboring fibers; fiber 2 is more distant. It is seen that the micro stresses in the 9-fiber center element also displays a degree of randomness; the closer the fibers, the more pronounced the effect of fiber-to-fiber interactions.

3.3 Discussions and Summary

In the literature, most UD composites are modelled by the 2-phase or 3-phase single fiber RVE. Occasionally, the rectangular, square, and hexagonal arrays are also assumed, even though the actual fiber packing is random. Thus, it is interesting to pose the question as to what difference do these fiber packing assumptions make. Figure 3.16 displays the computed G_{23} versus V_f for the square, hexagonal, and random arrays. These are all computed using the properly selected multi-fiber RVE. In each case, a pair of collapsed bounds is obtained. It is seen that, in the reference frame in which the moduli are computed, the square array gives the lowest value for G_{23}, while the hexagonal array gives the highest value; the 25-fiber RVE for the random array yields a value in between. The square array is much closer to the random array representation, at least in the case for G_{23}.

In this chapter, it is demonstrated that the multi-fiber RVE with a center element possesses several advantages over the other prevailing homogenization models:

1. It is capable of modelling UD composites with regular arrays as well as random array;

2. It conforms to the statistical homogeneity and material symmetry assumptions, especially for composites with random fiber packing;

3. Uniform traction and linear displacement boundary conditions can still be imposed on the RVE in the same manner as before;

4. The computed micro stress and strain fields in the center element in the respective RVE are unique and exact, regardless the details of the imposed boundary conditions;

5. Consequently, bounds for the effective moduli collapse into one; these effective moduli are unique and exact.

The multi-fiber RVE model can also be used to recover the micro fields in composites subjected to external loads. In that case, one or more multi-fiber RVEs may be placed in regions of stress concentration; the boundary conditions on the RVE are rendered from the macro analysis of the composite under load; and the micro fields in the RVE (i.e. the center element) can the be obtained exactly or near exactly by solving the B-V problem so defined for the RVE. Details in the recovery process will be discussed in Chapter 4.

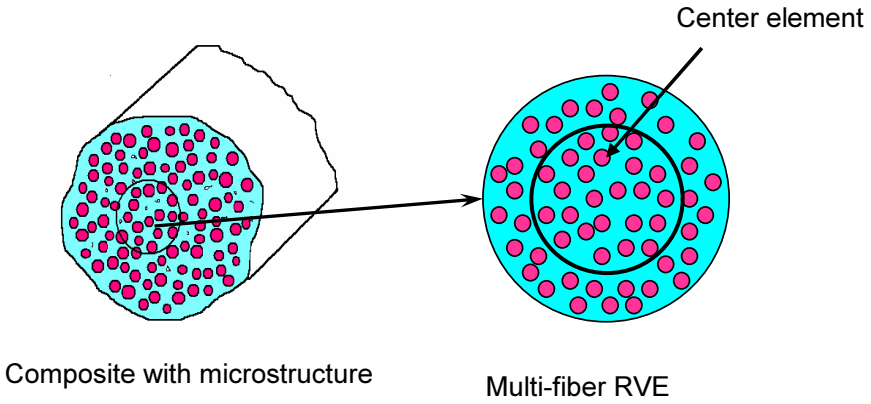

Figure 3.1: a Schematic of Multi-fiber RVE.

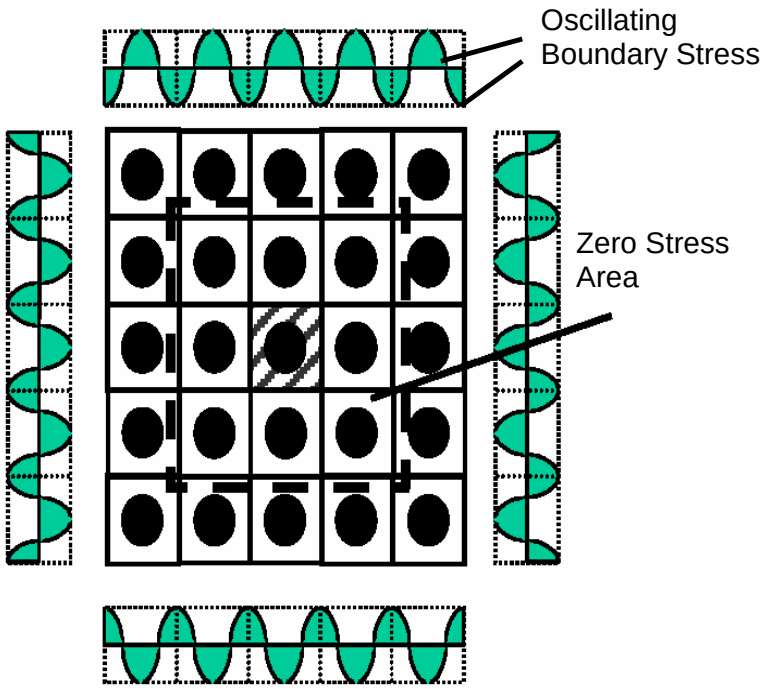

Figure 3.2: Oscillating boundary stress: micro boundary and effective boundary - after [43] .

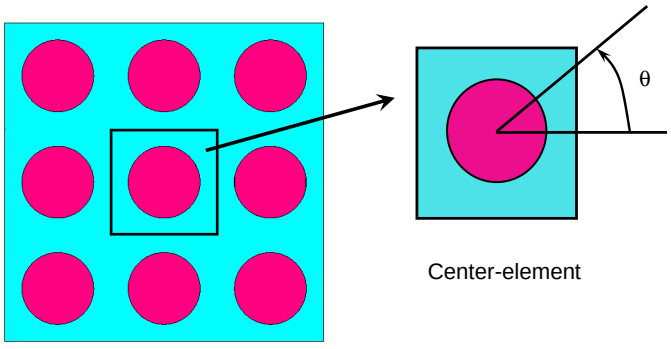

(a)

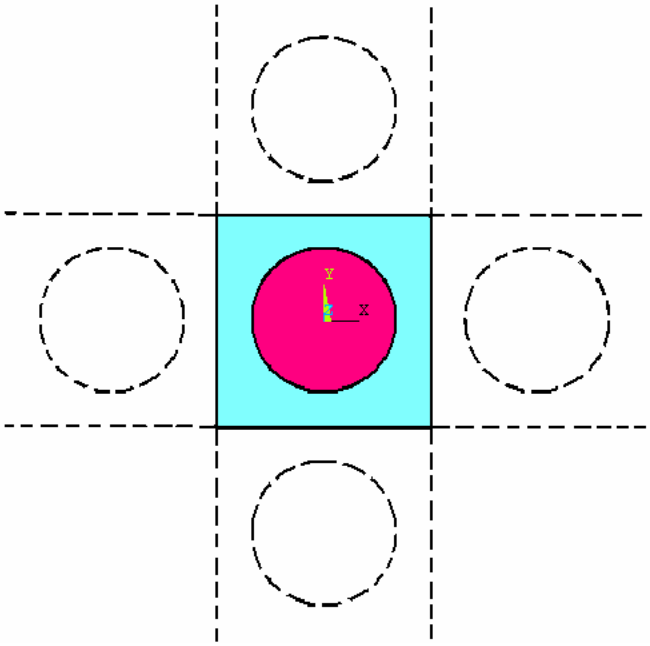

(b)

Figure 3.3: RVEs for square array (a)a 9-fiber RVE with center element (b) a periodic element.

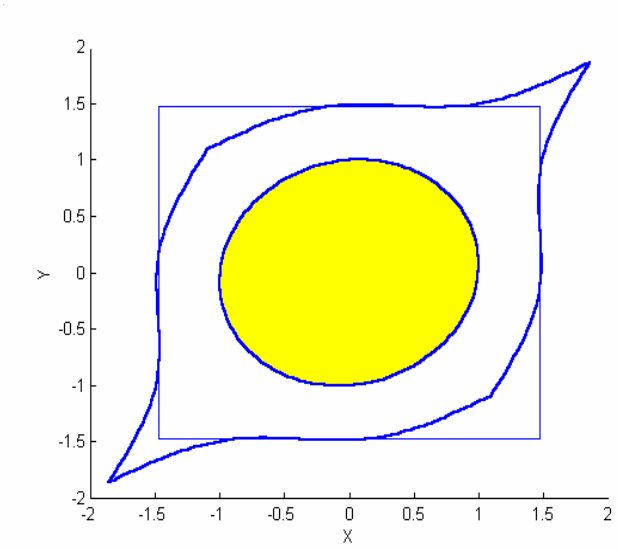

(a)

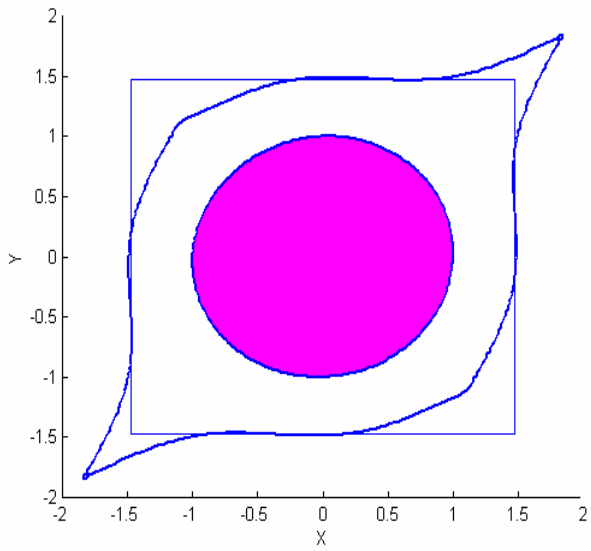

(b)

Figure 3.4: Deformed shape: (a) center element in the 9-fiber RVE (b) periodic element, glass/epoxy composite with square array under uniform shear

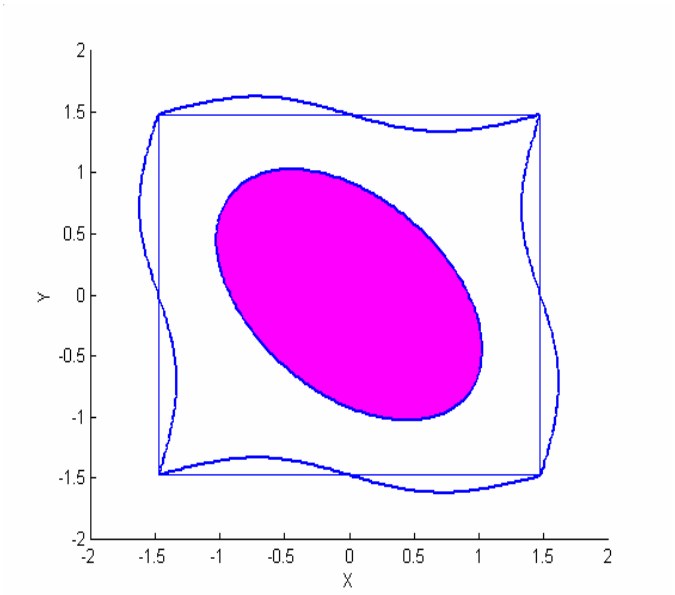

(a)

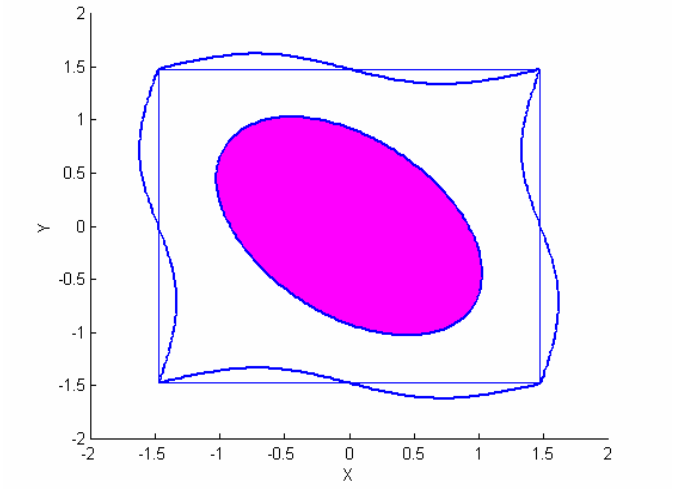

(b)

Figure 3.5: Periodic component in the deformation of glass/epoxy composite with square array under uniform shear (a) center element in the 9-fiber RVE (b) periodic element.

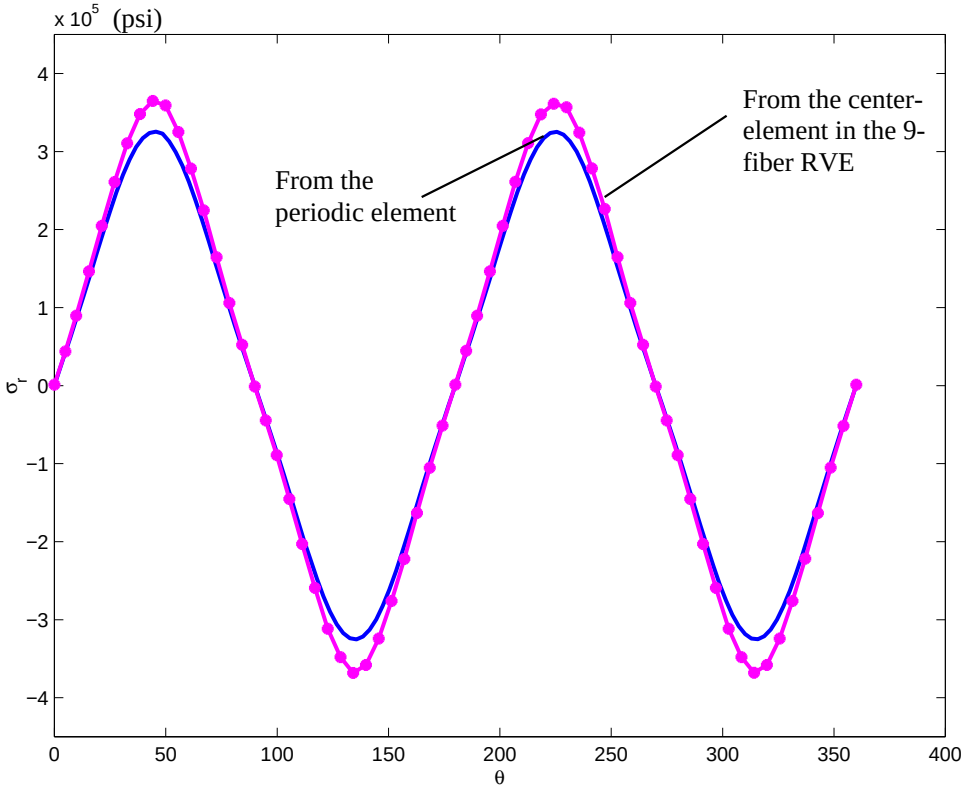

Figure 3.6: σ_{rr} along the fiber/matrix interface from the center element in the 9-fiber RVE and the periodic element

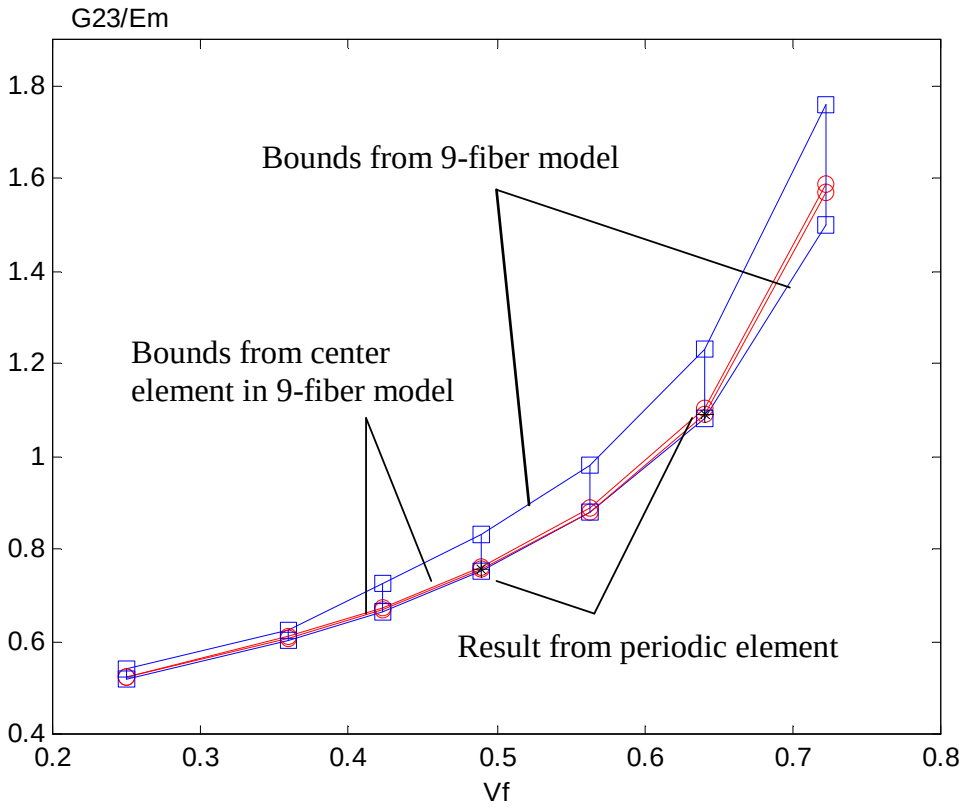

Figure 3.7: G_{23} vs. V_f for glass/epoxy composites with square array

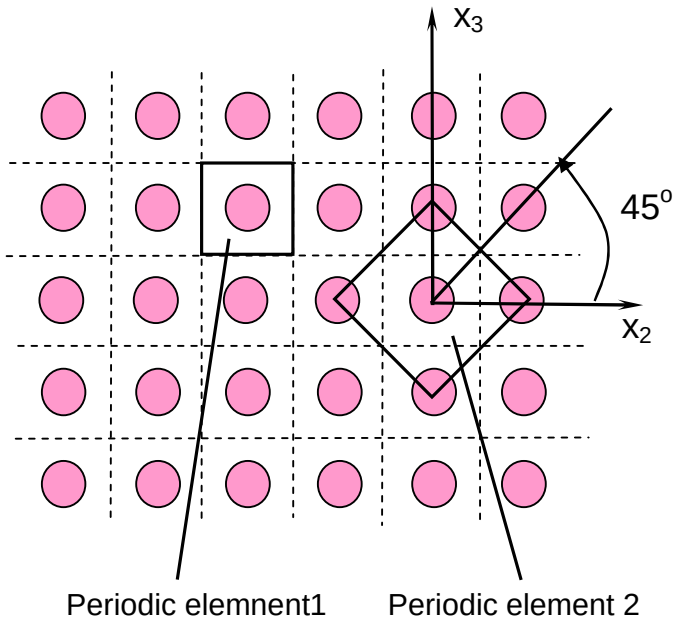

Figure 3.8: Possible periodic elements for square array

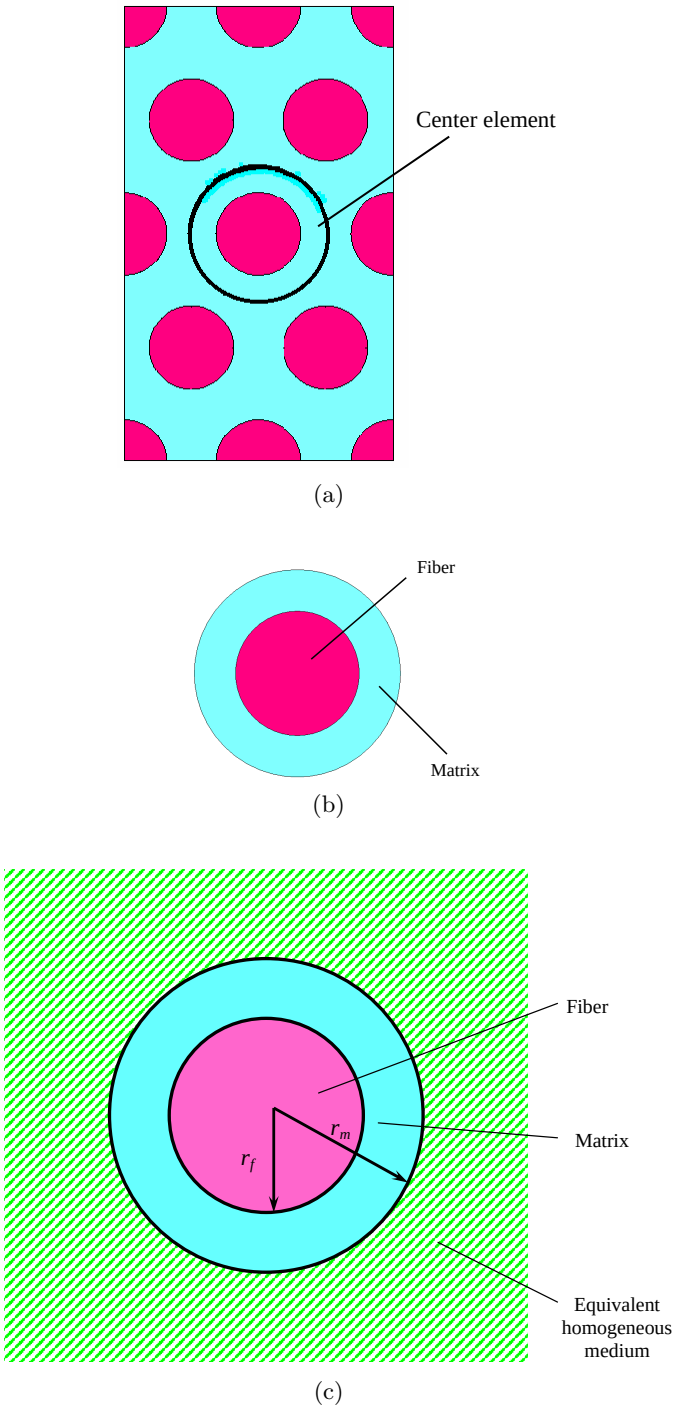

Figure 3.9: Three RVEs used for composite with hexagonal array: (a) a multi-fiber RVE with a center-element, (b) 2-phase single fiber RVE, (c) 3-phase single fiber RVE.

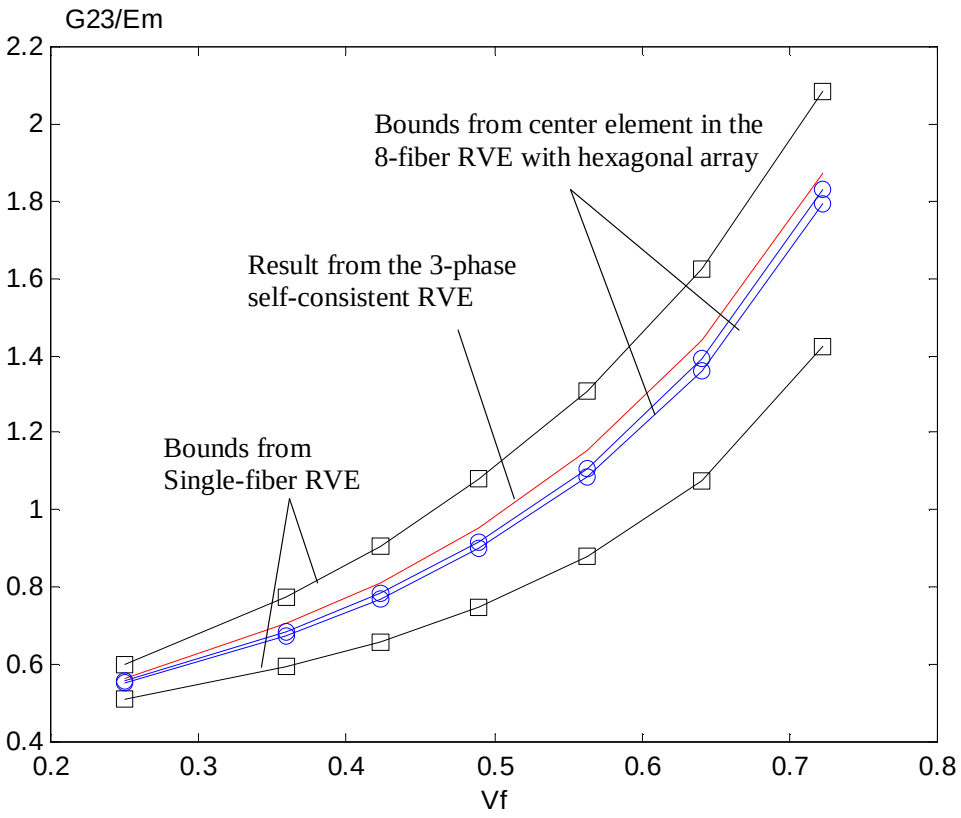

Figure 3.10: G_{23} vs. V_f for glass/epoxy composites with hexagonal array

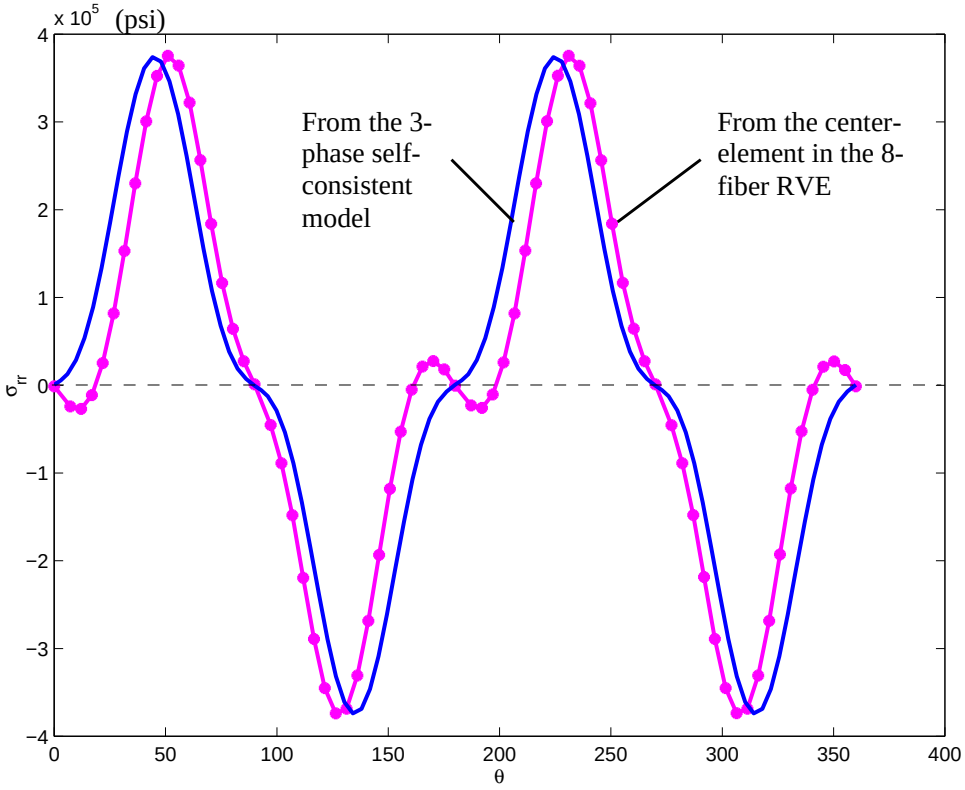

Figure 3.11: σ_{rr} along the fiber/matrix interface from the center element in the 8-fiber RVE model and the 3-phase Self-Consistent Model

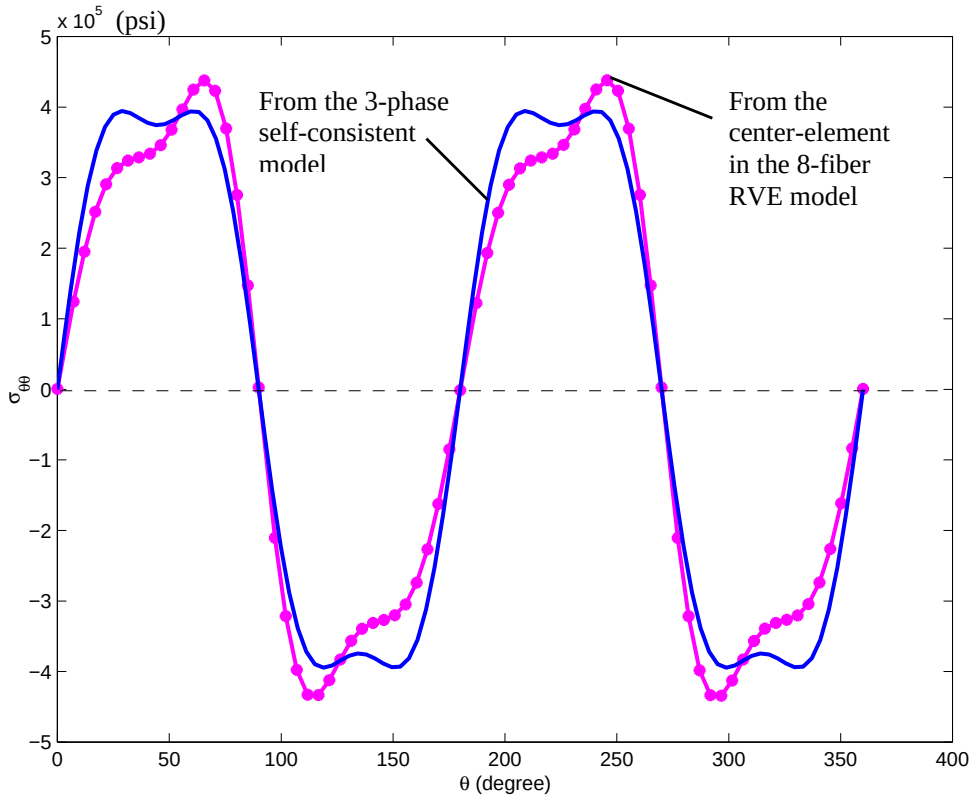

Figure 3.12: σ_{xy} along the fiber/matrix interface from the center element in the 8-fiber RVE model and the 3-phase Self-Consistent Model

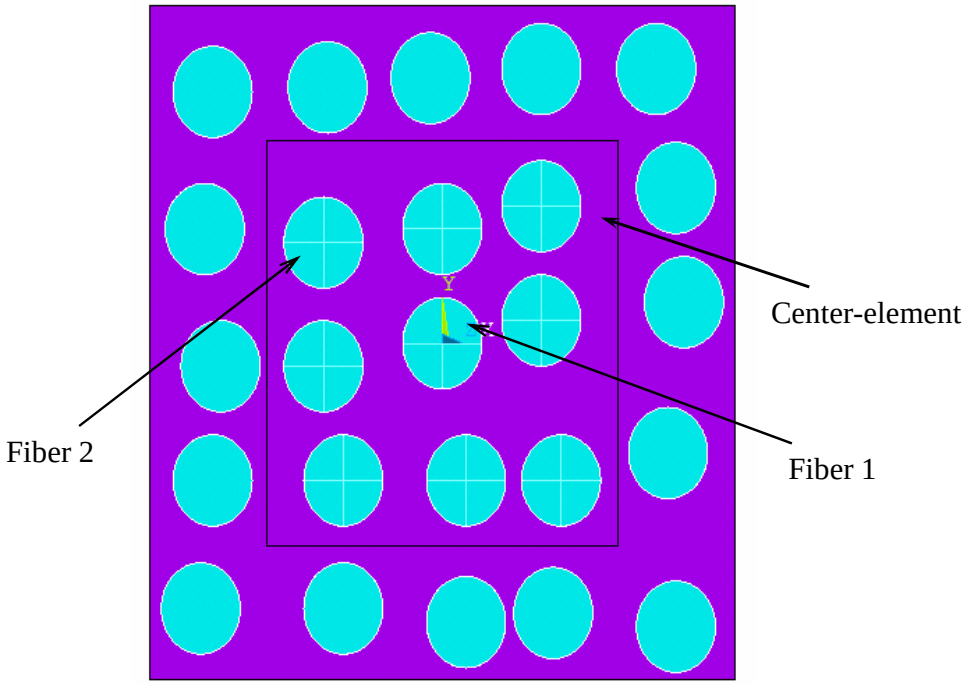

Figure 3.13: A 25-fiber RVE with a center-element containing 9 fibers for random array

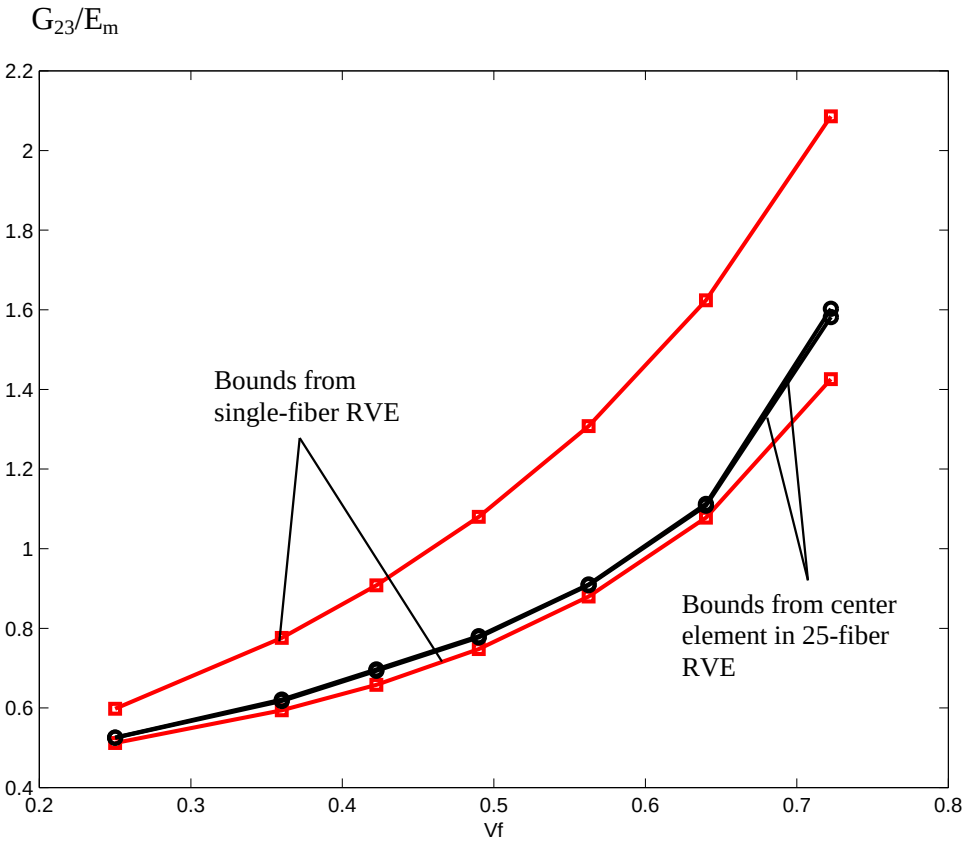

Figure 3.14: G_{23} vs. V_f for glass/epoxy composites with random array

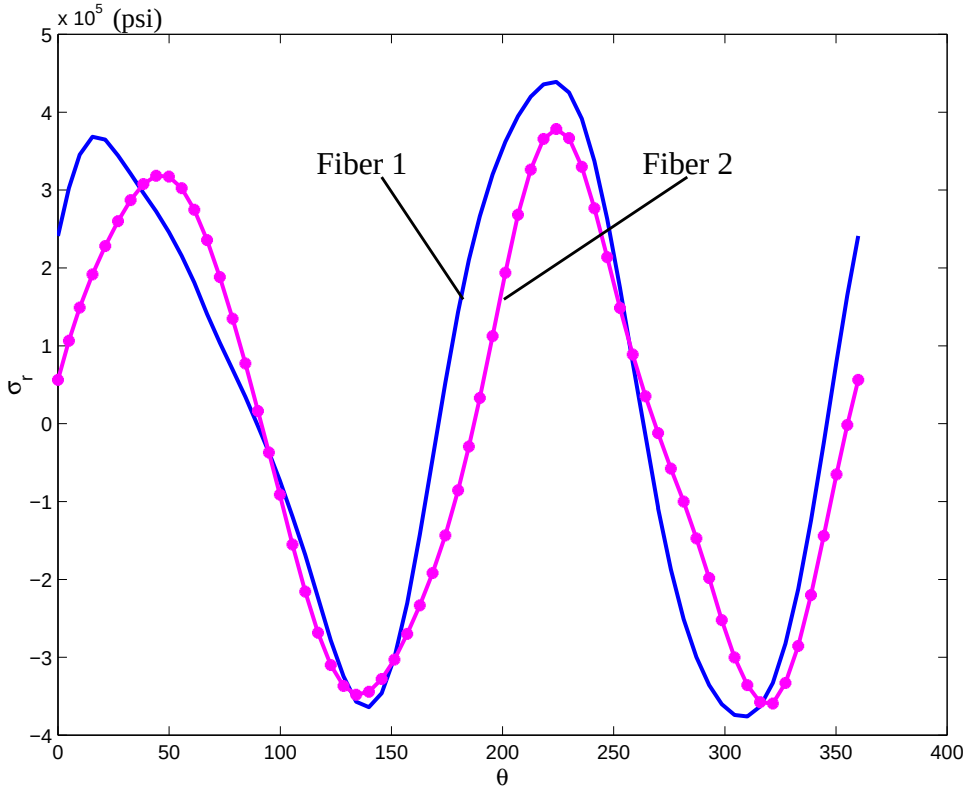

Figure 3.15: σ_{rr} along the fiber/matrix interface for different fibers in the center element

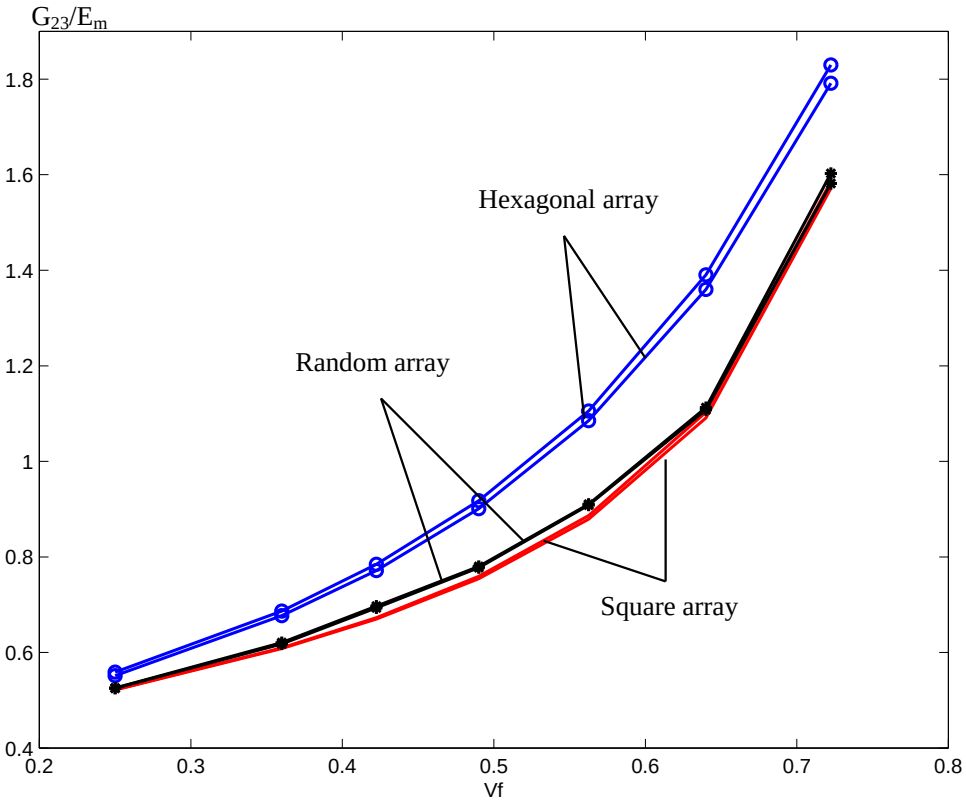

Figure 3.16: G_{23} vs. V_f, a comparison among results for composites with square array, hexagonal array, and random array

Chapter 4: De-Homogenization: To Recover The Micro Fields

This chapter is devoted to the subject of De-Homogenization. De-homogenization is also a mechanics formulation for the recovery of the micro fields, following the homogenization of the basic composite systems and the analysis of loaded composite structures. The scheme utilizes the multi-fiber RVE modelling concept, and it retrieves the micro fields in suspected failure regions. Numerical examples using the same E-glass/Epoxy UD system as before are presented; major micro field effects, not found in the macro fields of the homogenized composites, are illustrated and examined as to their effects on failure.

4.1 Recent Works Related to De-Homogenization

The recovery of composite micro fields from the homogenized macro fields can be achieved in several ways. All require the restoration of the fiber-level microstructure, at the least, in regions of suspected failure. The recovered micro fields may provide the needed details for a rational description of material failure initiations first in the microstructure and then growth into higher scales.

One obvious, but impractical, way is not to homogenize the fibrous system in the first place; so a load-bearing composite structure is treated with all of its microstructure details at the fiber-matrix scale. In practice, this approach has been abandoned at the outset and homogenization of the fibrous system remains the only viable choice.

In 2000, Fish and Shek [10] attempted to link the micro field mechanics formulation

at the fiber-matrix level to the macro field formulation at the ply level through an inter-scale operator. The micro field is formulated based on a spatially periodic microstructure such as the UD system with a rectangular or square array. A periodic single-fiber unit cell can then be described and analyzed rigorously. The macro field is formulated for specimens containing unlimited numbers of the periodic unit cells; the inter-scale operator connects the two sets of field equations, solvable simultaneously. Theoretically, the micro and macro fields could be obtained in one complex solution scheme; but the approach is applicable only to macro fields of infinite extension; neither geometrical nor material discontinuities at the macro scale are allowed, since the unit cells near such discontinuities would lose periodicity. Yet, material failures usually occur near such discontinuities, e.g. crack-tip, free boundary, lamination interface and regions of stress concentration.

In a subsequent paper, Hutapea, Yuan, and Pagano [26] amended the Fish-Shek formulation by modifying the unit cell that loses periodicity (e.g. near the free surface in the macro field); a couple stress is added in the unit cell field formulation in accordance with the well known micro-polar theory, see e.g. Eringen [9]. In this way, macro fields of finite size and/or containing high stress gradients could be treated.

Recently, an approach similar to that of Fish and Shek was formulated by Raghavan, Moorthy, Ghosh, and Pagano [40]. Instead of a periodic unit cell, a so-called "Voronoi cell" is introduced based on the composite microstructure. The Voronoi cell is similar to the multi-fiber RVE discussed in Chapter 3; it contains multiple fibers packed regularly or randomly. The macro field may contain any number of the Voronoi cells connected through shared finite element nodes. The macro field has definitive boundaries that can be loaded or constrained, and the connected cells deform together in accordance with

their connective conditions; the latter serves as the linkage between the micro fields in the Voronois and the macro fields in the loaded specimen containing the Voronois. Again, the formulated field equations must be solved simultaneously for the micro fields (Voronois) as well as the macro field (specimen). The approach, however, is theoretically sound but difficult to implement computationally.

4.2 De-homogenization Using the Multi-fiber RVE model

As discussed in detail in Chapter 3, the multi-fiber RVE model can be routinely used in the homogenization of UD system and yields unique and exact effective moduli without bounding them. Moreover, the RVE conforms to the underlying statistical homogeneity and symmetry assumptions; it can hence encompass regularly or randomly packed fiber arrays. Now, the same model is applied to recover the micro fields in regions of high stress gradient, after the corresponding macro field solutions are obtained. Uniqueness and accuracy of the recovered micro fields are numerically demonstrated.

The general procedures in the recovery process are as follows:

Consider the schematic shown in Figure 4.1. On the left is the UD composite with a definitive fiber array; homogenization of the composite is carried out by means of a proper multi-fiber RVE, as shown in the middle, which provides the effective moduli for the homogenized composite, as shown on the right. Upon field analysis of the composite under load, a region of interest is identified, as shown by the dash-lined area on the right. This region is then isolated as a free-body, with boundary stresses and displacements drawn from the macro field solutions.

To recover the micro-field of the selected region, the detailed microstructure at the

fiber-matrix level is restored back into the selected region. Then, two boundary-value problems are solved for the region: one with the macro field stresses imposed on the boundary and the other with the macro displacements on the boundary. These boundary agencies are statically equivalent at the macro scale, and they render different micro fields. However, the respective micro-fields in regions a distance away from the boundary (i.e. inside the center element), are identical or nearly identical. Justification of this proposition has been discussed fully in detail in Chapter 3.

The above procedures are generally applied in selected regions where concentration of stress is present; a cautionary note is in order:

Recall that, in the homogenization process, the RVE is subjected to uniform boundary conditions; it is not suitable for RVE subjected to high stress gradient on the boundary. Rapid changes of the stress states could compromise the procedure of volume averaging from which the effective moduli are derived. However, high stress gradient usually decays rapidly from the stress riser, such as at the crack-tip. The multi-fiber RVE modelling concept can still be applied when the following guidelines are observed:

1. The boundary of the selected region of interest must be sufficiently away from the high stress gradient zone, and the macro stresses on the region's boundary can vary only mildly.

2. The center element in which the micro fields remain exact must be placed well within the region's boundary.

These guidelines are independently suggested recently by Wang, Sun, Sun, and Pagano [53], who studied the macro stress gradient effects on the micro fields. Figures 4.2 (a)-(c) show a multi-fiber RVE containing 64 fibers; it is subjected to uniformly, linearly, and

Table 4.1: Effective thermo-elastic properties of E-glass/Epoxy composite with $V_f = 50\%$.

E_{11} (msi)	E_{22} (msi)	G_{12} (msi)	G_{23} (msi)	ν_{12}	ν_{23}	α_{11} $(\times 10^{-6} in/in \cdot^o F)$	$\alpha_{22} = \alpha_{33}$ $(\times 10^{-6} in/in \cdot^o F)$
5.539	1.594	0.487	0.378	0.278	0.378	4.314	19.802

quadratically distributed stresses, but with same average value, on the boundary. Wang, et.al. showed that a properly selected center element should be one fiber diameter away from the boundary for the uniform, and the linear cases; a distance of 2 fiber diameters is needed in the quadratic case.

4.3 Examples of Recovered Micro Fields

A number of interaction effects in the micro field, which is recovered from its corresponding macro-field, are highlighted here with numerical examples. The ABAQUS finite element package is utilized in all computations. The same E-glass/epoxy UD system having a square array and 50% fiber-volume content is used as the base-line material. UD systems are cured at temperatures different from the design operating temperatture; the thermal stresses induced therein also need to be considered. Hence, the thermo-elastic properties of the E-glass fiber and the epoxy matrix are given in Table 3.1. The effective thermo-elastic constants for the UD system are obtained by means of the multi-fiber RVE model, as explained in Chapter 3. The values of the six independent effective constants along with the thermal expansion coefficients in the principle material coordinates are listed in Table 4.1. It is noted that these values are the same as those obtained by the periodic (square) array model [55].

4.3.1 Intra-Microstructure Effects

In the fiber-matrix level, fibers are inclusions in the expanse of matrix material; mismatch in the thermo-mechanical properties can produce significant fiber/matrix and fiber-to-fiber interactions. These are briefly discussed as follows.

Thermal Residual Fields

Consider the free-standing UD specimen. The thermal residual stress field at the fiber-matrix scale due to cooling from the curing temperature can be significant and complex, while the thermal residual stresses at the macro scale are null. For the E-glass/epoxy UD system, the radial normal stress σ_{rr}^{T} acting on the fiber-matrix interface varies in a sinuous pattern around the fiber, as shown in Figure 4.3. In this case, σ_{rr}^{T} is compressive with the maximum magnitude at $14.5psi$ per $\Delta T = -1^{o}F$. Figure 4.4 displays the normal stress σ_{x}^{T} along the side of a unit square containing a single fiber. Here, σ_{x}^{T} varies in a sinuous pattern between the maximum compressive magnitude of $13.5psi$ per $\Delta T = -1^{o}F$ and the maximum tensile magnitude of $8.2psi$ per $\Delta T = -1^{o}F$. Say, ΔT due to cooling from curing to the ambient is $-250^{o}F$; then, the thermal residual stresses in the free-standing UD system can be fairly significant before any other external loading is applied.

Fiber-to-fiber Interactions

Consider the UD composite specimen subjected to a far-field tensile stress σ_0 transverse to the fibers. The macro-field is uniformly stressed with $\sigma_x = \sigma_0$. But, the micro-scale is disturbed by fiber-to-fiber interactions. Figure 4.5 shows the distribution of the micro field σ_x along a unit square containing a single fiber. In this case, the maximum tensile stress in the matrix between two adjacent fibers is $1.714\sigma_0$; the local concentration

Table 4.2: Elastic properties of E-glass, SiC fiber, boron fiber and Epoxy, after [2],[35].

Constituents	E-glass	SiC	Boron	Epoxy
Young's modulus $E(msi)$	10.6	47.1	60	0.5
Poison's ratio ν	0.22	0.15	0.2	0.35
E_f/E_m	21.2	94.2	120	N/A

factor due to fiber-to-fiber interaction, $k = 1.714$. Let this value of k $(= 1.714)$ be the base-line value to which other stress concentration factors are compared in later examples.

Local stress concentration effect due to fiber-to-fiber interaction is widely known [8]. Their intrinsic and extrinsic effects can be assessed only when the micro-field is recovered. As examples, consider the SiC/epoxy and boron/epoxy systems along with the E-glass/epoxy system. Here, the fiber-matrix property mismatch, expressed in terms of E_f/E_m, in each system is listed in Table 4.2. Note that the E_f/E_m value for the E-glass/epoxy system is 21.2, that for the SiC/epoxy system is 94.2, and that for the boron/epoxy system is 120. The k factor are computed for the systems with $V_f = 50\%$ and 64% respectively, and the computed values in each case are listed in Table 4.3. It is seen that the value of k increases with the ratio of E_f/E_m as well as with V_f.

The above demonstrates that the recovered micro fields contain features of stress concentration not found in the macro fields. These features may provide additional clues as to how matrix-dominated failure is initiated at the micro-scale.

4.3.2 Effects from Macro-Scale Constraints

In multi-layer laminates, there exist interactions amongst the laminating plies. These in turn compound the interaction effects at fiber-matrix scale.

Table 4.3: The influence of V_f and mismatch between fiber and matrix on the local stress concentrator factor k.

	E-glass/Epoxy	SiC/Epoxy	Boron/Epoxy
$V_f = 50\%$	$k = 1.714$	$k = 2.000$	$k = 2.735$
$V_f = 64\%$	$k = 1.794$	$k = 2.147$	N/A

As an example, consider the [0/90/0] laminate loaded by the axial tensile strain ϵ_0 , as shown schematically in Figure 4.6.

Here, the macro fields in the layers of the laminate can be rigorously computed, e.g. by the elasticity method [49]; the micro fields in each of the layers can be recovered, using the multi-fiber RVE model. From the recovered micro fields, the effect of the 0^o-layer upon the micro field in the 90^o-layer can be examined. The following two laminate combinations are studied as examples: (1) the 0^o and 90^o layers are both the E-glass/epoxy UD system, with $E_{0^o}/E_{90^o} = 3.4$; (2) the 0^o-layer is the SiC/epoxy system and the 90^o-layer is the E-glass/epoxy system, with $E_{0^o}/E_{90^o} = 14.7$. In addition, the 90^o-layer thickness t_{90^o} varies from $8a_0$, $12a_0$, $20a_0$, and $\geq 50a_0$, a_0 being the size of the unit square containing a single fiber. The thickness of the 0^o layer, $t_{0^o} = t_{90^o}$ (see the inset in Figure 4.6).

The micro field stress concentration factor k in the 90^o-layers are listed in Table 4.4. It is seen that the 0^o-layer has some constraining effects on the 90^o-layer micro fields. Specifically, if the 90^o-layer thickness is kept constant, a stiffer 0^o-layer will reduced the k factor, displaying a degree of the constraining effect. On the other hand, if the 0^o-layer is kept unchanged, a thicker 90^o-layer will increase the k factor. The constraining effect fades with the increased distance from the 0^o-layer. Note that when the 90^o-layer thickness is $50a_0$ or more, k approaches the base-line value of 1.714.

Table 4.4: Effect of macro scale parameters on the computed local stress concentrator factor k .

n	$E_{0^o}/E_{90^o} = 3.4$ (the 0^o-layer: E-glass/epoxy) (the 90^o-layer: E-glass/epoxy)	$E_{0^o}/E_{90^o} = 14.7$ (the 0^o-layer:SiC/epoxy) (the 90^o-layer: E-glass/epoxy)
$n = 4$	$k = 1.671$	N/A
$n = 8$	$k = 1.681$	$k = 1.680$
$n = 12$	$k = 1.688$	$k = 1.685$
$n = 20$	$k = 1.697$	$k = 1.690$
$n \geq 50$	$k = 1.714$	$k = 1.714$

Though the numerical values of the computed stress concentration factor k do not vary significantly, the question of whether such a minor effect could be ignored is not clear at this point. The examples in the next section may provide additional insight into this question.

4.3.3 Effects of Crack-like Defects

Consider the same [0/90/0] laminate loaded by the far-field axial tension ϵ_0 as before. Now, let there be a crack-like defect of size a_{crack}, which is situated in the center of the 90^o-layer thickness and normal to the applied tension, as shown in Figure 4.7.

The micro field in the 90^o-layer is now influenced simultaneously by the 0^o-layer constraint, the 90^o-layer thickness, and the crack-like defect. In this case, the tensile stress along the crack-line from the crack-tip to the 90/0 layer-interface, shown in the inset of Figure 4.7, will be examined.

Numerical analysis of this problem is first conducted at the macro-scale; the crack-like defect is introduced in the homogenized 90^o-layer at the designated location; the laminate

macro fields under the applied load are computed by a 3-D, elasticity-based finite-element routine. The region of interest is identified as that near the crack-tip and a suitable multi-fiber RVE is selected. The center-element in the RVE contains the crack-tip, the fiber pairs along the crack line extend to the 90/0 interface and beyond, see Figure 4.8.

To illustrate the 0^o-layer constraining effect on the crack-like defect, 4 laminate combinations with varying the 90^o-layer thickness t_{90^o} and the stiffness ratio, E_{0^o}/E_{90^o}, are studied: (a) the 90^o-layer thickness, $t_{90^o} = 12a_0$ and $E_{0^o}/E_{90^o} = 3.4$ (i.e. both the 0^o-layer and the 90^o-layer are E-galss/Epoxy system) ; (b) $t_{90^o} = 12a_0$ and $E_{0^o}/E_{90^o} = 14.7$ (i.e. the 0^o-layer is SiC/Epoxy system and the 90^o-layer is E-galss/Epoxy system); (c) $t_{90^o} = 20a_0$ and $E_L/E_T = 3.4$; and (d) $t_{90^o} = 20a_0$ and $E_{0^o}/E_{90^o} = 14.7$. In all cases, the thickness of the 0^o-layer is fixed at $t_{0^o} = 20a_0$; and the size of crack-like defect is also fixed at $a_{crack} = 6a_0$.

Figure 4.9 (a) displays the distribution of the tensile stress along the crack-line for case (a), where $t_{90^o} = 12a_0$ and $E_{0^o}/E_{90^o} = 3.4$. The macro stress is plotted in dotted line, while the corresponding micro stress is plotted in solid line. It is seen that the macro stress is singular near the crack-tip as expected; it decays rapidly away from the crack-tip to approach the far-field stress value of $\sigma_0 = \epsilon_0 E_T$. The micro field stress is oscillating about the macro stress curve along the crack line; the zone of the singular stress is much smaller, however. In this example, there are only three fiber pairs from the crack-tip to the 90/0 interface; the stress concentration factor k for the first pair is as high as 3.47; for the second pair, it reduces to 2.06; for the third one, it is only 1.87. The last value is still higher than the base-line value of 1.714.

Figure 4.9 (b) displays the distribution of the tensile stress along the crack-line for case

(b), where $t_{90^o} = 12a_0$ and $E_{0^o}/E_{90^o} = 14.7$. In this case, the outside 0^o-layer is stiffer than in case (a); the stress concentration at the crack-tip is suppressed; the corresponding k values are 3.38, 2.00, and 1.80, respectively, as compared to 3.47, 2.06, and 1.87 in the previous example.

When the 90^o-layer thickness is increased, say $t_{90^o} = 20a_0$, the k factors in the fiber pairs along the crack line are also increased. This is shown in Figures 4.9 (c) and (d) for the laminate in case (c) and case (d), respectively. In both cases, the distance from the crack-tip to the 0^o-layer is increased to $7a_0$; so the 0^o-layer constraining effect on the crack-tip is reduced, resulting in the increase of the stress concentration factor k along the crack line. These constraining effects may be important in initiating the propagation of the crack-like defect.

4.3.4 Thermal Residual Stresses in Cross-ply Laminates

Composites are fabricated at an elevated temperature. Thermal residual stresses are induced when cooled to the ambient temperature. In some cases, thermal residual stresses alone can cause damage in the form of micro cracking.

In multi-layer laminates, the thermal residual micro field includes contributions from elements at the fiber-matrix level as well as at the laminate level. At the fiber-matrix level, the field is generated by the fiber-matrix property mismatch, as discussed in the examples in Section 4.3.1. In general, the micro field is self-equilibrated (see e.g. Figure 4.4); so at the macro scale, the field becomes null after the composite is homogenized. At the laminate level, the thermal residual stresses occur as a result of ply-to-ply property mismatch. Such fields exists in each of the plies, at the homogenized macro scale. These

two sources of thermal effects mutually interact as well.

As an example, consider the E-glass/epoxy [0/90/0] laminate subjected to a temperature drop $\Delta T = -1^o F$. Here, the thermal residual micro field in the 90^o-layer will be recovered and examined.

To recover this micro field, the first step is to compute the macro fields in the homogenized plies via the $3D$ finite element solution routine. A multi-fiber RVE is then selected, as shown in Figure 4.10, where the center element contains the region from the 90^o-layer mid-plane to the 90/0 interface and beyond. The boundary conditions on the RVE are drawn from the macro scale solution; a temperature drop $\Delta T = -1^o F$ is imposed.

Two laminates with the 90^o-layer thicknesses $t_{90^o} = 10a_0$ and $t_{90^o} = 40a_0$ are considered; the 0^o-layer thickness in both is kept at $t_{0^o} = 20a_0$.

Figure 4.11 (a) depicts the thermal stress σ_x^T across the 90^o-layer thickness for the case of $t_{90^o} = 10a_0$. The thermal stress computed from the macro analysis is plotted in dotted line, while the recovered micro thermal stress is plotted in solid line. The macro field σ_x^T is tensile and nearly uniform throughout the 90^o-ply; its value is $22psi$ per $\Delta T = -1^o F$. The micro σ_x^T is oscillating around the macro σ_x^T; the maximum magnitude of the micro σ_x^T is about $25psi$ per $\Delta T = -1^o F$. It is noted that the oscillation consists of the contributions from the effects of the fiber-to-fiber interactions and the fiber-matrix property mismatch. These two effects are off-phased, as it can also be seen in Figures 4.4 and 4.5.

Figure 4.11 (b) shows the thermal stress σ_x^T along the 90^o-layer thickness for the case of $t_{90^o} = 40a_0$. Again, the macro stress is plotted in dotted line, and the micro stress in solid line. The macro stress displays the similar pattern; but the macro stress is about

$15psi$ per $\Delta T = -1^oF$, while the micro stress exhibits a more complex oscillating pattern.

The oscillating pattern is caused by the combination of the two contributing sources as mentioned above; they are off-phased and cause a complex distributional pattern.

4.4 Summary and Discussions

In summary, the multi-fiber RVE model is a versatile vehicle for de-homogenization, as it is for homogenization. The model provides consistent and reliable results both in the forward and in the reverse processes. When used in the reverse process, microstructural effects can be recovered uniquely and accurately. These effects include the fiber-to-fiber interaction, thermal residual field, interactions with global loading and laminate scale constraints.

The question remains, however, as how to use the micro field solutions to investigate the modes, mechanisms and material conditions governing composite failures. In the next chapter, an attempt is made to model matrix tensile failures in laminates, based on the recovered micro field solutions.

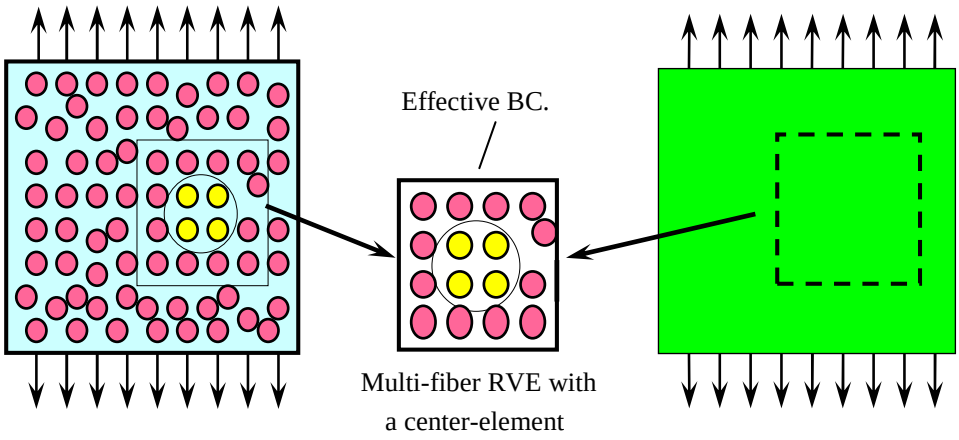

Figure 4.1: A schematic of De-homogenization: Composite body with microstructure (left); The corresponding homogenized body (right); The modified multi-fiber RVE with a center-element (middle)

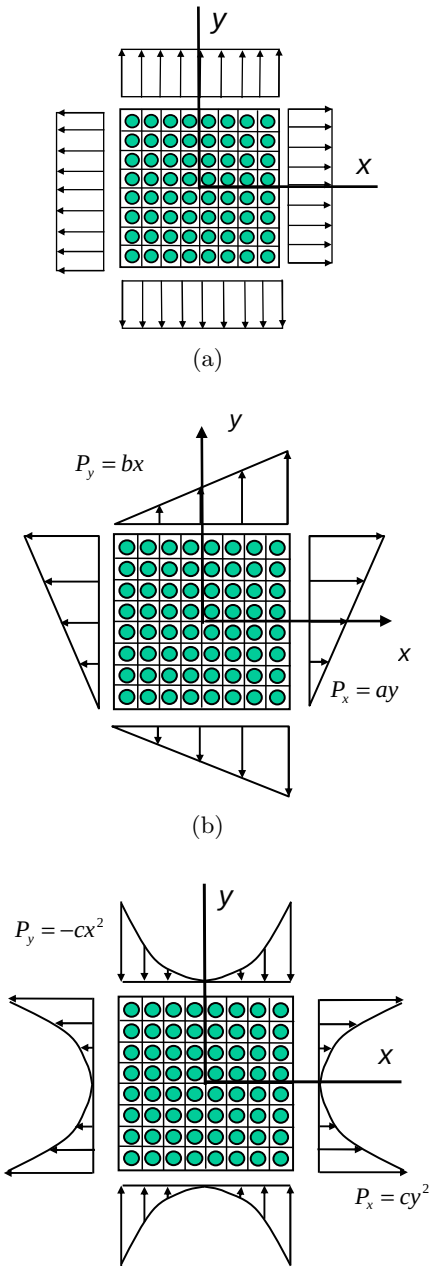

Figure 4.2: Boundary stress with gradient: (a) uniform stress, (b) linear stress, (c) quadratic stress - after [53]

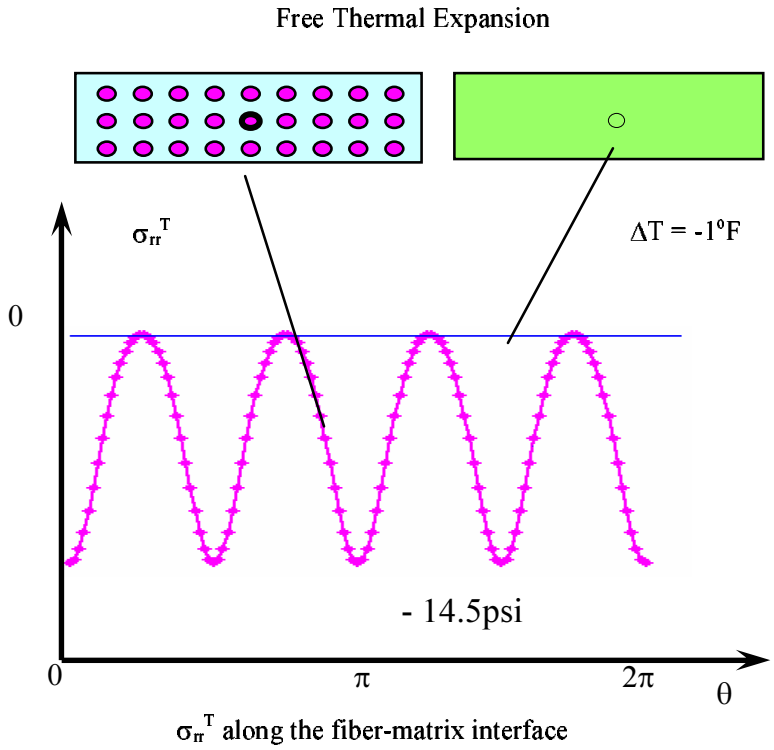

Figure 4.3: Variation of micro radial stress σ_r around a fiber due to $\Delta T = -1^o F$

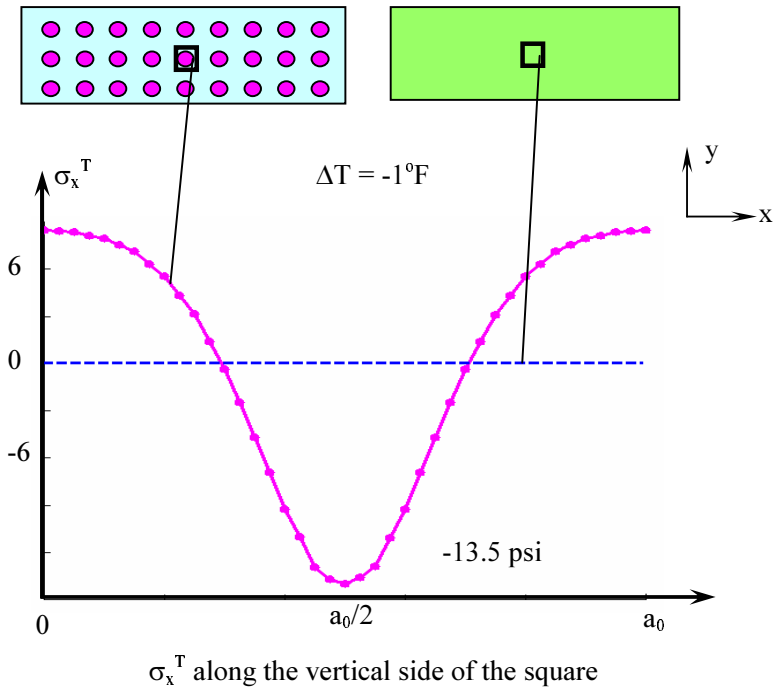

Figure 4.4: Variation of micro thermal stress σ_x along side of unit-square due to $\Delta T = -1^o F$

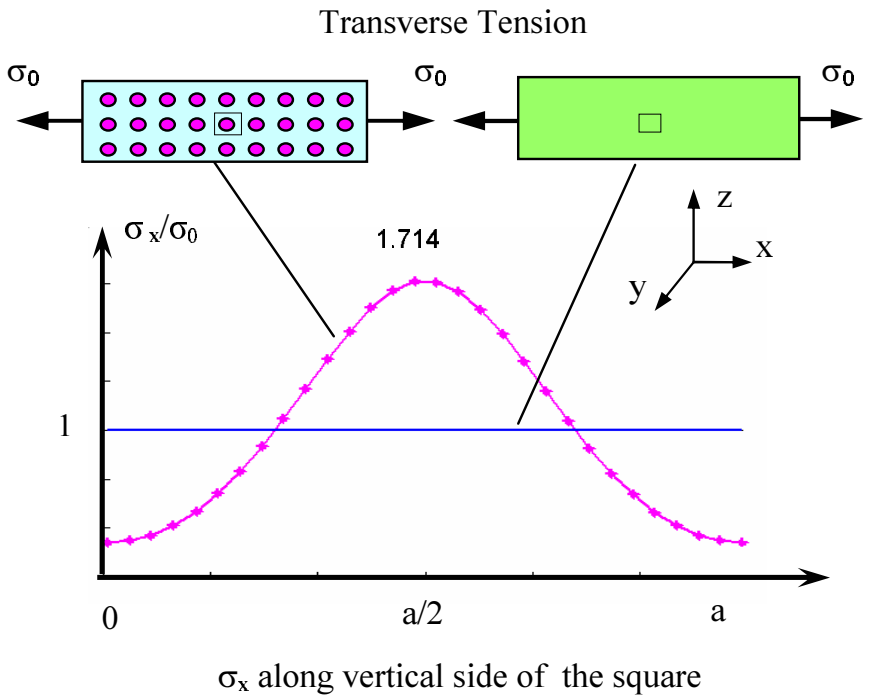

Figure 4.5: Variation of the micro tensile stress σ_x along side of unit-square due to far field stress σ_0

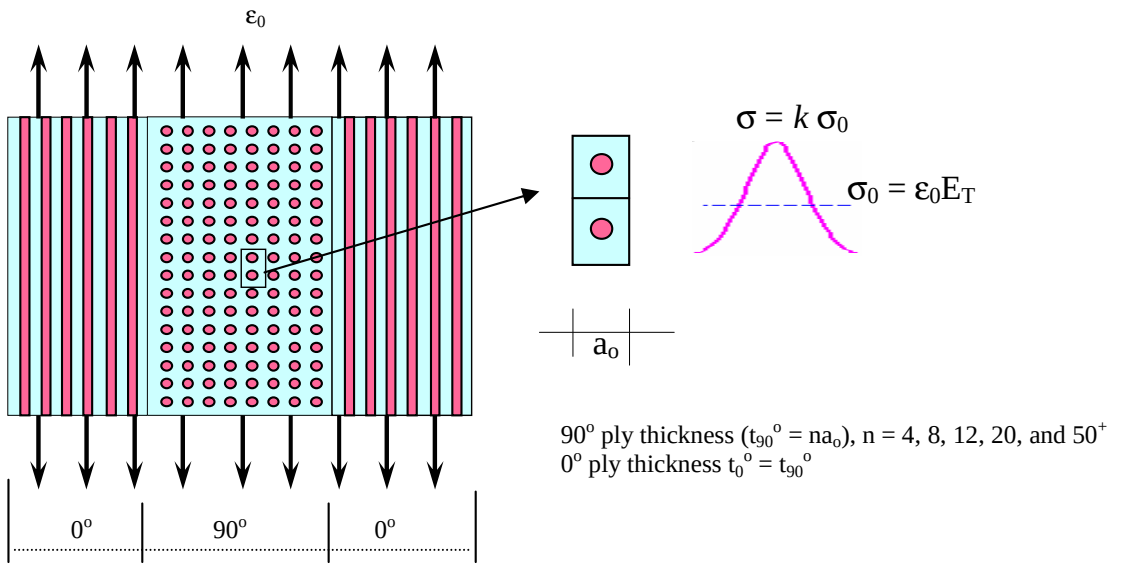

Figure 4.6: Cross-ply laminate under far-field axial strain (left); Micro-field tensile stress between two adjacent square unit cell (inset on right)

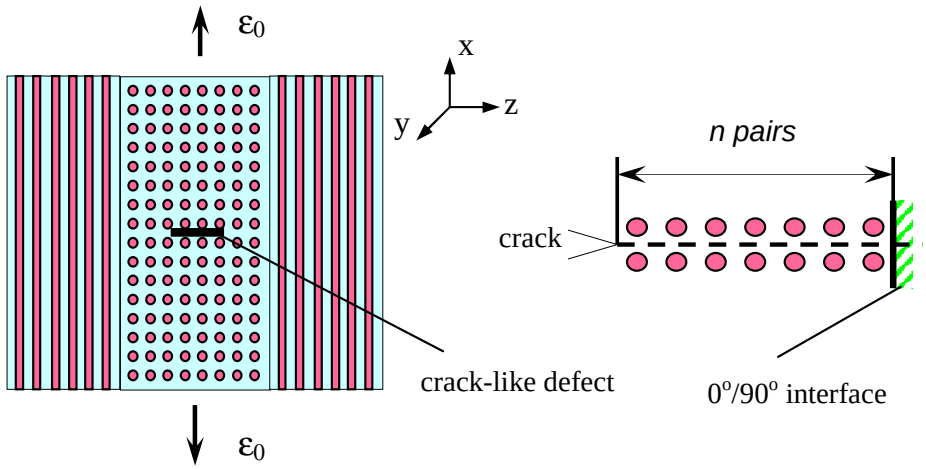

Figure 4.7: Cross-ply laminate under far-field axial strain (left); Micro-field tensile stress between two adjacent square unit cell (inset on right)

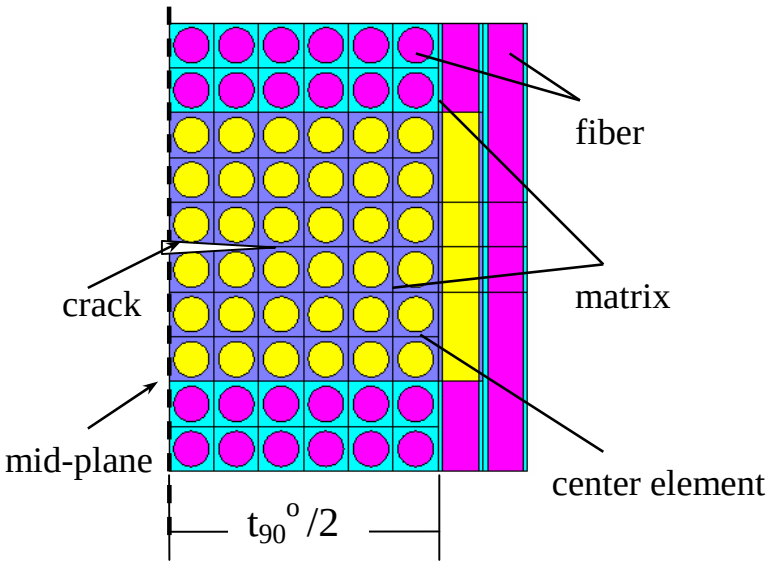

Figure 4.8: A multi-fiber RVE with a center element used in the de-homogenization process for cross-ply laminate with a crack

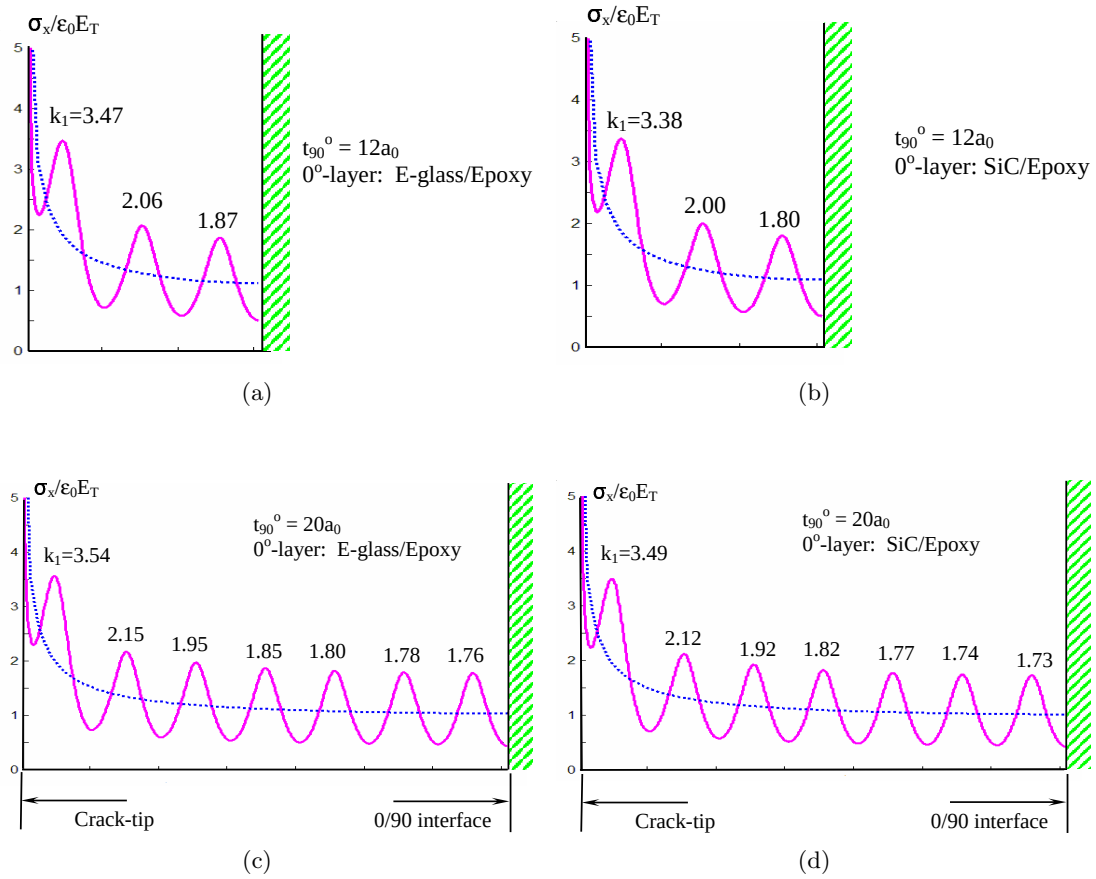

Figure 4.9: Tensile-stress distribution along the crack-line: (a) $t = 12a_0$, $E_L/E_T = 3.4$ (i.e. the 0^o-layer is the E-glass/epoxy system); (b) $t = 12a_0$, $E_L/E_T = 14.7$ (i.e. the 0^o-layer is the SiC/epoxy system); (c) $t = 20a_0$, $E_L/E_T = 3.4$ (i.e. the 0^o-layer is the E-glass/epoxy system); (d) $t = 20a_0$, $E_L/E_T = 14.7$ (i.e. the 0^o-layer is the SiC/epoxy system).

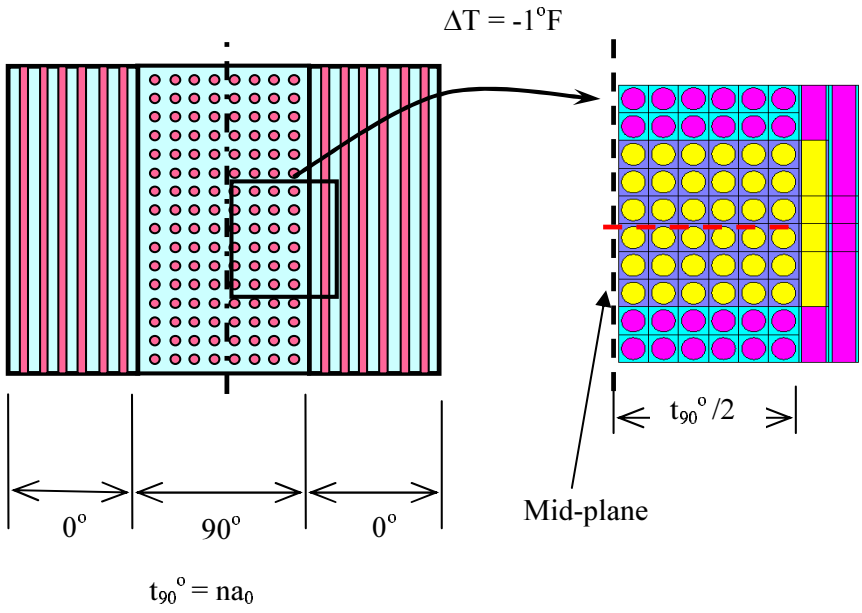

Figure 4.10: Recovery of the micro field across the 90^o thickness in the cross-ply laminate under $\Delta T = -1^o F$.

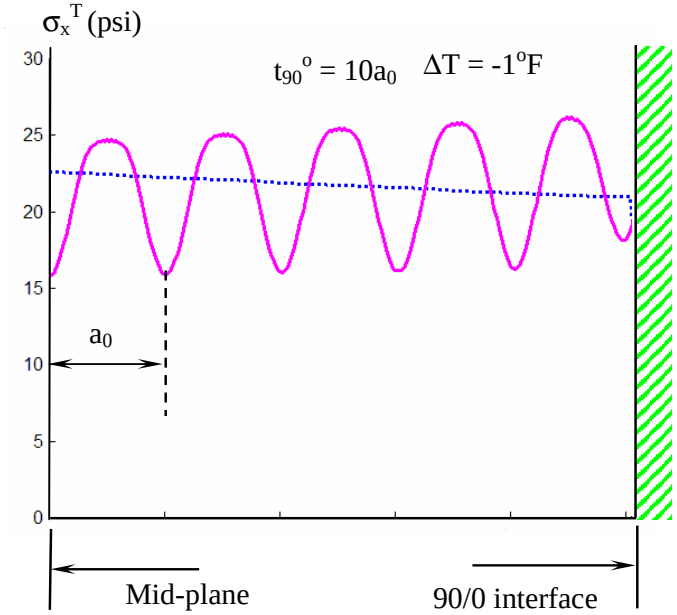

(a)

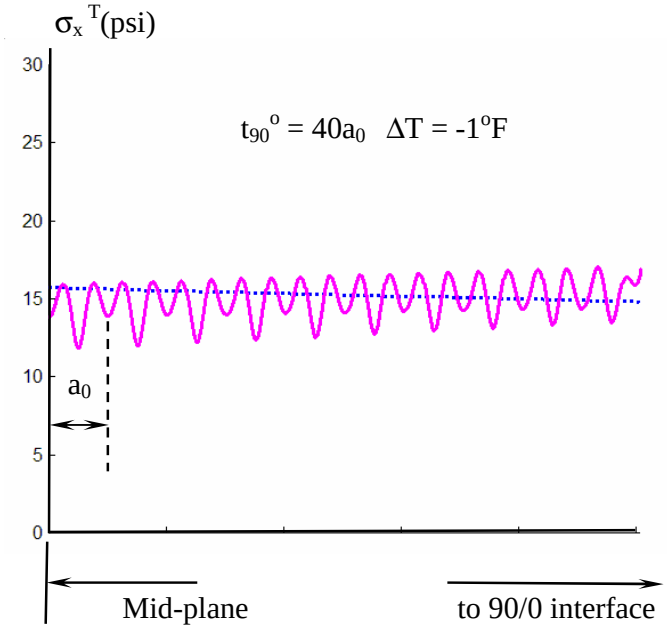

(b)

Figure 4.11: Thermal stress distribution cross the 90^o thickness with fixed $t_{0^o} = 20a_0$: (a) for $t_{90^o} = 10a_0$; (b)for $t_{90^o} = 40a_0$.

Chapter 5: An Inter-Scale Theory For Matrix-Cracking

This chapter describes an inter-scale theory for the onset of matrix-dominated tensile failures in unidirectional and multi-directional laminates that are loaded globally. The theory is formulated at the fiber and matrix scale where the micro field is recovered from the laminate macro-field; but the theory predicts the critically applied global load at the onset of matrix cracking, which is observable at the laminate macro scale.

The description of the inter-scale theory follows a brief review of some key studies on matrix cracking in laminates. In these studies, failure analyses and/or models are macro field based. Most of them are heuristic and/or ad-hoc in nature, thus possess inherent limitations. The inter-scale theory, on the other hand, provides considerable rationality as well as generality, and circumvents most of the predicaments inherent in the macro scale models.

5.1 Matrix Cracking in Laminates under Global Loading

Matrix-dominated tensile failures occur prior to fiber-dominated failures. This is because the matrix and/or the fiber-matrix interface are inherently weaker in tension than the fiber. Thus, when tension normal to the fibers exceeds a certain critical level, matrix-dominated failures occur. Consider the UD laminates loaded in transverse tension. Onset of fiber-separation can result in sudden rupture of the specimen. On the other hand, in multi-directional laminates loaded externally, fiber-separation occur only in the layers

where tension transverse to the fibers is critical. The result is matrix-cracking seen at the laminate macro-scale. Figure 5.1 shows photographs of transverse cracks in a $[\pm 25/90]_s$ graphite/epoxy laminate specimen under axial tension. The x-radiograph on the left is viewed in the x-y plane; multiple transverse cracks are seen to span across the width of the specimen. The microphotograph on the right is viewed in the x-z plane, where transverse cracks are seen to form within the 90^o layer thickness and to terminate at the $90^o(\pm 25^o)$interfaces.

In general, matrix cracking in laminates appears to be non-fatal at first; but accumulation of such cracks could lead to total laminate failure.

Historically, UD laminates loaded under transverse tension are used in experiments to obtain the so-called transverse tensile strength, the latter being the critical macro-scale stress at the specimen rupture. This experiment-derived entity has been regarded, to this date, as one of several basic material strength properties assumed to exist in the UD system. But it has long been documented that the transverse tensile strength obtained experimentally can vary with the size, volume, geometry, loading and other extrinsic factors of the tested specimen. It is not a unique entity that can be deduced in terms of the macro stresses.

As early as in 1973, Kaminski [28] tested a boron/epoxy UD system for the transverse tensile strength. Specimens of three different geometric configurations were used, and each was loaded differently. Namely, a 90^o-coupon loaded under axial tension, a sandwiched beam with 90^o-face sheets loaded in 4-point bending, and a [90]-laminate beam loaded in 3-point bending. Figure 5.2 shows the schematics of the three specimen configurations and the respective loading conditions. All specimens yield sudden tensile matrix failure

observable at the macro-scale; but the critical tensile stresses at the onset of failure differ greatly. Figure 5.3 displays the results obtained by testing more than 50 replicates in each case, where the Weibull survivability versus the transverse tensile strength is plotted. Note the relatively large scattering of the strength values in each test case, and the distinct shift of the survivability curves from the different test methods. Namely, the 90^o coupon test yields the lowest tensile strength, while the [90] beam in 3-point bending provides the highest; the sandwiched beam in 4-point bending gives strength values in between. These results indicate that the homogenized UD system does not have a unique transverse tensile strength, as a material property.

Numerous studies on matrix cracking in multi-directional laminates have also shown that the critical tensile stress initiating matrix cracks in homogenized plies varies with similar non-material factors at the macro-scale [6, 12, 51]. Many criteria have been developed based on macro-field laminate analysis; but none could adequately model the observed failure events [46, 51].

In recent years, there have been increasing efforts in looking into the laminate micro-fields where matrix tensile cracks initiate. The homogenization and de-homogenization schemes presented in Chapter 3 and 4 make it possible to develop a general theory for matrix tensile cracking; the theory is based on the recovered fields at the micro-scale, but predicts failure events at the macro-scale, hence the inter-scale theory.

5.2 The General Theory

Suppose that, upon a rigorous macro-field analysis of a laminate under globally applied load, one of the principal stresses at a certain locality in the laminates is in tension

and transverse to the fibers; macro-scale matrix tensile cracking could suddenly occur at that locality. Let a finite volume be identified at the location where matrix tensile cracking is suspected; the size of the identified volume is larger than the multi-fiber RVE used in homogenization, see Figure 5.4. Through the de-homogenization scheme outlined previously, the microstructure at the fiber-matrix scale is first restored back into the selected volume; and the micro-field is recovered therein.

Inside the recovered micro-field, a pair of parallel fibers is identified randomly, termed as a unit-pair; see the inset of Figure 5.4. Since the pair of fibers are bonded by the matrix and/or the fiber-matrix interface, a material strength X exists between the 2 fibers, which governs the tensile separation of the pair. Here, X is a random variable, with possible values $0 < x < \infty$, described by the probability density function $f(x)$.

Now, let the tensile stress between the parallel fibers in the i^{th} pair be $\sigma_i = k_i\,\sigma_0 + \sigma_T$. Here, $k_i\,\sigma_0$ is the micro field stress component induced by the globally applied load σ_0, k_i being the local stress concentration factor; σ_T is the residual stress due to composite curing. If the net value of σ_i remains tensile, fiber separation is defined as the event that the local tensile strength x becomes less than σ_i. Then, the probability of fiber separation in the i^{th} unit-pair is given by

$$F_i(\sigma_i) = P\{x \leq \sigma_i\} = \int_0^{\sigma_i = k_i\,\sigma_0 + \sigma_T} f(x)dx \tag{5.1}$$

Suppose that there are N connected unit-pairs across the identified volume, and that fiber separation of a single unit-pair can initiate unstable fiber separations of its immediate neighboring pairs. Then, according to the weakest-link theory, which considers statistical

independence for the event of separation in each pair, the probability that the system of N pairs would separate unstably is given by:

$$F_{sys}(\sigma_0) = 1 - \prod_{i=1}^{N}[1 - F_i(\sigma_i)] \tag{5.2}$$

where $\prod$ indicates multiplication.

Equation (5.2) is expressed in terms of the global stress parameter σ_0 and the basic unit-pair strength probability functions, $F_i(\sigma_i)$. Clearly, if a value for $F_{sys}(\sigma_0)$ is specified, the critical σ_0 is found from (5.2).

Note that the above theory is hinged on two key postulations: that a random tensile strength X exists between any fiber-pair in the micro field, and that the connectivity of the unit-pairs in the recovered field is represented by a chain of weakest-links. The first postulation is plausible, as matrix tensile cracking stems from fiber separation; X represents the critical tensile stress that causes such a failure mode at the fiber-matrix scale. The second postulation is, perhaps, applicable only to brittle matrix materials. Both postulations need to be experimentally validated.

In what follows, an experiment is suggested for determining $f(x)$ of the unit-pair; and the experiment may also be used for a validation of the weakest-link postulation.

5.3 Experiment for Determining $f(x)$

For simplicity but without loss of generality, consider the UD composite system with a square fiber array. Let a sample of 90^o tensile coupons be fabricated using this UD system, the coupons being made in a dog-bone shape as shown in Figure 5.5. When

the coupons are tested to failure under the far-field tensile stress σ_0, each would fail as $\sigma_0 \longrightarrow X$. For a sample of large number of coupons, a sample of $\{X\}$, $\{\hat{X}\}$, is thus obtained from the test. Let $F_{sys}(X)$ be the cumulative probability function by fitting the sample $\{\hat{X}\}$. Without loss of generality, let $F_{sys}(X)$ be a three-parameter Weibull function [54]:

$$F_{sys}(X) = 1 - \exp\left[-\left(\frac{X - X_L}{\beta_0}\right)^{\alpha_0}\right], \tag{5.3}$$

where X_L is the lower limit of X; α_0 and β_0 are the shape and scale parameters, respectively. All three are found by fitting the test sample $\{\hat{X}\}$.

Now, let the micro field in the region of the narrowest section of the test coupon be recovered, see Figure 5.5. In particular, since the coupon is loaded uniformly across the width of the coupon at the narrowest section, the tensile stress between the fibers in each and every unit-pair is the same. The latter is expressed in terms of the applied macro stress σ_0: $\sigma = k\,\sigma_0 + \sigma_T$, and the probability that the pair fails at $\sigma = k\,\sigma_0 + \sigma_T$ is given by Equation (5.1). Moreover, if there are N unit-pairs across the narrowest section of the coupon, and coupon separation follows the weak-link postulation, the probability $F_{sys}(\sigma_0)$ that the coupon (a system of N pairs) fails by σ_0 is given by Equation (5.2).

Suppose that $f(x)$ of the unit-pair is also a three-parameter Weibull function, with three parameters x_L, α and β:

$$f(x) = \frac{\alpha}{\beta}\,(\frac{x - x_L}{\beta})^{\alpha}\,\exp\left[-\left(\frac{x - x_L}{\beta}\right)^{\alpha}\right], \tag{5.4}$$

Then, substution of Equation (5.4) into Equation (5.2) yields a Weibull function:

$$F_{sys}(\sigma_0) = 1 - \exp\left[-N\left(\frac{k\sigma_0 + \sigma_T - x_L}{\beta}\right)^{\alpha}\right]. \tag{5.5}$$

By comparing $F_{sys}(\sigma_0)$ in Equation (5.5) with the experimentally fitted function $F_{sys}(X)$ in Equation (5.3) as $\sigma_0 \longrightarrow X$, the parameters x_L, α and β in Equation (5.4) can be related explicitly in terms of X_L, α_0 and β_0:

$$\begin{aligned} x_L &= \sigma_T + k\,X_L \\ \alpha &= \alpha_0 \\ \beta &= k\,\beta_0\,N^{1/\alpha_0}\,. \end{aligned} \tag{5.6}$$

It should be noted that the postulated probability density function $f(x)$ for the unit-pair is obtained based on the postulation of the weakest-link theory; the uniqueness of $f(x)$ so obtained remains an open question. If samples of the test coupons are made with varying width at the narrowest section, a correlation between the test results and the proposed inter-scale theory should provide a possible validation for both postulations.

5.4 Analysis of The Kaminski Problems

The inter-scale theory presented above may explain the distinctive differences in the transverse tensile strengths found in the Kaminski experiment [28].

For the 90^o tension coupon in Figure 5.2(a), the macro stress σ_0 is uniform; but the micro field stress in the unit-pair is $\sigma = k\,\sigma_0 + \sigma_T$. According to the inter-scale theory,

the failure probability of the coupon under σ_0 is given by:

$$F_{sys}(\sigma_0) = 1 - [1 - \int_0^{k\,\sigma_0+\sigma_T} f(x)dx]^N \,. \tag{5.7}$$

where $f(x)$ is the probability density function for fiber separation of the unit-pair; N is the number of unit-pairs across the thickness of the coupon. From Equation (5.7), the critical σ_0 at coupon failure can be determined if a value of $F_{sys}(\sigma_0)$ is specified.

For the sandwiched beam in 4-point bending, as shown in Figure 5.2(b), the macro field at the bottom face sheet is in tension. The tensile stress is slightly non-uniform through the thickness of the face sheet, the largest being at the outer surface of the bottom sheet. Let the latter be denoted by σ_0. The critical σ_0 at tensile failure of the 90^o face sheet is taken as the transverse tensile strength for the UD composite. The recovered micro field in the face sheet provides the tensile stress in the i^{th} pair: $\sigma_i = k_i\,\sigma_0 + \sigma_T$. Here, the numbering of i ($i = 1 \cdots N$) begins at the outer surface of the bottom face sheet, where the macro stress is σ_0. Even without a numerical computation, it is seen that σ_i (or k_i) decreases from the outer surface toward the interior of the face sheet. The reduction of σ_i is due to the slight non-uniformity of the macro stress through the thickness of the sheet and the constraining effect from the stiffer aluminum core of the sandwiched beam. Then, application of Equations (5.1) and (5.2) yields the critical σ_0 for a given value of F_{sys}. In this case, the critical σ_0 is always greater than that found for the 90^o coupon by the same value of F_{sys}. This is obviously due to the reducing σ_i through the thickness of the face sheet.

For the [90] beam tested in 3-point bending, Figure 5.2(c), the macro stress is linearly

distributed through the depth of the beam. Here, the tension field is in the bottom half of the beam, the maximum being at the outer surface. When the maximum stress σ_0 at the outer surface becomes critical, the beam fails. Kaminski treated this critical σ_0 as the transverse tensile strength of the UD composite.

If the corresponding micro fields in the bottom half of the beam is recovered, the tensile stress between the fibers in the i^{th} unit pair is $\sigma_i = k_i\,\sigma_0 + \sigma_T$. Here, again the numbering of i begins at the bottom face of the beam where the macro stress is σ_0. Note σ_i decreases rapidly from the outer surface to the mid-plane. In this case, Equation (5.2) should yield a much lower failure probability for a given value of σ_0. Or, for the same F_{sys} value, the critical σ_0 is much higher than the sandwiched beam.

Due to the lack of specific information concerning the constituents properties, fiber volume content, and the precise geometries in the test specimens, it is not possible to numerically analyze the experimental results presented by Kaminski. The above analysis provides at least a qualitative understanding as to why the UD system does not possess a uniquely determined transverse strength at the macro scale.

5.5 Analysis of the Compact Tension Problem

The compact tension test is commonly used to determine the material toughness of structural solids against fracture, e.g. crack propagation. For the UD composite system under transverse tension, matrix cracking caused by transverse tension is of great concern. The 90^o compact tension test is a way for determining the fracture toughness related to matrix cracking.

Figure 5.6 (a) shows a 90^o compact tension specimen with a side-crack, a_{crack}. When

the specimen is loaded under a uniform far-field tensile strain, say ϵ_0, the crack would propagate unstably in mode-I at a critical value of ϵ_0 ($= \epsilon_{cr}$). According to the theory of linear elastic fracture mechanics (LEFM) [41], the critical value ϵ_{cr} is given as follows:

$$\epsilon_{cr} = \frac{K_{Ic}}{E_T\, H \sqrt{a_{crack}}} \tag{5.8}$$

where K_{Ic} is the critical stress intensity factor (i.e. fracture toughness), and H is a finite correction factor. In correlative compact tension tests, ϵ_{cr} is measured and a_{crack} is given; K_{Ic} is then deduced from Equation 5.8.

In linear fracture mechanics, the mode-I strain energy release rate, G_{Ic}, is often used to represent the material's fracture toughness, instead of K_{Ic}. Their interrelation is obtained through an integration of the stress field near the crack-tip [41]:

$$G_{Ic} = \pi\, K_{Ic}^2 \sqrt{\frac{S_{22}S_{33}}{2}} \left[\sqrt{\frac{S_{33}}{S_{22}}} + \frac{2S_{23} + S_{44}}{2S_{22}} \right]^{\frac{1}{2}}, \tag{5.9}$$

where S_{ij} are compliances of the composite.

In general, for arbitrary large a_{crack}, the deduced K_{Ic} or G_{Ic} is more or less a constant; both are treated as a material property of the homogenized material. However, if a_{crack} is small, the deduced K_{Ic} or G_{Ic} would vary with the size of a_{crack}. This is a well-known dilemma in the theory of linear elastic fracture mechanics. Figure 5.6 (b) shows schematically a comparison between the theoretical and experimental ϵ_{cr} versus a_{crack} relationships. It is seen that, for short cracks, the linear fracture mechanics prediction departs from the experimental results.

With the inter-scale theory outlined previously, the short crack problem in the compact tension test can now be explained with good consistency. The details are presented in the following sub-sections.

5.5.1 Characterization of $f(x)$ of the E-glass/epoxy System

For purpose of a numerical simulation, let the UD composite be the same E-glass/epoxy system as used before, with a square array and $V_f = 50\%$. The properties of the fiber and matrix materials are listed in Table 3.1; and the effective properties of the UD system are obtained by the multi-fiber RVE model, given in Table 4.1.

To characterize the strength function $f(x)$ of the unit-pair in the micro field, let the UD composite specimen be under the transverse tension σ_0 and a uniform temperature drop ΔT. At the macro scale, the specimen is stressed uniformly by σ_0, transverse to the fibers. The thermal residual field is null. At the micro field, however, the maximum tensile stress transverse to the fibers in each unit-pair is $\sigma = k\sigma_0 + \sigma_T$, where $k = 1.714$, $\sigma_T = -13.5psi$ per $\Delta T = -1^oF$. Let the system be cured at the temperature of 350^oF; but the residual stress field is evaluated at the uniform temperature drop of $\Delta T = -200^oF$, allowing post-cure stress relaxation. Then, the thermal residual stress normal to the fibers in the unit pair is, $\sigma_T = -2.62ksi$.

Ideally, the characterization of $f(x)$ for the unit pair is done by conducting a transverse tensile strength experiment, such as suggested in Section 5.3. The experiment would then provide the necessary specimen strength data X, from which the cumulative distribution function $F_{sys}(x)$ is obtained. In the present case, however, pertinent test data is unavailable. But a search in the open literature for comparable test data finds that

most transverse strength tests on glass-epoxy systems do fall in a rather narrow value range. For purpose of numerical illustration, therefore, a hypothetical yet realistic function $F_{sys}(X)$ is assumed, based on the results from the literature search. Namely, $F_{sys}(x)$ is expressed by a Weibull function with the parameters

$$\begin{aligned} X_L &= 2ksi \\ \alpha_0 &= 10 \\ \beta_0 &= 7ksi\,. \end{aligned}$$

The mean value of X is at $8.7ksi$. This is in the range found in most experiments with E-glass/epoxy systems.

For definiteness, let there be 250 connected unit-pairs across the width of the test specimen. This corresponds to about 10 15 plies of such UD system.

The probability density function $f(x)$ for the unit-pair is found in Equation 5.4, which is a Weibull function as well. The parameters in $f(x)$ are found from Equation (5.6):

$$\begin{aligned} x_L &= 0.8ksi \\ \alpha &= 10 \\ \beta &= 20.7ksi\,. \end{aligned} \tag{5.10}$$

5.5.2 Simulation of the Compact Tension Test

Consider the compact tension specimen loaded under the far-field transverse tensile strain ϵ_0, see Figure 5.7; the side crack a_{crack} would propagate self-similarly in mode-I when ϵ_0

reaches a critical value ϵ_{cr}. Here, the micro field containing the crack line is of interest and must be recovered in terms of globally applied ϵ_0 and ΔT. For this purpose, a 80-fiber RVE is used, see the inset in Figure 5.7. Note that the center element inside the RVE contains the crack-line from the crack tip to a length of 6 unit-pairs.

Specimens having the width of $250a_0$ and the initial side-crack size of: $a_{crack} = 0$, a_0, $2a_0$, $3a_0$, $7a_0$, $10a_0$, $15a_0$, and $20a_0$, are simulated. Recall that a_0 is the size of unit square that contains a single fiber. For the E-glass/epoxy system, $a_0 = 0.000505\, in.$

Figures 5.8, 5.9, and 5.10 display the normalized (by σ_0) macro and micro tensile stresses along the crack line, due to the applied stress σ_0 $(= \epsilon_0\, E_T)$. Here, the respective stresses for $a_{crack} = 0$, a_0, and $2a_0$ are shown in Figures 5.8 (a-c); $a_{crack} = 3a_0$, $7a_0$, and $10a_0$ are in Figures 5.9(a-c); and $a_{crack} = 15a_0$ and $20a_0$ are in Figures 5.10(a-b), respectively.

For $a_{crack} = 0$, see Figure 5.8 (a), the macro stress is constant as it should, equaling to σ_0, while the micro stress is oscillating about the macro stress. The micro stress σ_y in the unit-pair is magnified by a concentration factor, $k = 1.714$.

Figure 5.8 (b) shows the respective stresses along the crack line for $a_{crack} = a_0$. The macro field displays a stress concentration near the crack tip; and the micro stress oscillates about the macro stress. Note that the concentration factor k in the unit-pair next to the crack-tip increases to $k = 2.469$, due to the presence of the crack, while the k factors for the rest of unit-pairs along the crack line decay and approach to the far-field value.

The macro and micro stresses along the crack line for a_{crack} from $2a_0$ to $20a_0$ display the similar patterns as those in $a_{crack} = a_0$. However, as the size of the side crack

increases, the k factors in the unit-pairs along the crack line becomes larger, especially the one in the unit-pair next to the crack tip. For instance, when $a_{crack} = 2a_0$, $k_1 = 3.109$; and k_1 increases to 3.263, 5.235, 6.179, 7.486, and 8.555 for $a_{crack} = 3a_0$, $7a_0$, $10a_0$, $15a_0$, and $20a_0$, respectively.

The residual stress σ_y^T along the crack-line is null at the macro scale; but it is non-zero at the micro scale. Figure 5.11 shows the micro field σ_y^T per $\Delta T = -1^o F$ along the crack line for $a_crack = a_0$. It is seen that the distribution pattern near the crack tip is somewhat disturbed by the presence of the side crack. The maximum crack-tip σ_y^T is in tension; in the unit-pair, σ_y^T remains compressive between fibers. The magnitude of the compressive σ_y^T is slightly larger than that when $a_{crack} = 0$. Furthermore, the size of a_{crack} has little influence on σ_y^T.

With the micro field solutions computed, the failure probability F_{sys} for the compact tension specimen under the applied strain ϵ_0 and $\Delta T = -200^o F$ is then expressed by Equation (5.2). Thus, if a value for F_{sys} is given, the critical strain ϵ_{cr} at the specimen failure is then computed from Equation (5.2).

Alternatively, Equation (5.2) can be used to compute the survivability $(1 - F_{sys})$ versus σ_{cr} $(= \epsilon_{cr} E_T)$ curve. Figure 5.12 (a) displays the survivability $(1 - F_{sys})$ versus σ_{cr} $(= \epsilon_{cr} E_T)$ curves for $a_{crack} = 0$, a_0, $2a_0$, $3a_0$, $7a_0$, $10a_0$, $15a_0$, and $20a_0$. Here, σ_{cr} is normalized by $(\beta_0 + X_L)$. The reason is that, for $a_{crack} = 0$, F_{sys} is a Weibull function; at the characteristic value of $\sigma_{cr} = \beta_0 + X_L$, F_{sys} is 63.2% corresponding to σ_{cr}.

When $a_{crack} > 0$, F_{sys} is not a Weibull function. The actual dependence of σ_{cr} on a_{crack} can be seen when F_{sys} is assigned a definitive value. Figure 5.12(b) shows the computed σ_{cr} versus a_{crack} curve for $F_{sys} = 63.2\%$. The σ_{cr} vs. a_{crack} curve is valid,

regardless the size of a_{crack}: large, small or null. Moreover, the trend of the curve agrees with that found experimentally. The only material strength property input to the inter-scale theory is the $f(x)$ function, postulated as the basic strength of the unit pair.

It is interesting to note that the σ_{cr} versus a_{crack} curve provided by the inter-scale theory coincides with the linear elastic fracture mechanics (LEFM) theory for $a_{crack} = 15a_0$ or larger. The reason is that the k factor in the unit-pair next to the crack tip is large if a_{crack} is large. It can become the most dominant term in the failure probability Equation (5.2). This dominance is acute to the LEFM theory where the crack-tip stress intensity factor determines the onset of unstable crack propagation. If the curve beyond $a_{crack} = 15a_0$ is fitted by the LEFM equation (5.8), a value for $K_{Ic} = 0.6ksi.in^{1/2}$ (or $G_{Ic} = 119J/m^2$) is obtained. This value of K_{Ic} (or G_{Ic}) is in the range found from the compact tension tests for most epoxy-based UD systems.

Figure 5.13 (a) shows the comparison of the σ_{cr} versus a_{crack} curves computed by the inter-scale theory (solid curve) and the LEFM theory (dashed curve). For short cracks, the dashed curve departs dramatically from the solid curve, while the solid curve captures the experimental trend (Figure 5.6). In addition, the inter-scale theory can also provide the well-known R-curve for small side cracks. In this case, ϵ_{cr} from the inter-scale theory is used in Equation (5.8), which renders a value for K_{Ic}, for a given a_{crack}. Figure 5.13 (b) shows the K_{Ic} growth curve as a function of a_{crack}. It is seen that K_{Ic} grows to the asymptotic value of $K_{Ic} = 0.6ksi.in^{1/2}$, as a_{crack} becomes larger than $15a_0$.

5.6 Transverse Cracking in Cross-ply Laminates

5.6.1 A Brief Background Review

In multi-directional laminates, the so-called "transverse cracking" occurs in plies where tension normal to the fibers becomes critical [7, 11, 12, 50]. Figure 5.14 shows a $[0/90]_s$ laminate loaded in axial tension, where transverse cracks occur in the 90^o layer.

In 1977, Garrett and Bailey [11] conducted experiments using laminates in the form of [0/90/0] made of a glass/polyester system. Tensile specimens were fabricated with the thickness of the outside 0^o layers kept constant at $1.0mm$, and the thickness of the middle 90^o layer varied from 0.75 to $3.2mm$. Under the applied laminate tensile strain ϵ_0, one or more transverse cracks in the 90^o layer were recorded. It was then reported that the critical applied strain at the onset of the 90^o layer cracking varied with the thickness of the 90^o layer. Specifically, the critical strain decreases as the 90^o layer thickness increases, see Table 5.1. The subsequent experiments have been conducted using graphite/epoxy laminates [12, 51]. Similar 90^o-layer effects were observed, see Table 5.2.

There have been many analyses and modelling studies on the transverse cracking problem [34, 36, 48, 50, 51]. In all cases, the laminate field are analyzed at the homogenized ply (macro) scale; and the fields are computed by a 2D or a 3D analysis laminated plate model. Transverse cracks are deemed to occur in plies where the tensile stress normal to the fibers exceeds the transverse strength of the ply. But such a failure criterion could not explain the thickness-dependance nature of the transverse cracking. The predicament here is similar to that encountered in the Kaminski's experiment.

A heuristic approach, based on the concept of effective flaws, was developed by Wang,

Table 5.1: Experimental results for the onset strain of transverse cracking in cross-ply laminate made of glass/polyester, after [11].

90^o-ply thickness (mm)	Critical strain at onset of cracking
0.75	0.48%
1.5	0.50%
2.0	0.44%
2.6	0.38%
2.7	0.40%
3.2	0.37%

Table 5.2: Experimental results for the onset strain of transverse cracking in cross-ply composite laminates. (a) Carbon/Epoxy laminates -after [12], (b) Graphite/Epoxy laminates -after [51].

	$[0_4/90_n/0_4]^{(a)}$ transverse cracking strain (onset)	$[0_2/90_n/0_2]^{(b)}$ transverse cracking strain (onset)
$n = 1$	0.65%	N/A
$n = 2$	0.4%	$0.55 - 0.57\%$
$n = 4$	0.35%	$0.29 - 0.36\%$
$n = 8$	0.3%	$0.24 - 0.28\%$

et.al. [50], who stipulated that the 90^o layer possesses materially a distribution of effective flaws, some being oriented in the ply thickness direction. When the 90^o layer is stressed under transverse tension, the flaws act like small cracks; and the most dominant ones would propagate into transverse cracks. Such cracking events are then modelled by the fracture mechanics theory. In order to quantitatively determine the critical laminate load at the onset of the cracking events, the sizes and locations of the effective flaws must be provided ,along with the fracture toughness (K_{Ic} or G_{Ic}) of the homogenized 90^o layer.

However, the effective flaw concept remains heuristic at best. The sizes and locations of the effective flaws must scale with the 90^o layer thickness. The assumed flaw distributions can only be experimentally corrected; their uniqueness can not be proven.

5.6.2 Application of the Inter-scale Theory

In this section, the thickness-dependence character of transverse cracking event in laminates will be analyzed using the inter-scale theory. To be specific, consider a $[0/90]_s$ laminate made of the same E-glass/Epoxy system, with a square array and $V_f = 50\%$ as before. Let the thickness of the 0^o layer (t_{0^o}) be fixed at $20a_0$, and the thickness of the 90^o layer (t_{90^o}) be varying from $4a_0$, $10a_0$, $20a_0$, $40a_0$, and $80a_0$ respectively. The laminate is subjected to an axial tensile strain ϵ_0 as well as a thermal residual temperature drop $\Delta T = -200^o F$.

The laminate macro fields are computed by using the classical lamination theory. The macro stress in the 90^o layer is denoted as $\sigma_0 = \epsilon_0 E_T + \sigma_T^0$. Here, $\epsilon_0 E_T$ is independent of the 90^o layer thickness, while σ_T^0 decreases with the thickness of the 90^o layer; both are uniform in the 90^o layer.

The micro fields in the 90^o-layer is recovered using the multi-fiber RVE. The detailed recovery process has been described earlier in Section 4.3.2.

The stress between the fibers in each unit pair is denoted as: $\sigma = k\,\epsilon_0 E_T + \sigma_x^T\,\Delta T$. The first term is due to the mechanical load ϵ_0, and the second term is due to the thermal residual temperature of $\Delta T = -200^o F$.

Figure 5.15 shows the micro stress (normalized by $\epsilon_0 E_T$) from the mechanical load along the 90^o layer thickness direction, for $t_{90^o} = 4a_0$ and $20a_0$, respectively. Here, the micro stress is oscillating about 1 due to the fiber-to-fiber interaction. When $t_{90^o} = 4a_0$, the stress concentration factor k is 1.671; when $t_{90^o} = 20a_0$, $k = 1.697$. (Note that $k = 1.714$, when $t_{90^o} \to \infty$.) It is seen that k increases slightly with thickness of the 90^o layer, indicating a small degree of the 0^o-layer constraining effect.

The thermal residual stress σ_x^T includes contributions from thermal mismatch between the 0^o and the 90^o layers at the macro scale as well as that between the fiber and matrix at the micro scale. The former induces a tensile micro field in the 90^o layer; its average value decreases with the thickness of the 90^o layer. The latter induces a self-equilibrated micro field. The distribution of σ_x^T along the 90^o thickness direction for $t_{90^o} = 10a_0$ and $40a_0$ are shown previously in Figure 4.11. Note that the distribution pattern and the value of σ_x^T vary with the thickness of the 90^o layer.

Within the context of the inter-scale theory, for the UD system considered, the probability density function $f(x)$ is a 3-parameter Weibull function, with the parameters given in Equation (5.10). If the stress between the fibers in a unit pair is tensile, the probability that fiber separation occurs is given by Equation (5.1).

According to the weakest-link assumption, fiber separation in one unit pair can propagate unstably and result in a large crack in the thickness of the 90^o layer; this defines the onset of the transverse cracking. The probability F_{sys} for the onset of transverse cracking in the 90^o layer is then given by Equation (5.2). Alternatively, if a value of F_{sys} is given, the critical strain ϵ_{cr} for the onset of transverse cracking can also be computed from Equation (5.2). Figure 5.16 shows the survivability R_{sys} $(= 1 - F_{sys})$ curves as a function of ϵ_{cr} for $t_{90^o} = 4a_0, 10a_0, 20a_0, 40a_0$, and $80a_0$, respectively. Note that the curves shift to the left as t_{90^o} increases.

Figure 5.17 shows the computed ϵ_{cr} curves as a function of the 90^o layer thickness for $F_{sys} = 63.2\%$, 90%, and 99%, respectively. It is seen that, when t_{90^o} is small, the onset strain ϵ_{cr} decreases sharply with the 90^o layer thickness; when t_{90^o} is large, ϵ_{cr} approaches a constant value. This trend is consistent with that observed in numerous experiments, see e.g. Table 5.1. It is interesting to note that the computed ϵ_{cr} for $t_{90^o} = 20a_0$ is in the range of $4500 \sim 5500\mu\epsilon$. Here, $20a_0$ corresponds to $0.011in$ or $0.26mm$; this is roughly 2-ply thickness for commercial epoxy-based UD tapes. Most experimental values for ϵ_{cr} in such cases range from 5500 to $5700\mu\epsilon$, see e.g. [51].

5.6.3 Effective Flaws at the Macro Scale

As mentioned previously, the problem of transverse cracking in cross-ply laminates has been treated by introducing the effective flaws at the macro scale and using the fracture mechanics approach, see [31, 50]. Figure 5.18(a) shows the schematics of the laminate that contains the most dominant flaw with a size of a_e. But in order to correlate with the experiments, the size of a_e must scale with the 90^o layer thickness.

The inter-scale theory can now be used to augment the fracture mechanics analysis at the macro scale. Specifically, from the results of the inter-scale analysis, the appropriate effective flaw size a_e can be deduced, along with the value of K_{Ic}. Note the both have to be experimentally deduced, if the analysis is at the macro scale.

The K_{Ic} was found earlier in the simulated compact tension test described in section 5.5.2. For the E-glass/epoxy UD system used, a value of $K_{Ic} = 0.6ksi \cdot in^{1/2}$ was obtained.

As for the effective flaw size a_e, it can be deduced from the inter-scale theory in the following way: By means of the macro scale fracture analysis, using $K_{Ic} = 0.6ksi \cdot in^{1/2}$, a plot of ϵ_{cr} versus a_e is computed. Figure 5.18(b) shows the computed ϵ_{cr} versus a_e curves (solid curves), for $t_{90^o} = 20a_0$, $40a_0$ and $80a_0$, respectively. Note that these curves are unbounded as a_e becomes smaller. This is expected because the fracture mechanics theory is not for small a_e. But, the inter-scale analysis yields readily $\epsilon_{cr} = 4260\mu\epsilon$ for $t_{90^o} = 20a_0$; $4100\mu\epsilon$ for $t_{90^o} = 40a_0$; and $4003\mu\epsilon$ for $80a_0$, as they are read from Figure 5.17. With the inter-scale solutions and the corresponding fracture mechanics solutions, a_e can be readily deduced from the curves: $a_e = 3.9a_0$, $6.4a_0$ and $7.4a_0$. Note that the value of a_e so deduced does scale with the thickness of the 90^o layer. Furthermore, these value appear to be in the range of a_e used by Lei [31] and Wang, et.al [50].

5.7 Summary

In summary, the inter-scale theory is formulated at the fiber-matrix scale to simulate matrix cracks observed at the macro scale. The physical basis of the theory is that fiber separation in a unit-pair is governed by a random tensile strength X with a real value x in the range $0 < x < \infty$. The probability density function of X, $f(x)$, serves as the only

basic material input, which must be carefully characterized by a suitable experiment. The theory is applied to several known matrix cracking problems with consistent results.

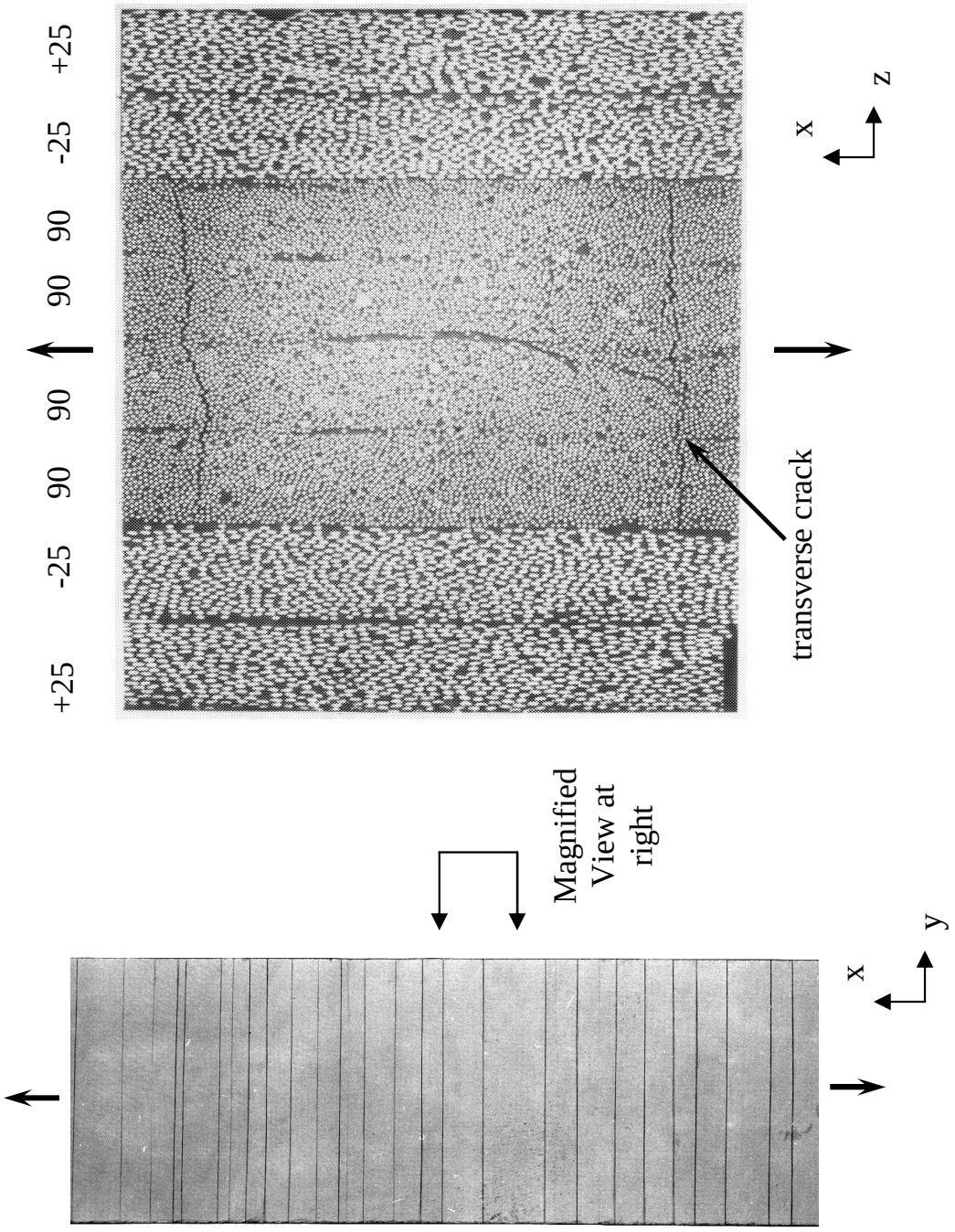

Figure 5.1: Photograph Showing Transverse cracks in the 90^o-layers of a $(\pm 25/90_2)_s$ specimen, after [30].

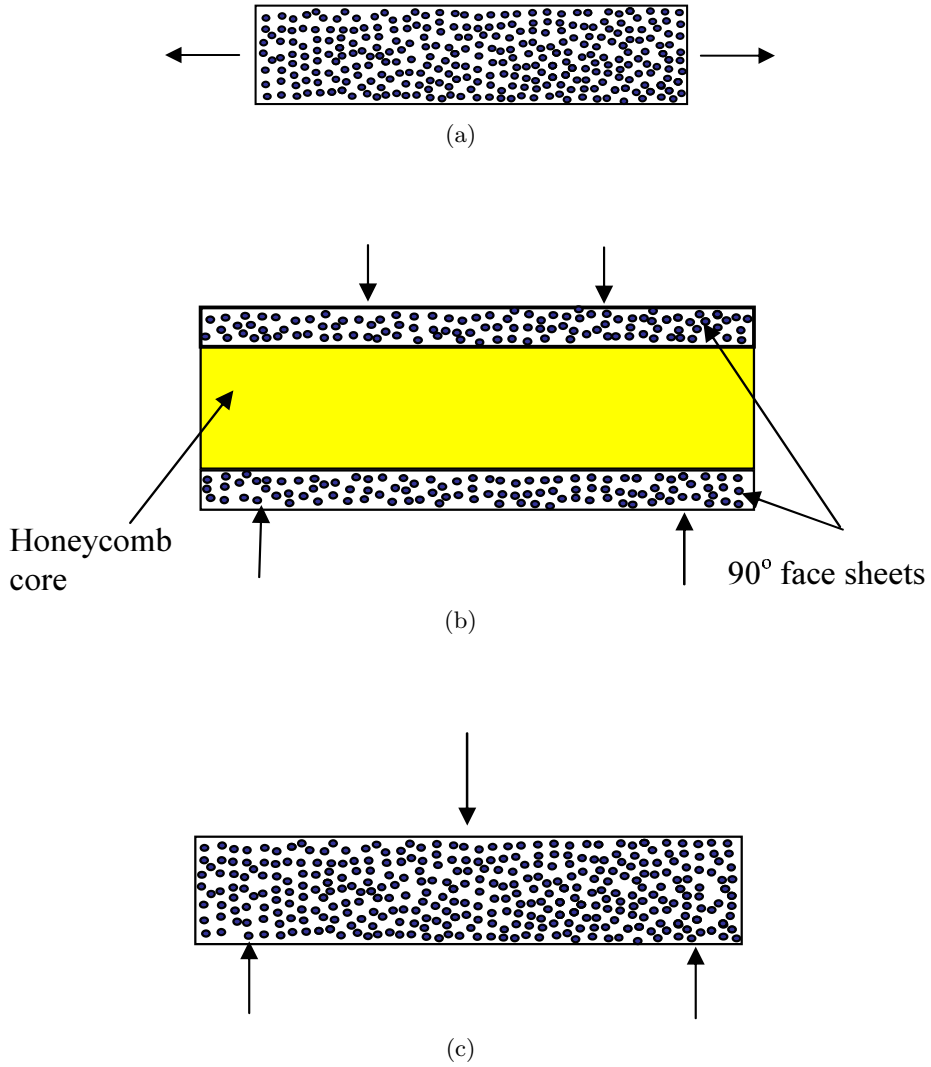

Figure 5.2: Schematics of specimens in Kaminski's experiment: (a)a 90^o coupon under tension (b) a sandwiched beam under 4-point bending (c) a [90] laminate beam under 3-point bending, after [28].

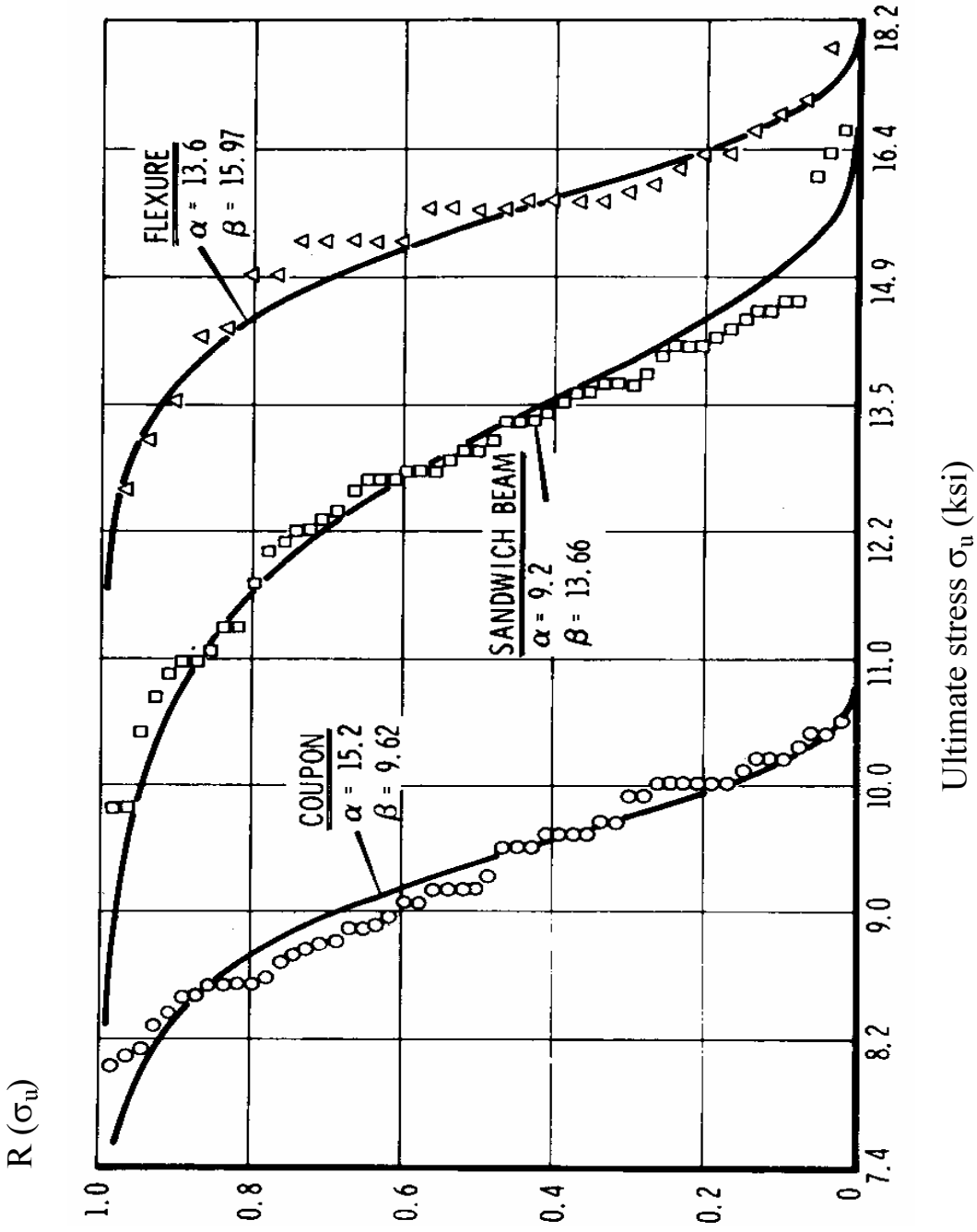

Figure 5.3: Experimental data for transverse strength of Boron-epoxy UD composite, after [28].

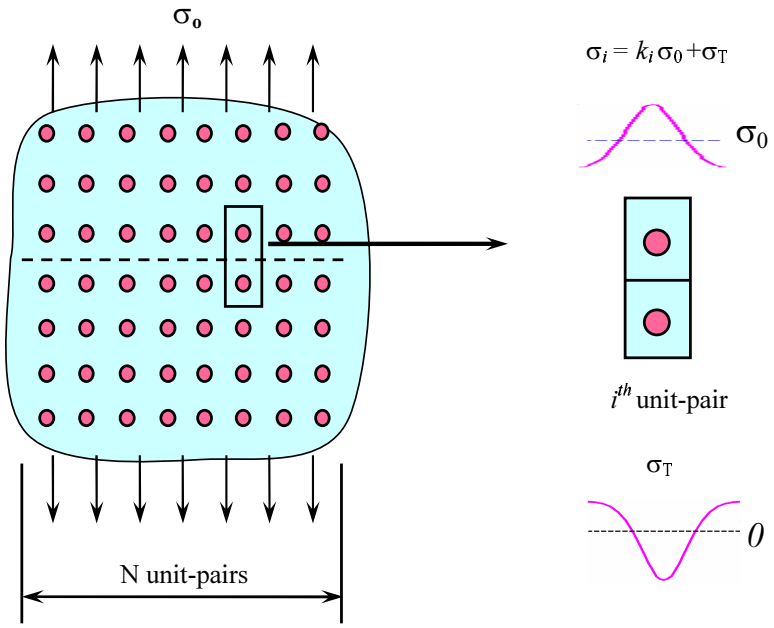

Figure 5.4: A schematic of a specimen with N unit pairs across the width, under transverse tension(left); the inset (right): the i_{th} pair, and micro stress by σ_0 and ΔT.

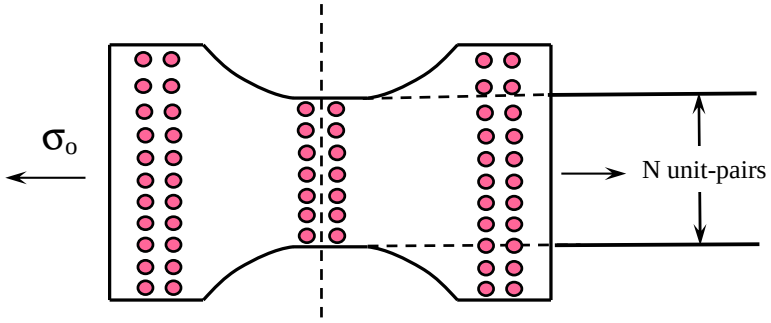

Figure 5.5: A dog-bone shaped specimen made of a model composite with a square array.

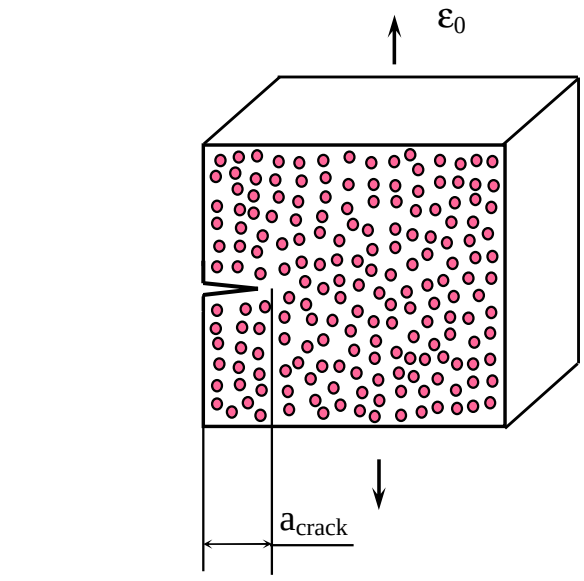

(a)

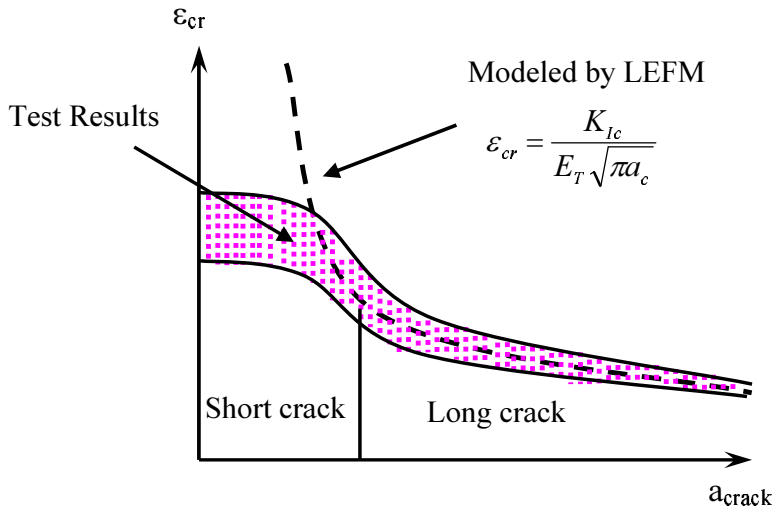

(b)

Figure 5.6: Compact tension test: (a) a specimen with a side-crack, a_{crack}, (b) a schematic show of the correlation between fracture mechanics model and experimental result.

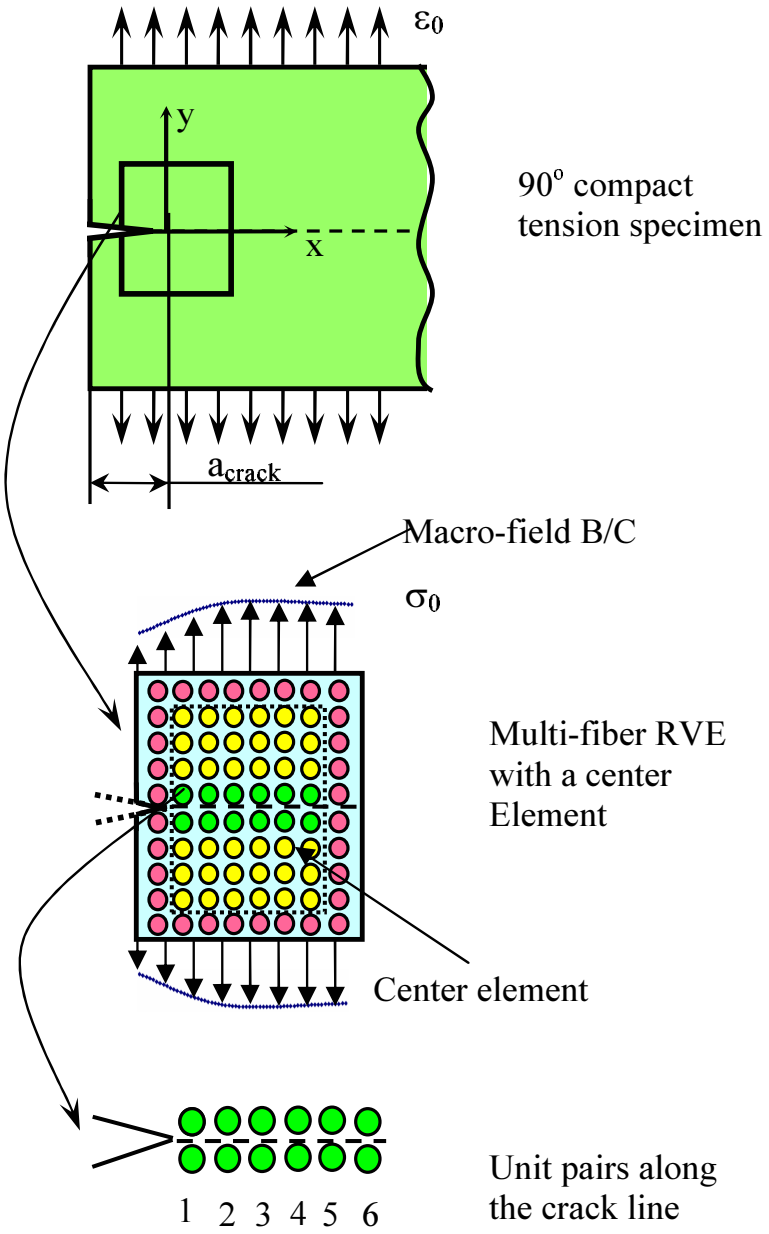

Figure 5.7: Recovery of the micro field along the crack line in the compact tension specimen.

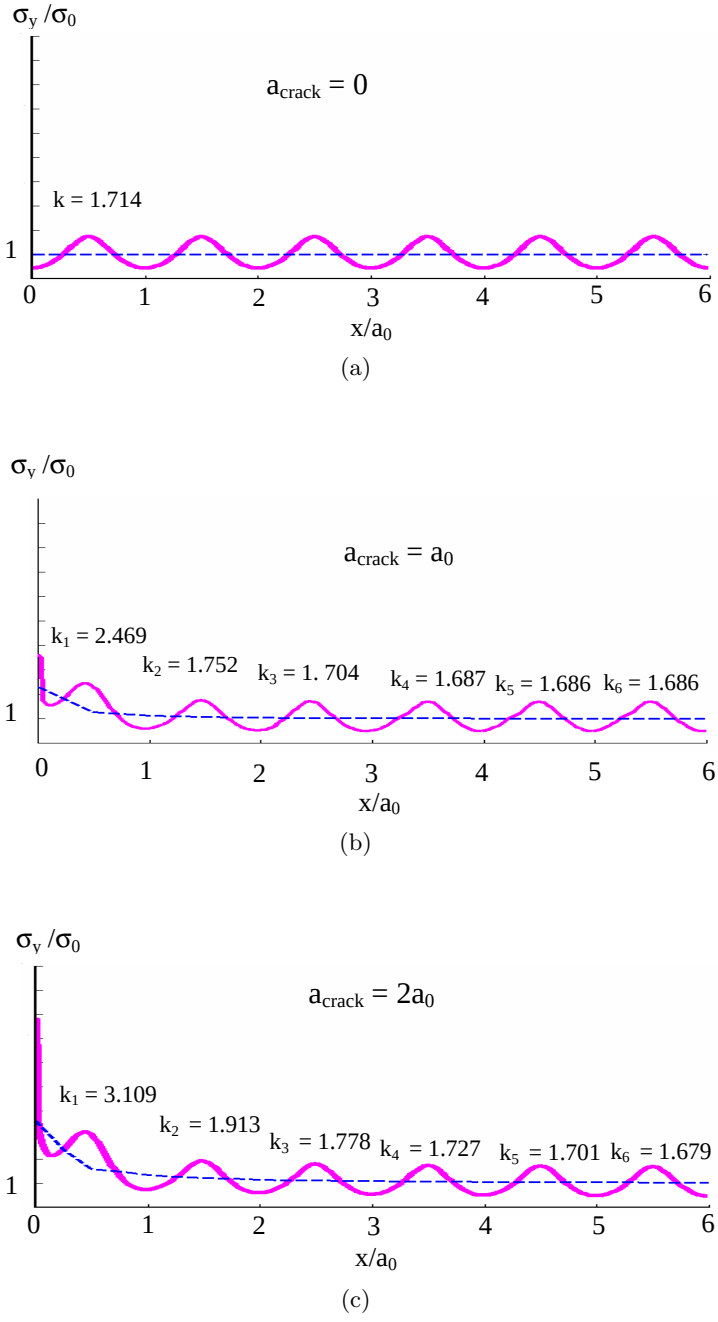

Figure 5.8: The distribution of the micro tensile stress along the crack line: (a) $a_{crack} = 0$, (b) $a_{crack} = a_0$, (c) $a_{crack} = 2a_0$.

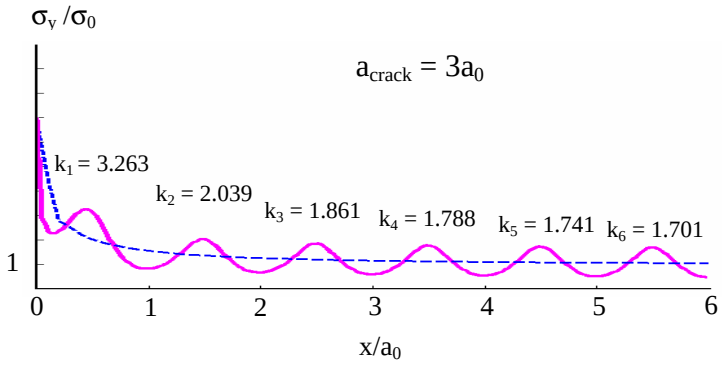

(a)

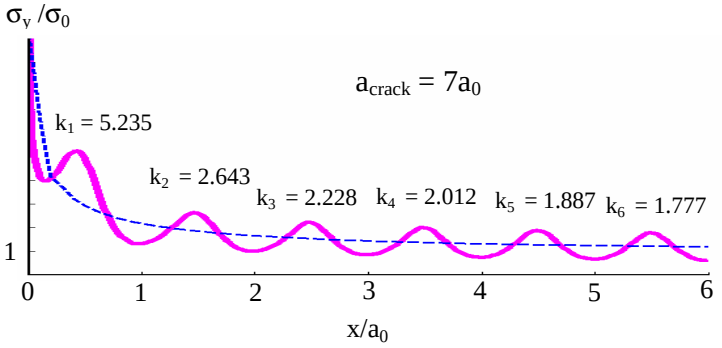

(b)

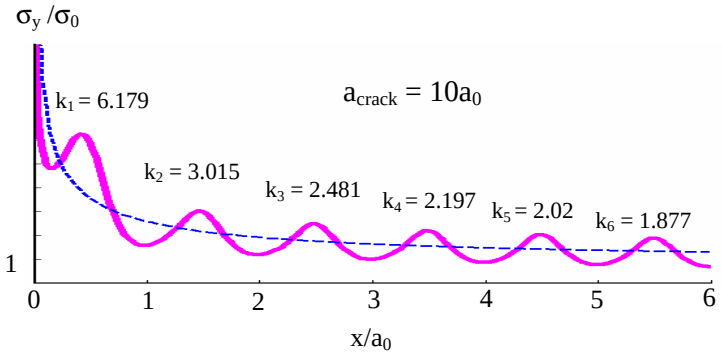

(c)

Figure 5.9: The distribution of the micro tensile stress along the crack line: (a) $a_{crack} = 3a_0$, (b) $a_{crack} = 7a_0$,(c) $a_{crack} = 10a_0$.

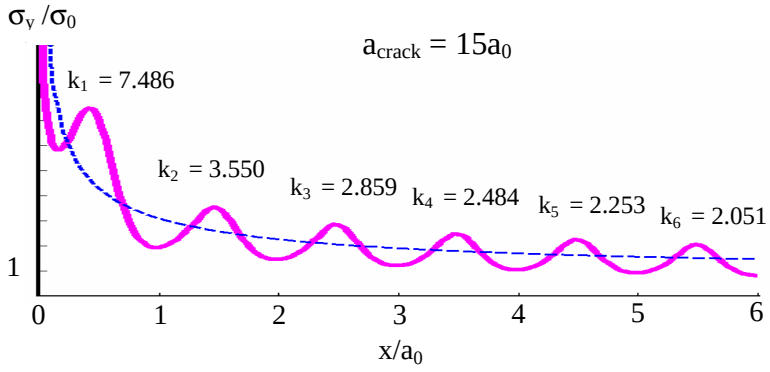

(a)

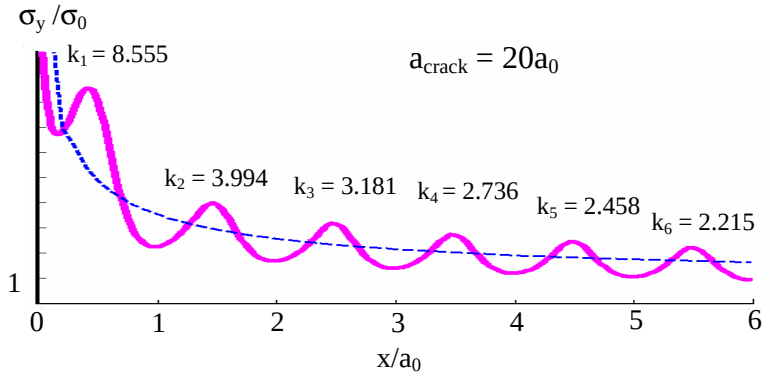

(b)

Figure 5.10: The distribution of the micro tensile stress along the crack line: (a) $a_{crack} = 15a_0$, (b) $a_{crack} = 20a_0$.

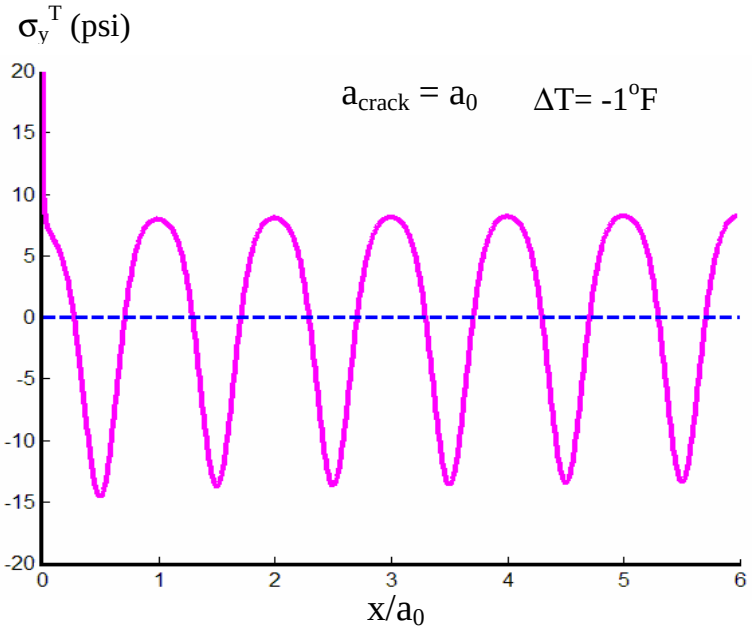

Figure 5.11: The distribution of the micro thermal stress along the crack line for $a_{crack} = a_0$ and$\Delta T = -1^o F$.

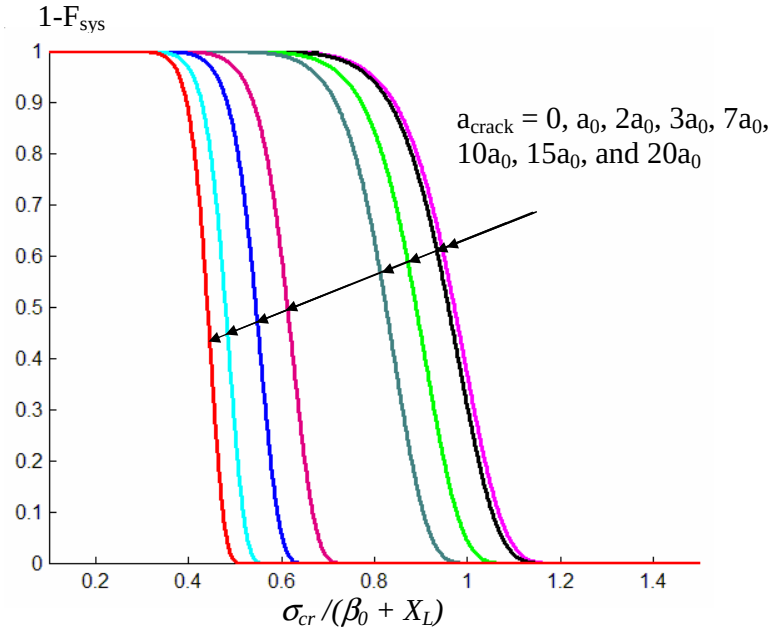

(a)

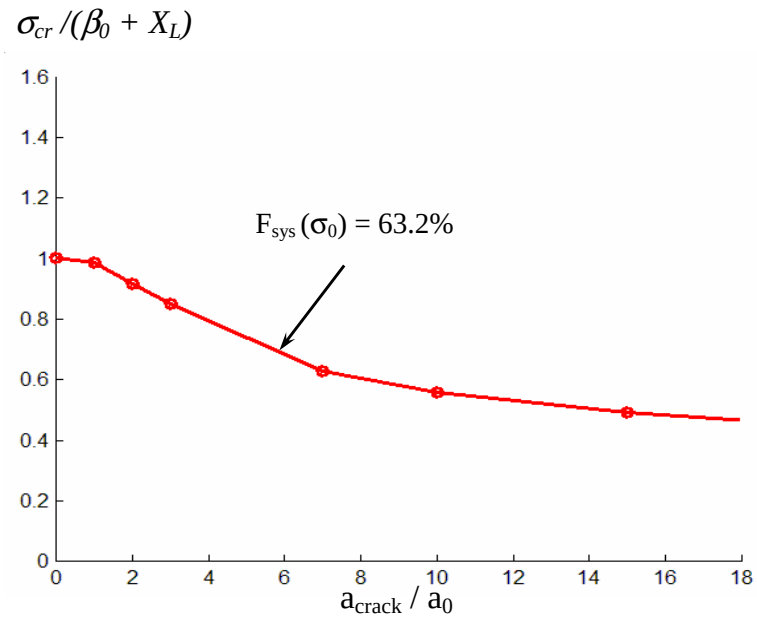

(b)

Figure 5.12: Prediction of critical load for compact tension specimen via the inter-scale theory: (a) reliability of compact tension specimens with a_{crack} from 0 to $120a_0$, (b) predicted critical load v.s. the size of crack.

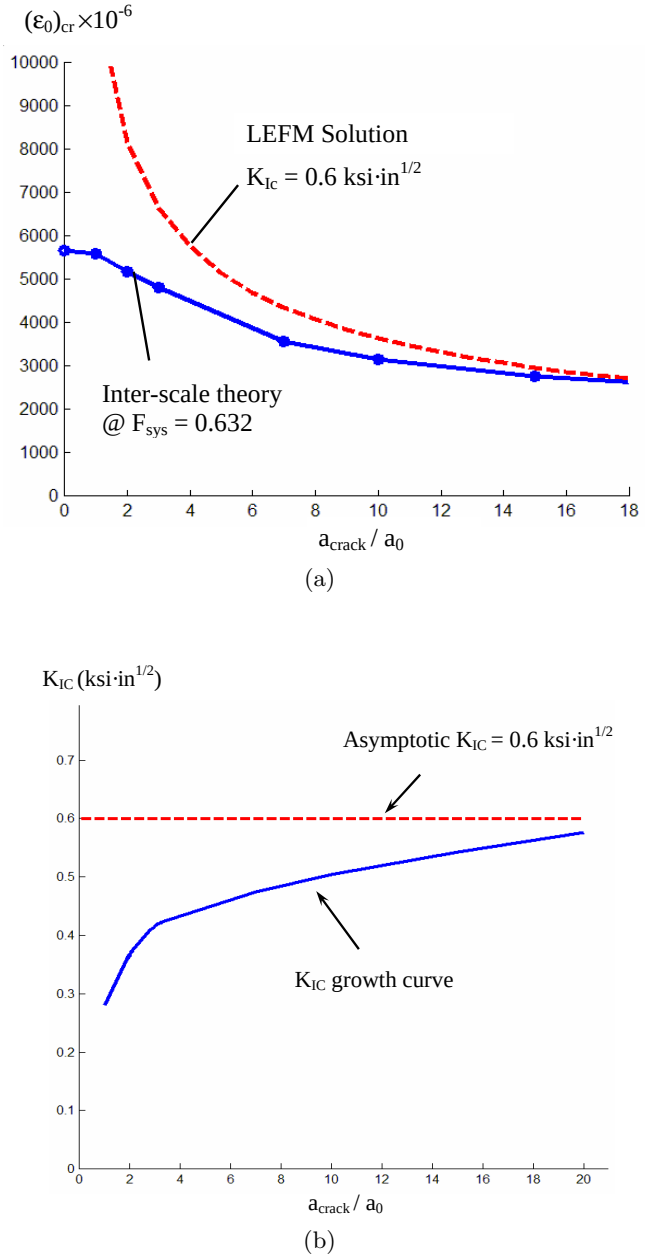

Figure 5.13: Comparison between the inter-scale failure theory and fracture mechanics approach: (a) critical strain ϵ_{cr} v.s. the size of crack, (b) K_{Ic} v.s. the size of crack.

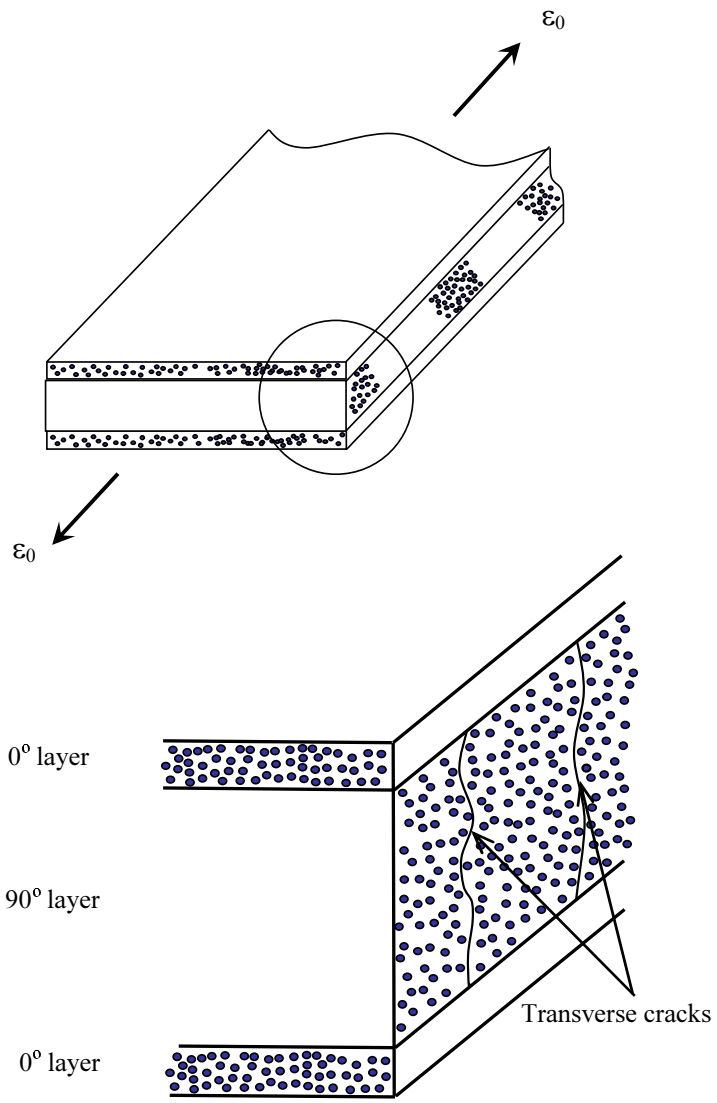

Figure 5.14: A schematic of transverse cracks in a cross-ply laminate under axial tension.

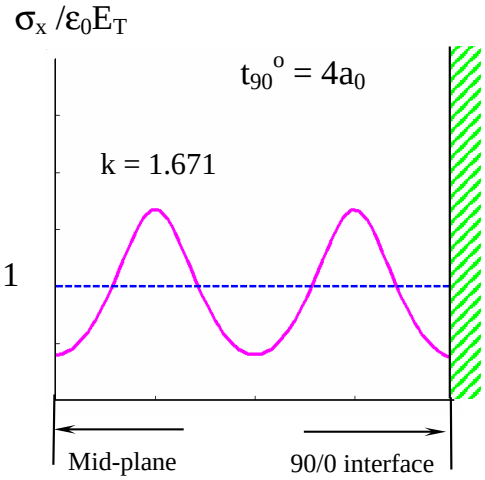

(a)

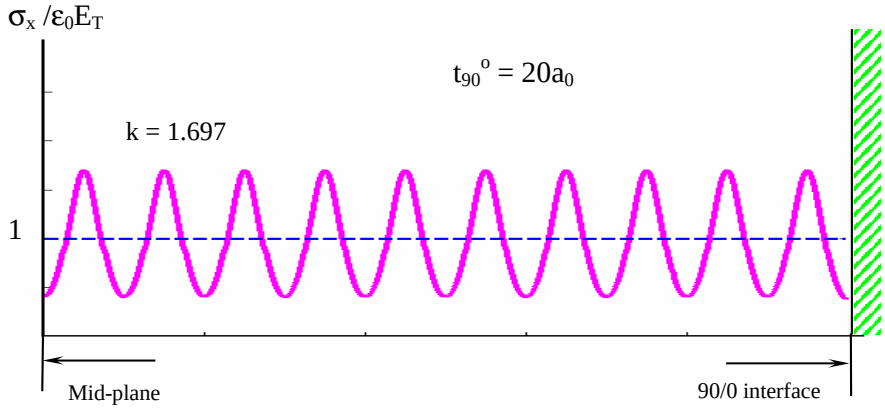

(b)

Figure 5.15: The micro stress distribution along the thickness direction of the 90^o layer, due to the axial strain ϵ_0: (a) $t_{90^o} = 4a_0$, (b) $t_{90^o} = 20a_0$.

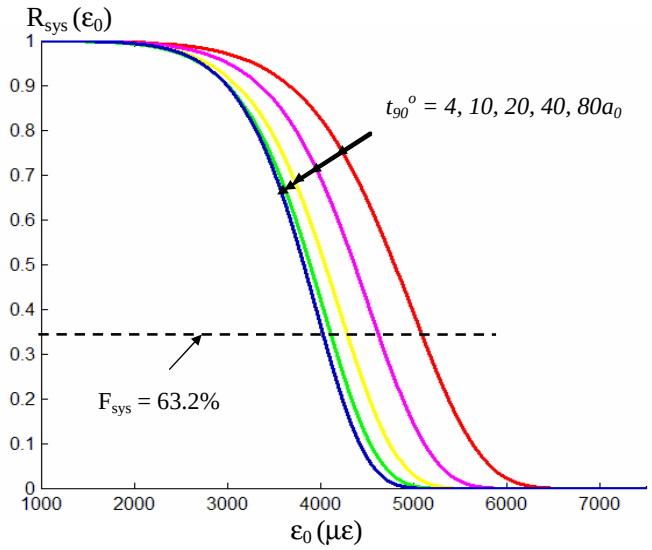

Figure 5.16: The survivability $R_{sys}(= 1 - F_{sys})$ of the 90^o layer v.s. the applied load ϵ_0, for $t_{90^o} = 4a_0$, $10a_0$, $20a_0$, $40a_0$, and $80a_0$. .

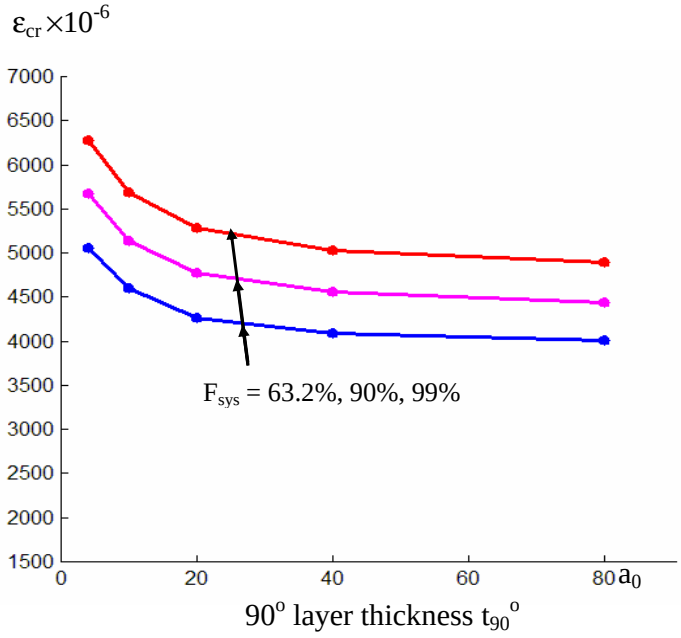

Figure 5.17: The critical laminate strain ϵ_{cr} v.s. the thickness of the 90^o layer, for $F_{sys} = 63.2\%, 90\%$, and 99% respectively.

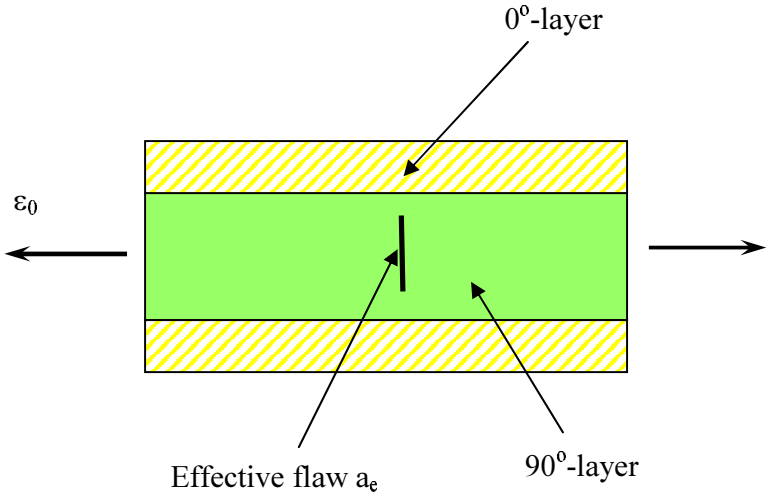

(a)

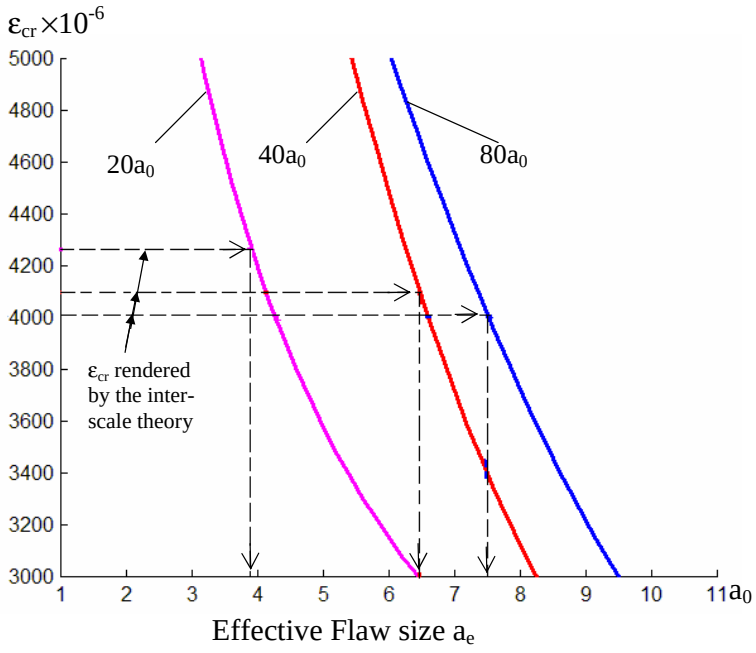

(b)

Figure 5.18: (a) A schematic of the effective flaw introduced into the cross-ply laminate, (b)Application of the inter-scale theory: determine the size of the effective flaw .

Chapter 6: Concluding Remarks

6.1 Summary

In this thesis, a concerted effort is made to obtain the stress/strain fields at the fiber-matrix level in multi-directional laminates when they are under global loads. This effort is directed by the perception that such micro field information is essential for failure theories that describe rationally damages in laminates under loads.

Toward this end, a multi-fiber RVE modelling approach is developed for homogenizing unidirectional fiber-reinforced composite system, and the same modelling concept is applied in de-homogenizing the same composite when it is a part in laminates under load.

The multi-fiber RVE, when chosen properly, can be physically conforming to the statistical homogeneity axiom and material symmetry supposition. Since both serve as basis in the theory of composite homogenization, the effective properties of the UD system so homogenized are exact or nearly exact, in so far as the fiber packing details in the UD system are accurately described.

Similarly, the multi-fiber RVE model is capable of recovering the micro fields at the fiber-matrix level in laminates under external loading, in so far as the macro fields in the homogenized plies are computed accurately. In a sense, the multi-fiber RVE model provides a useful vehicle for studying the various micro scale effects that initiate failures at the fiber-matrix level.

Based on the details in the recovered micro fields in laminates that suffer matrix

cracking, an inter-scale failure theory is then presented to describe the matrix cracking phenomena. The theory requires only a single material condition for matrix cracking, namely, the tensile strength X between two adjacent fibers, X being a random variable. Matrix cracking at the laminate ply level is modelled as a probabilistic event involving certain chain-interactions amongst unit-pairs.

Several numerical examples are presented, using the inter-scale theory to predict the initiation of matrix cracking. All predicted results are consistent with experiments.

It is noted that matrix cracking in the example problems have all been previously treated, with some *ad hoc* failure theories based on the macro fields in the homogenized laminate plies. In all cases, the critical material conditions for matrix cracking are defined at the laminate ply level and characterized by experiments accordingly. As discussed in Chapter 5, characterization at the ply level often fails to provide unique strength properties. The inter-scale theory, however, can simulate most of the experiments; the corresponding macro level material conditions can be deduced using the results from the inter-scale theory.

In this sense, the multi-fiber RVE and the inter-scale theory provide a unique linkage between the micro scale responses and those at the macro scale.

6.2 Directions for Future Work

The emphasis of the present work is placed on the analytical efforts towards a rational description of a particular sub-laminate failure mode, namely, matrix cracking. Further investigation, involving carefully devised experiments, is needed to validate the assumed existence of the random variable X - the tensile strength between two adjacent fibers

in the micro field; the assumed chain-interaction among the fiber pairs in forming the weakest-link model also needs to be checked with validating experiments.

Beyond these validating efforts, the mechanistic/probabilistic combination of the inter-scale theory may also be applied to other matrix-dominated failure modes in composite laminates, such as ply delamination. Micro fields near the laminate free edges have recently been investigated using the multi-fiber RVE model [5]; the inter-scale theory remains to be a viable approach to proceed.

In characterizing composites other than the UD systems, the concept of the multi-fiber RVE could be extended to multi-cell RVE. Examples may be found in tissue engineering: tissue scaffolds are man-made porous structures that guide cell growth into a certain prescribed shape. In order to provide the correct environment for cell growth, the scaffold must possess interconnected channels as well as sufficient strength to maintain structural integrity. Traditionally, composites with repeated unit cells are homogenized by means of a single-cell RVE. As has been demonstrated in this thesis, the single-cell RVE representation invariably leads to inaccuracy in the effective composite properties. In the case of the scaffolds used for tissue growth, a multi-cell RVE model may be developed to characterize the overall properties of the scaffolds; this would also provide a natural model to study the micro-macro interactions, which influence the mechanisms in cell growth.

List of References

[1] J. Aboudi. *Mechanics of Composite Materials A unified micromechanical approach*. Elsevier Science Publishing Company, INC., New York, 1991.

[2] J. Ashton, J. Halpin, and P. Petit. *Primer on Composite Materials: Analysis*. TECHNOMIC Publishing Co., Inc., 750 Summer St., Stamford, Conn. 06901, 1969.

[3] B. Budiansky and T. Wu. Theoretical prediction of plastic strains in polycrystals. In *Proceedings of the 4th U.S. National Congress of Theoretical Applied Mechanics*, page 1175, Berkeley, Calif., 1962.

[4] R. Christensen and K. Lo. Solutions for effective shear properties in three phase sphere and cylinder models. *Journal of the Mechanics and Physics of Solids*, 27:315–330, 1979.

[5] S. Chung. *Effects of Interlaminar Stress Gradients on Free Edge Delamination in Composite Laminates*. PhD thesis, Drexel University, 2003.

[6] F. Crossman and A. Wang. *The Dependence of Transverse Cracking and Delamination onPly Thickness in Graphite/Epoxy Laminates*, pages 118–139. ASTM, Philadelphia, 1982. ASTM STP 775.

[7] F. Crossman, J. Warren, A. Wang, and G. Law. Initiation and growth of transverse cracks and edge delamination in composite laminates, part 2, experimental correlation. *Jounral of Composite Materials*, 14:88–106, 1980.

[8] J. de Kok and H. Meijer. Deformation, yield and fracture of unidirectional composites in transverse loading: 1. influrence of fiber volume fraction and test temperature. *Composites Part A: applied science and manufacturing*, 30A:905–916, 1999.

[9] C. Eringen. *Microcontinuum Field Theories I: Foundations and Solids*. Springer-Verlog New York, Inc., 1999.

[10] J. Fish and K. Shek. Multiscale analysis of composite materials and structures. *Composites Science and Technology*, 60:2547–2556, 2000.

[11] K. Garrett and J. Bailey. Multiple transverse fracture in 90^o cross-ply laminates of a glass fibre-reinforced ployester. *Jounral of Materials Science*, 12:157–168, 1977.

[12] R. Harrison and M. Bader. Damage development in cfrp laminates under monotonic and cyclic stressing. *Fiber Science and Technology*, 18:163–180, 1983.

[13] Z. Hashin. The elastic moduli of heterogeneous materials. *ASME Journal of Applied Mechanics*, pages 143–150, Mar. 1962.

[14] Z. Hashin. Theory of mechanical behavior of heterogeneous media. *Applied Mechanics Reviews*, 17:1–9, 1964.

[15] Z. Hashin. Theory of fiber reinforced materials. Technical report, 1972. NASA Report.

[16] Z. Hashin and B. Rosen. The elastic moduli of fiber-reinforced materials. *ASME Journal of Applied Mechanics*, 31:223–232, 1964.

[17] Z. Hashin and S. Shtrikman. A varational approach to the theory of the elastic behaviour of multi-phase materials. *Journal of the Mechanics and Physics of Solids*, 11:143–150, Mar.-Apr. 1963.

[18] M. Heaton. A calculation of the elastic constants of a unidirectional fibre-reinforced composites. *British Journal of Applied Physics Series*, 21:1039–1048, 1968.

[19] J. Hermans. The elastic properties of fiber reinforced materials when the fibers are aligned. In *Proc. Koninkl, Nederl, Akad, Wetenschappen*, volume B70, page 1, 1967.

[20] A. Hershey. The elasticity of an isotropic aggregate of anisotropic cubic crystals. *ASME Journal of Applied Mechanics*, 21:236, 1954.

[21] R. Hill. Elastic properties of reinforced solids: Some theoretical principles. *Journal of the Mechanics and Physics of Solids*, 11:357–372, 1963.

[22] R. Hill. Theory of mechanical properties of fiber-reinforced materials: I. elastic behavior. *Journal of the Mechanics and Physics of Solids*, 12:199, 1964.

[23] R. Hill. Theory of mechanical properties of fibre-strengthened materials - iii self consistent model. *Journal of the Mechanics and Physics of Solids*, 13:189, 1965.

[24] O. Hoffman. The brittle strength of orthotropic materials. *Journal of Composite Materials*, 1:200–206, 1967.

[25] S. Hollister and N. Kikuchi. A comparison of homogenization and standard mechanics analyses for periodic porous composites. *Computational Mechanics*, 10:73–95, 1992.

[26] P. Hutapea, F. Yuan, and N. Pagano. Micro-stress prediction in composite laminates with high stress gradients. *International Journal of Solids and Structures*, 40:2215–2248, 2003.

[27] R. Jones. *Mechanics of Composite Materials*. Taylor & Francis, 1999. 2nd Edition.

[28] B. Kaminski. *Effects of Specimen Geometry on the Strength of Composite Materials*, pages 181–191. ASTM, Philadelphia, 1973. ASTM STP 521.

[29] Y. Korczynskij and J. Morley. Constrained cracking in cross-ply laminates. *Journal of Material Science*, 16:1785–1795, 1981.

[30] G. Law. *Fracture Analysis of* $(\pm 25/90_n)_s$ *Graphite-Epoxy Composite Laminates*. PhD thesis, Drexel University, 1981.

[31] S. Lei. *A Stochastic Model for the Damage Growth During the Transverse Cracking Process in Composite Laminates*. PhD thesis, Drexel University, 1987.

[32] S. Li. General unit cells for micromechanical analyses of unidirectional composites. *Composites Part A: applied science and manufacturing*, 32:815–826, 2000.

[33] L. McCartney. Theory of stress transfer in a $0^o - 90^o - 0^o$ cross-ply laminate containing a parallel array of transverse cracks. *Journal of the Mechanics and Physics of Solids*, 40:27–68, 1992.

[34] L. McCartney. Predicting transverse crack formation in cross-ply laminates. *Composites Science and Technology*, 58:1069–1081, 1998.

[35] N. Pagano and F. Yuan. The significance of effective modulus theory (homogenization) in composite laminate mechanics. *Composites Science and Technology*, 60:2471–2488, 2000.

[36] A. Parvizi, K. Garrett, and J. Bailey. Constrained cracking in glass fibre-reinforced epoxy cross-ply laminates. *Jounral of Materials Science*, 13:195–201, 1978.

[37] B. Paul. Prediction of elastic constants of multiphase materials. *Transactions of the Metallurgical Society of AIME*, pages 36–41, Feb. 1960.

[38] C. Pellegrino, U. Galvanetto, and B. Schrefler. Numerical homogenization of periodic composite materials with non-linear material components. *International Jounral for Numerical Methods in Engineering*, 46:1609–1637, 1999.

[39] R. Pipes and N. Pagano. Interlaminar stresses in composite laminates under uniaxial extension. *Journal of Composite Materials*, 4:538–548, 1970.

[40] P. Raghavan, S. Moorthy, S. Ghosh, and N. Pagano. Revisiting the composite laminate problem with an adaptive multi-level computational model. *Composites Science and Technology*, 61:1017–1040, 2001.

[41] G. Sih, P. Paris, and G. Irwin. On cracks in rectlinearly anisotopic bodies. *International Journal of Fracture Mechanics*, 1:189–203, 1965.

[42] C. Sun and R. Vaidya. Prediction of composites from a representative volume element. *Composites Science and Technology*, 56:171–179, 1996.

[43] C. Sun and Y. Wang. Determine the size of "local domain" in multi-scale analysis. In *Proceedings of the 13th International Conference of Composite Materials*, 2001. Paper Number: 1681.

[44] P. Suquet. *Elements of Homogenization Theory for Inelastic Solid Mechanics*, pages 194–275. Springer-Verlag, Berline-Heidelberg-New York, 1987.

[45] L. Sutherland, R. Shenoi, and S. Lewis. Size and scale effects in composites: Ii. unidirectional laminates. *Composites Science and Technology*, 59:221–233, 1999.

[46] S. Tsai and T. Hahn. *Introduction to Composite Materials*. Technomic Publishing Co., Inc., Westport, CT., 1980.

[47] S. Tsai and E. Wu. A general theory of strength for anisotropic materials. *Journal of Composite Materials*, 5:58–81, 1971.

[48] A. Wang. *Fracture Mechanics of Sublaminate Cracks in Composite Materials*, pages 45–62. ASTM, 1984.

[49] A. Wang and F. Crossman. Some new results on edge effects in symmetric composite laminate. *Journal of Composite Materials*, 11:92–102, 1977.

[50] A. Wang, F. Crossman, G. Law, and J. Warren. Initiation and growth of transverse cracks and edge delamination in composite laminates, part 1, an energy method. *Jounral of Composite Materials*, 14:71–87, 1980.

[51] A. Wang, N. Kishore, and C. Li. Crack development in graphite-epoxy cross-ply laminates under uniaxial tension. *Composites Science and Technology*, 24:1–31, 1985.

[52] A. Wang and C. Yan. On a unique linkage between micro and macro. In *Proceedings of the American Society for Composites 17th Technical Conference*, Purdue University, West Lafayette, Indiana, 2002. Paper Number: 140.

[53] Y. Wang, C. Sun, X. Sun, and N. Pagano. *Principle of Recovering Microstress in Multi-Level Analysis*. ASTM, Philadelphia, 2002. ASTM STP 1416.

[54] W. Weibull. A statistical distributiton function of wide applicability. *Jounral of Applied Mechanics*, 18:293–297, 1951.

[55] F. Yuan, N. Pagano, and X. Cai. Elastic moduli of brittle matrix composites with interfacial debonding. *International Journal of Solids and Structures*, 34(2):177–201, 1997.

Appendix A: Supplemental Boundary Conditions

A.1 Periodic Boundary Conditions

For UD composites having square and hexagonal arrays, the concept of translational symmetry is applied to describe the periodic boundary conditions by Li [32]. The compatible displacement and traction boundary conditions on the periodic element are described in terms of uniform far-field loading. The detailed expressions for the composites with square and hexagonal arrays are given as the follows respectively.

Square Array

Figure 2.9 displays the RVE for the square array and the two mutually orthogonal translational symmetry axes in the $x_2 - x_3$ plane for the square array. The boundary conditions are described on the two pairs of sides of the periodic element; and they consist of the displacement boundary conditions and the compatible traction conditions. The displacement boundary conditions are given by

$$\begin{aligned} (u_1|_{x_2=b} - u_1|_{x_2=-b})|_{x_3} &= 2b\ \gamma_{12}^0 \\ (u_2|_{x_2=b} - u_2|_{x_2=-b})|_{x_3} &= 2b\ \epsilon_{22}^0 \\ (u_3|_{x_2=b} - u_3|_{x_2=-b})|_{x_3} &= 0 \end{aligned} \tag{A.1}$$

$$(u_1|_{x_3=b} - u_1|_{x_3=-b})|_{x_2} = 2b\gamma_{13}^0$$

$$
\begin{aligned}
(u_2|_{x_3=b} - u_2|_{x_3=-b})|_{x_2} &= 2b\gamma^0_{23} \\
(u_3|_{x_3=b} - u_3|_{x_3=-b})|_{x_2} &= 2b\epsilon^0_{33}.
\end{aligned} \tag{A.2}
$$

The compatible traction conditions are

$$
\begin{aligned}
(\sigma_{22}|_{x_2=b} - \sigma_{22}|_{x_2=-b})|_{x_3} &= 0 \\
(\tau_{12}|_{x_2=b} - \tau_{12}|_{x_2=-b})|_{x_3} &= 0 \\
(\tau_{23}|_{x_2=b} - \tau_{23}|_{x_2=-b})|_{x_3} &= 0
\end{aligned} \tag{A.3}
$$

$$
\begin{aligned}
(\sigma_{33}|_{x_23=b} - \sigma_{33}|_{x_3=-b})|_{x_2} &= 0 \\
(\tau_{13}|_{x_3=b} - \tau_{13}|_{x_3=-b})|_{x_2} &= 0 \\
(\tau_{23}|_{x_3=b} - \tau_{23}|_{x_3=-b})|_{x_2} &= 0.
\end{aligned} \tag{A.4}
$$

Hexagonal Array

The RVE for the hexagonal array is shown in Figure 2.10, along with the three axes of translational symmetry; each axis is 60^o from the other two. Three sets of displacement boundary conditions on the three pairs of sides of the periodic element are presented as

$$
\begin{aligned}
(u_1|_{x_2=b} - u_1|_{x_2=-b})|_{x_3} &= 2b\gamma^0_{12} \\
(u_2|_{x_2=b} - u_2|_{x_2=-b})|_{x_3} &= 2b\epsilon^0_{22} \\
(u_3|_{x_2=b} - u_3|_{x_2=-b})|_{x_3} &= 0
\end{aligned} \tag{A.5}
$$

$$
\begin{aligned}
(u_1|_{x_2+\sqrt{3}x_3=2b} - u_1|_{x_2+\sqrt{3}x_3=-2b})|_{\sqrt{3}x_2-x_3} &= b\gamma_{12}^0 + \sqrt{3}b\gamma_{13}^0 \\
(u_2|_{x_2+\sqrt{3}x_3=2b} - u_2|_{x_2+\sqrt{3}x_3=-2b})|_{\sqrt{3}x_2-x_3} &= b\epsilon_{22}^0 + \sqrt{3}b\gamma_{23}^0 \\
(u_3|_{x_2+\sqrt{3}x_3=2b} - u_3|_{x_2+\sqrt{3}x_3=-2b})|_{\sqrt{3}x_2-x_3} &= \sqrt{3}\epsilon_{33}^0
\end{aligned} \tag{A.6}
$$

$$
\begin{aligned}
(u_1|_{-x_2+\sqrt{3}x_3=2b} - u_1|_{-x_2+\sqrt{3}x_3=-2b})|_{\sqrt{3}x_2+x_3} &= b\gamma_{12}^0 - \sqrt{3}b\gamma_{13}^0 \\
(u_2|_{-x_2+\sqrt{3}x_3=2b} - u_2|_{-x_2+\sqrt{3}x_3=-2b})|_{\sqrt{3}x_2+x_3} &= b\epsilon_{22}^0 - \sqrt{3}b\gamma_{23}^0 \\
(u_3|_{-x_2+\sqrt{3}x_3=2b} - u_3|_{-x_2+\sqrt{3}x_3=-2b})|_{\sqrt{3}x_2+x_3} &= -\sqrt{3}\epsilon_{33}^0.
\end{aligned} \tag{A.7}
$$

Three sets of compatible traction boundary conditions are given by

$$
\begin{aligned}
(\sigma_{22}|_{x_2=b} - \sigma_{22}|_{x_2=-b})|_{x_3} &= 0 \\
(\tau_{23}|_{x_2=b} - \tau_{23}|_{x_2=-b})|_{x_3} &= 0 \\
(\tau_{12}|_{x_2=b} - \tau_{12}|_{x_2=-b})|_{x_3} &= 0
\end{aligned} \tag{A.8}
$$

$$
\begin{aligned}
\left[\left(\sqrt{3}\sigma_{22} + \tau_{23}\right)|_{x_2+\sqrt{3}x_3=2b} - \left(\sqrt{3}\sigma_{22} + \tau_{23}\right)|_{x_2+\sqrt{3}x_3=-2b}\right]|_{\sqrt{3}x_2-x_3} &= 0 \\
\left[\left(\sqrt{3}\tau_{23} + \sigma_{33}\right)|_{x_2+\sqrt{3}x_3=2b} - \left(\sqrt{3}\tau_{23} + \sigma_{33}\right)|_{x_2+\sqrt{3}x_3=-2b}\right]|_{\sqrt{3}x_2-x_3} &= 0 \\
\left[\left(\sqrt{3}\tau_{12} + \tau_{13}\right)|_{x_2+\sqrt{3}x_3=2b} - \left(\sqrt{3}\tau_{12} + \tau_{13}\right)|_{x_2+\sqrt{3}x_3=-2b}\right]|_{\sqrt{3}x_2-x_3} &= 0
\end{aligned} \tag{A.9}
$$

$$
\begin{aligned}
\left[\left(\sqrt{3}\sigma_{22} - \tau_{23}\right)|_{-x_2+\sqrt{3}x_3=2b} - \left(\sqrt{3}\sigma_{22} - \tau_{23}\right)|_{-x_2+\sqrt{3}x_3=-2b}\right]|_{\sqrt{3}x_2+x_3} &= 0 \\
\left[\left(\sqrt{3}\tau_{23} - \sigma_{33}\right)|_{-x_2+\sqrt{3}x_3=2b} - \left(\sqrt{3}\tau_{23} - \sigma_{33}\right)|_{-x_2+\sqrt{3}x_3=-2b}\right]|_{\sqrt{3}x_2+x_3} &= 0
\end{aligned} \tag{A.10}
$$

$$\left[\left(\sqrt{3}\tau_{12}-\tau_{13}\right)|_{-2+\sqrt{3}x_3=2b}-\left(\sqrt{3}\tau_{12}-\tau_{13}\right)|_{-x_2+\sqrt{3}x_3=-2b}\right]|_{\sqrt{3}x_2+x_3} \quad = \quad 0.$$

For purpose of determining the effective moduli, a corresponding individual strain component need be singled out in each case; and the effective modulus can be computed by solving the resulting B-V problem. Note that, in the case of square array, Equation (A.1-A.2) will be the same as ones listed in Table 2.2 by setting $a = b$.

A.2 Uniform Boundary Conditions for orthotropic materials

While applying the bounding technique, a sets of uniform displacement and traction boundary conditions on the boundary of the RVE are needed to determine the effective elastic properties. This appendix describes the boundary conditions for an orthotropic material. Here, consider the UD composite having rectangular array. Orthotropy is assumed; 9 independent elastic constants are needed. A set of 6 independent loading cases for all 9 constants are listed in Table A.1.

Table A.1: Uniform boundary conditions and corresponding effective elastic and mathematic constants for a UD composite with rectangular array.

Elastic and Mathematic constants	Strain B.C.	Displacement B.C.	Stress B.C.	Traction B.C.	FE models
C_{11} C_{12} C_{13} (E_{11}) (ν_{12}) (ν_{13})	$\epsilon_{11} = \epsilon_{11}^0$ $\epsilon_{22} = 0$ $\epsilon_{33} = 0$ $\epsilon_{ij} = 0$ $i \neq j$	$u_1 = \epsilon_{11}^0 x_1$ $u_2 = 0$ $u_3 = 0$	$\sigma_{11} = \sigma_{11}^0$ $\sigma_{22} = 0$ $\sigma_{33} = 0$ $\sigma_{ij} = 0$ $i \neq j$	$T_1(x_2, x_3) = \sigma_{11}^0$ $T_2 = 0$ $T_3 = 0$	generalized plain strain
C_{22} C_{23} (E_{22}) (ν_{23})	$\epsilon_{11} = 0$ $\epsilon_{22} = \epsilon_{22}^0$ $\epsilon_{33} = 0$ $\epsilon_{ij} = 0$ $i \neq j$	$u_1 = 0$ $u_2 = \epsilon_{22}^0 x_2$ $u_3 = 0$	$\sigma_{11} = 0$ $\sigma_{22} = \sigma_{22}^0$ $\sigma_{33} = 0$ $\sigma_{ij} = 0$ $i \neq j$	$T_1 = T_3 = 0$ $T_2(x_2^0, x_3) = \sigma_{22}^0$ $T_2(-x_2^0, x_3) = -\sigma_{22}^0$ $T_2(x_2, x_3^0) = 0$ $T_2(x_2, -x_3^0) = 0$	plain strain
C_{33} (E_{33})	$\epsilon_{11} = 0$ $\epsilon_{22} = 0$ $\epsilon_{33} = \epsilon_{33}^0$ $\epsilon_{ij} = 0$ $i \neq j$	$u_1 = 0$ $u_2 = 0$ $u_3 = \epsilon_{33}^0 x_3$	$\sigma_{11} = 0$ $\sigma_{22} = 0$ $\sigma_{33} = \sigma_{33}^0$ $\sigma_{ij} = 0$ $i \neq j$	$T_1 = T_2 = 0$ $T_3(x_2^0, x_3) = 0$ $T_3(-x_2^0, x_3) = 0$ $T_3(x_2, x_3^0) = \sigma_{33}^0$ $T_3(x_2, -x_3^0) = -\sigma_{33}^0$	plain strain
C_{44} (G_{23})	$\gamma_{23} = \gamma_{23}^0$ other $\epsilon_{ij} = 0$	$u_2 = \frac{\gamma_{23}^0 x_3}{2}$ $u_3 = \frac{\gamma_{23}^0 x_2}{2}$ $u_1 = 0$	$\sigma_{23} = \sigma_{23}^0$ other $\sigma_{ij} = 0$	$T_1 = 0$ $T_2(x_2^0, x_3) = 0$ $T_2(-x_2^0, x_3) = 0$ $T_2(x_2, x_3^0) = \sigma_{23}^0$ $T_2(x_2, -x_3^0) = -\sigma_{23}^0$ $T_3(x_2^0, x_3) = \sigma_{23}^0$ $T_3(-x_2^0, x_3) = -\sigma_{23}^0$ $T_3(x_2, x_3^0) = 0$ $T_3(x_2, -x_3^0) = 0$	plain strain
C_{55} (G_{13})	$\gamma_{13} = \gamma_{13}^0$ other $\gamma_{ij} = 0$	$u_1 = \gamma_{13}^0 x_3$ $u_2 = 0$ $u_3 = 0$	$\sigma_{13} = \sigma_{13}^0$ other $\sigma_{ij} = 0$	$T_1(x_2^0, x_3) = 0$ $T_1(-x_2^0, x_3) = 0$ $T_1(x_2, x_3^0) = \sigma_{13}^0$ $T_1(x_2, -x_3^0) = -\sigma_{13}^0$ $T_2 = T_3 = 0$	generalized plain strain
C_{66} (G_{12})	$\gamma_{12} = \gamma_{12}^0$ other $\gamma_{ij} = 0$	$u_1 = \gamma_{12}^0 x_1$ $u_2 = 0$ $u_3 = 0$	$\sigma_{12} = \sigma_{12}^0$ other $\sigma_{ij} = 0$	$T_1(x_2^0, x_3) = \sigma_{12}^0$ $T_1(-x_2^0, x_3) = -\sigma_{12}^0$ $T_1(x_2, x_3^0) = 0$ $T_1(x_2, -x_3^0) = 0$ $T_2 = T_3 = 0$	generalized plain strain

VITA

Chang (Karen) Yan received her B.S. degree from University of Science and Technology of China in 1993, with major in mechanical engineering and minor in management and information science. She then worked in Panda Electronic Inc.(Nanjing, China) as a mechanical engineer from 1993 to 1997. She was sent to Panasonic Electronic Inc.(Osaka, Japan) as a visiting mechanical engineer from 1994 to 1995. In 1998, she started her graduate study in the Department of Mechanical Engineering and Mechanics at Drexel University. She received her Master degree in June, 2000. During her stay at Drexel, she has received several awards based on her academic achievements and her professional service. She was the recipient of the Albert & Harriet Soffa Fellowship from 1999 to 2003, the Graduate Student Research Award in 2001, and the Michael Herman Memorial Scholarship in 2000.